



UNIVERSITÀ
DEGLI STUDI
DI BRESCIA

DIPARTIMENTO DI
INGEGNERIA MECCANICA E INDUSTRIALE

Dottorato di Ricerca in
Ingegneria Meccanica e Industriale

Structural integrity of cellular materials: Characterization and research of structure-property relationships

ING-IND/22 Scienza e Tecnologia dei Materiali

Supervisore:
Prof. Francesco Baldi
Tutor:
Prof. Stefano Pandini

Dottorando:
Jacopo Agnelli

XXXVI Ciclo

Riassunto

In questo lavoro è stata studiata l'integrità strutturale di materiali cellulari a celle aperte. I materiali cellulari sono classificati principalmente sulla base del grado di regolarità strutturale, controllabile a priori in fase di design, che porta alla distinzione tra schiume stocastiche (a struttura casuale) e materiali cellulari a struttura controllata (ACM). Numerosi esempi di schiume stocastiche possono essere trovati in natura (legno, osso trabecolare, carbone, spugne), nella vita di tutti i giorni (pane e lievitati) e in laboratorio (praticamente ogni classe di materiali può essere utilizzata per la produzione di schiume). In questo lavoro di ricerca, l'attenzione è stata concentrata sull'osso trabecolare, nella forma di tessuti ossei utilizzati per la produzione di innesti ossei eterologhi. L'attività è stata svolta in collaborazione con Bioteck S.p.A. (Arcugnano, Vicenza, Italia), un'azienda che si occupa di ricerca, sviluppo e produzione di sostituti ossei per la medicina rigenerativa. I sistemi analizzati, di origine equina, sono stati prelevati da diversi siti anatomici, e presentano significative variazioni di contenuto minerale, essendo parte di essi marcatamente demineralizzata. Quindi, sono stati studiati tessuti ossei con risposta estremamente diversa - rigida e fragile da un lato, cedevole e duttile dall'altro - che richiedevano specifiche tecniche e metodi per essere approcciati. L'osso trabecolare è caratterizzato da una struttura porosa, da un'architettura altamente complessa e da rilevanti eterogeneità a diversi livelli, rendendo l'ipotesi di *continuo*

chiaramente violata. Al fine di approssimare problemi metodologici di carattere fondamentale legati all'applicabilità di procedure di laboratorio per lo studio dell'integrità strutturale di tessuti ossei trabecolari, sono state studiate strutture "modello" in materiale polimerico ad architettura controllata. Tali strutture sono state progettate e successivamente realizzate utilizzando la tecnica di modellazione a deposizione fusa (FDM). L'attenzione è stata posta volontariamente su sistemi caratterizzati da una risposta duttile, realizzati in resina Acrilnitrile-Butadiene-Stirene (ABS), al fine di relazionare direttamente i risultati al caso di tessuti ossei marcatamente demineralizzati, considerati come quelli più ostici da caratterizzare e studiare. L'attività è stata svolta in collaborazione con l'Istituto di Sistemi e Tecnologie Industriali Intelligenti per il Manifatturiero Avanzato del Consiglio Nazionale delle Ricerche (STIIMA-CNR - Milano, Italia). L'elevato grado di regolarità, modulabile con precisione *a-priori* in fase di design, colloca le strutture nella categoria degli ACM. In aggiunta, la fase di produzione è stata realizzata in maniera che le pareti delle celle fossero costituite da un unico filamento di materiale polimerico (ABS), che assume quindi il ruolo di elemento strutturale fondamentale dei sistemi.

Lo scopo del lavoro è duplice: 1) lo sviluppo di affidabili metodologie di prova per lo studio dell'integrità strutturale di materiali cellulari, principalmente nell'ambito della Meccanica della Frattura (FM); 2) la ricerca di correlazioni proprietà-struttura, sia nel caso dei tessuti ossei trabecolari che delle strutture "modello" in materiale polimerico. Il primo tratto innovativo della ricerca va trovato nel particolare tipo di tessuti ossei esaminati. Nonostante numerosi lavori di letteratura sulla meccanica dell'osso trabecolare siano stati svolti e pubblicati, ad oggi l'attenzione non è mai stata posta su tessuti ossei eterologhi di tipo commerciale, specificatamente pre-trattati al fine di garantire biocompatibilità, e, talvolta, anche marcatamente demineralizzati. Negli ultimi anni, tali sistemi, la cui domanda in ambito clinico è in costante crescita, sono stati analizzati dal punto di vista biologico, medico e della sicurezza per il paziente. Tuttavia, il loro comporta-

mento meccanico - per non parlare della loro integrità strutturale - non sono mai stati esaminati nel dettaglio.

L'integrità strutturale dei tessuti ossei trabecolari, così come delle strutture modello in materiale polimerico (ABS), è stata in primo luogo studiata a compressione, la principale condizione di carico a cui sono sottoposti i materiali cellulari, come riportato in letteratura. Gli effetti della geometria dei provini, delle loro dimensioni e della direzione di carico sulla risposta meccanica sono stati studiati anche considerando i risultati provenienti da (i) prove cicliche in compressione e (ii) analisi morfologiche delle strutture deformate. La prima fase della ricerca (a compressione) era finalizzata a incrementare la conoscenza della risposta meccanica di sistemi così complessi, ponendo solide basi per lo studio dell'integrità strutturale nell'ambito della Meccanica della Frattura. A valle dello studio dei sistemi a compressione, è stato possibile selezionare adeguate geometrie e dimensioni dei provini per prove di frattura. In aggiunta, nel caso dell'osso trabecolare, il ruolo secondario giocato dall'architettura trabecolare e dalla direzione di carico sulla risposta meccanica a compressione ha consentito di prescindere dalla posizione e dall'orientazione di prelievo dal sito anatomico, nella selezione dei tessuti per i provini a frattura. In tal modo, i risultati ottenuti sarebbero stati rappresentativi dei veri tessuti di tipo commerciale, e non di un loro particolare sottoinsieme con specifiche caratteristiche non ricercate nella pratica industriale. La possibilità di cedimento strutturale sotto carico costante è stata evidenziata in prove di creep a compressione, svolte al fine di mettere in luce la natura viscoelastica dei tessuti.

Alla luce dell'elevata porosità, dell'architettura complessa e della natura eterogenea dei sistemi, nel presente lavoro la caratterizzazione nell'ambito della Meccanica della Frattura è stata svolta seguendo l'approccio energetico, preferendolo a quello tensionale, basato sul concetto di fattore di intensificazione dello sforzo e largamente utilizzato nella letteratura sulla frattura dei materiali cellulari. L'approccio energetico prescinde completamente dal campo di sforzo che si instaura localmente all'apice della cricca - la cui precisa determinazione

richiederebbe l'utilizzo di tecniche di modellazione agli elementi finiti (FEM) - e produce risultati di tenacità a frattura caratteristici del sistema nella sua globalità. Ogni fase nello sviluppo della metodologia di prova e di elaborazione dei dati è stata attentamente trattata, sfruttando le conoscenze e l'esperienza maturate nello studio della Meccanica della Frattura sui materiali polimerici duttili. Tutte le problematiche di carattere metodologico sono state dapprima approcciate sulle strutture "modello" in ABS e le soluzioni adottate sono state poi estese al caso dell'osso trabecolare, per il quale si sono dimostrate funzionali e affidabili. Nelle fasi di design e produzione degli ACM "modello", la porosità effettiva è stata fatta variare tra $\approx 20\%$ e $\approx 75\%$. Nonostante solo le strutture con porosità maggiore del 70% possano essere considerate a tutti gli effetti materiali cellulari (secondo la definizione classica da letteratura), lo studio di strutture a densità più elevata ha dato un importante contributo alla conoscenza dei meccanismi alla base della frattura dei sistemi cellulari. Riguardo agli aspetti metodologici, particolare attenzione è stata riservata a: 1) intaglio - l'acutezza dell'apice dell'intaglio e l'assenza di danneggiamento nella regione ad esso circostante sono state verificate, e la natura discontinua del fronte d'intaglio è stata messa in luce attraverso modelli CAD specificatamente sviluppati per il caso di ACM in materiale polimerico e scansioni di tomografia computerizzata (CT) per i tessuti ossei; 2) innesco del processo di frattura - l'approccio sinergico derivante dall'analisi delle curve di carico e delle immagini ad alta risoluzione scattate durante la prova ha consentito il posizionamento del punto d'innesco in corrispondenza di discontinuità nel segnale di carico (brusche cadute o variazioni di pendenza), ben prima che il picco di carico fosse raggiunto; 3) contributo locale dell'indentazione tra rullo e provino, in prove di frattura in configurazione di flessione a tre punti, specialmente nel caso di sistemi ad elevata cedevolezza; 4) densità locale - nel caso dell'osso trabecolare, il contributo della densità locale sulla risposta dei sistemi è stato studiato, riferendo le proprietà alla densità locale della regione coinvolta nel processo di frattura. Diverse branche di Mec-

canica della Frattura (FM) sono state considerate: da un lato quella Lineare Elastica (LEFM) per l'osso trabecolare a contenuto minerale invariato, rigido e fragile, dall'altro quella Elasto-Plastica (EPFM), per i tessuti ossei demineralizzati e per gli ACM in materiale polimerico, altamente cedevoli e duttili. Per gli ACM, la tenacità a frattura - valutata secondo l'approccio energetico - è risultata insensibile al grado di porosità. Questo è stato verificato su un ampio range di porosità, fino al raggiungimento di condizioni vicine a quelle di *continuo* - in corrispondenza delle quali si ha un cambio nell'interazione strutturale tra i filamenti. A basse deformazioni, sebbene la risposta sia risultata fortemente dipendente dalla densità apparente dei sistemi, importanti variazioni sono state ancora una volta rilevate all'avvicinarsi delle condizioni di minima porosità. Nel caso dell'osso trabecolare, la tenacità a frattura è risultata fortemente dipendente dal materiale trabecolare (in termini di percentuali relative di minerale e collagene). I dati per il tessuto a contenuto minerale invariato sono stati confrontati con successo con la (estremamente limitata) letteratura riguardo a sistemi di simile natura. Nel caso del tessuto osseo marcatamente demineralizzato, invece, è stata esaminata l'applicabilità di approcci monocampione innovativi basati sul Criterio di Separazione del Carico (LSC). In primo luogo, il LSC è stato utilizzato per esplorare la possibilità di ricorrere ad approcci di tipo multicampione, che si sono rivelati non validi, supportando quindi l'evidenza sperimentale fornita dalle analisi morfologiche e dalle prove meccaniche. In secondo luogo, ricorrendo al metodo della normalizzazione basato sul LSC, è stato possibile tentare la costruzione delle curve-R - curve di resistenza in cui il parametro di tenacità a frattura è espresso in funzione dell'avanzamento della cricca - nel caso di tessuti ossei altamente demineralizzati.

Lo sviluppo di una nuova e affidabile metodologia di prova ed elaborazione dei dati per lo studio dell'integrità strutturale dei materiali cellulari nell'ambito della Meccanica della Frattura è stato condotto con successo. Il metodo è stato applicato con ottimi risultati al caso di tessuti ossei trabecolari di tipo commerciale, preventivamente

trattati e talvolta anche marcatamente demineralizzati. In aggiunta all'elevato interesse scientifico - alla luce della mancanza ad oggi di una dettagliata caratterizzazione meccanica e a frattura di sistemi così complicati e particolari - l'importanza del metodo si estende anche alla sfera industriale, fornendo informazioni fondamentali che possono aiutare nelle fasi di progettazione, produzione e controllo qualità di tessuti ossei commerciali sviluppati *ad-hoc* per la specifica applicazione richiesta in medicina rigenerativa.

Abstract

In this work, the structural integrity of open-celled cellular materials was investigated. Cellular materials are mainly classified on the basis of the degree of structural regularity and *a-priori* tailorability, which leads to the distinction between randomly arranged stochastic foams and highly ordinated Architected Cellular Materials, ACMs. Many examples of stochastic foams can be found in nature (*e.g.* wood, trabecular bone, cork, sponge), in everyday life (*e.g.* bread and starch-based products) and in laboratory (virtually every class of materials can be industrially foamed). In the present research activity, the attention was focused on the specific case of trabecular bone, in the form of bone tissues used for the manufacturing of heterologous bone grafts. The activity was carried out in collaboration with Bioteck S.p.A. (Arcugnano, Vicenza, Italy), a company that deals with the research and production of tissue substitutes for regenerative medicine. The systems under analysis, of equine origin, were harvested from different anatomic sites, and presented relevant variations in the mineral content, being part of them markedly demineralized. Thus, bone tissues with extremely different response – stiff and brittle-like on one hand vs compliant and ductile-like on the other – were studied, requiring specific approaches to be addressed. Trabecular bone is characterized by porous structure, high degree of architectural complexity and pronounced heterogeneity at different scales, and the *continuum* assumption is clearly violated. To address

specific fundamental and methodological issues concerning the applicability of laboratory testing-schemes to the study of the structural integrity of the trabecular bone tissues, polymer-based "model" structures with controlled architecture, designed and manufactured by means of the Fused Deposition Modeling, FDM, technique, were examined. The attention was voluntarily paid to structures exhibiting a ductile behaviour, manufactured in Acrylonitrile-Butadiene-Styrene (ABS) resin, with the aim to directly relate the results to the case of the ductile-like demineralized bone tissues, which were regarded to be more challenging to study. This activity was carried out in collaboration with STIIMA-CNR (Institute of Intelligent Industrial Systems and Technologies for Advanced Manufacturing - Consiglio Nazionale delle Ricerche, Milan, Italy). The high regularity degree, tailored *a-priori* in the design phase, makes the structures belong to the category of ACMs. Further, the manufacturing process was carried out so that cell walls were made of a single filament of polymeric material, which thus assumed the role of the fundamental structural element.

The aim of the work was twofold: 1) the development of reliable testing methods for the study of the structural integrity of cellular materials, mainly within the framework of the Fracture Mechanics (FM); 2) the research of structure-property relationships for both the trabecular bone tissues and the polymer-based "model" structures examined. The first novelty character of this research is to be found in the specific type of trabecular bone tissues examined. Even if many literature papers have been published on the mechanics of trabecular bone, so far the attention has never been focused on commercial heterologous bone tissues, specifically pre-treated in order to ensure biocompatibility and, in some cases, even markedly demineralized. Biological and safety-profile analyses of systems with such unique features, increasingly used in clinical practice, have already been carried out, but their mechanical behaviour - not to mention their structural integrity - was never examined before.

The structural integrity of the trabecular bone tissues, as well as of the ABS-based model structures, was firstly studied under com-

pression, which is the most frequent loading condition experienced and analyzed in the relevant literature on cellular materials. The effect of specimen geometry, size and loading direction on the mechanical response was discussed in the light of the outcomes from (i) cyclic compression experiments and (ii) morphological analyses on the deformed materials. This first research phase (compression tests) was meant to improve the knowledge of the mechanical response of such complex systems, laying solid foundations for its assessment in the framework of FM. Appropriate specimen geometry and size could be selected for the execution of the fracture tests. Further, in the case of trabecular bone, the secondary role played by trabecular architecture and loading direction in the mechanical response analyzed under compression allowed the fracture specimens not to be bound by position or orientation during harvesting. Thus, the outcomes were representative of the actual as-made commercial products, and not of a specific subset with defined features (not explored in industrial practice). The possibility for failure under static loading conditions was observed in compression creep tests.

In the present work, for the FM characterization, in consideration of the high porosity, architectural complexity and heterogeneous nature of the systems under analysis, the energetic approach was preferred to the tensional one, which is based upon the stress intensity factor concept and used in the relevant literature for the fracture characterization of cellular materials. The former approach neglects completely the stress field at the crack tip, whose precise evaluation would require resorting to Finite Element Modeling (FEM), and provides fracture toughness parameters with a more global character. Each step in the development of the testing and data elaboration method was carefully addressed, on the basis of the experience in FM testing of ductile polymers. All the methodological problems were addressed on polymer-based ACMs first, and the solutions adopted then extended to the case of trabecular bone, proving to be reliable. In ACMs design and manufacturing stages, the effective porosity was varied between $\approx 20\%$ and $\approx 75\%$. Even though only the structures

with porosity level above 70% could be considered as full-fledged cellular materials, the study of the more dense structures gave an important contribution in understanding the mechanisms governing the fracture of the cellular systems. Concerning the methodological aspects, special attention was paid to: 1) notching - the tip sharpness and the absence of damage ahead of the tip were verified, and the discontinuous nature of crack front was pointed out by means of CAD models specifically developed and CT-scans, for the ACMs and bone tissues, respectively; 2) fracture initiation - the synergistic approach coming from the analysis of loading curves and high-resolution images taken during the tests allowed to place the initiation point in correspondence of discontinuities in the load signal (either drops or slope variations), long before the load peak was reached; 3) contribution of the specimen local indentation in the three-point bending-based fracture tests, especially in the case of highly-compliant systems; 4) local density - for stochastic-foam-like trabecular bone, the contribution of local density on the response of the systems was studied, by referring the properties to the density levels of the crack process region. Different FM approaches were considered: either Linear-Elastic Fracture Mechanics (LEFM) or Elastic-Plastic Fracture Mechanics (EPFM), for stiff brittle-like trabecular bone with unchanged mineral content and highly compliant ductile-like demineralized trabecular bone and polymer-based ACMs, respectively. For ACMs, the energetic-based fracture toughness of the systems turned out to be insensitive to the porosity level. This was verified over a wide range of porosity, until quasi-*continuum*-like conditions, in correspondence of which the structural interaction between filaments changed, were approached. At small strains, whereas the response turned out to be strongly dependent on apparent density of the systems, strong variations were once again observed while approaching minimum porosity conditions. In the case of trabecular bone, the fracture toughness turned out to be strongly dependent on the trabecular constituent material (mineral degree). The data for the tissue with unchanged mineral content were successfully compared with relevant literature on simi-

lar systems. In the case of the ductile highly demineralized tissue, the applicability of innovative single specimen approaches based on the Load Separation Criterion, LSC, was examined. First, the LSC was used to explore the possibility to resort to multi-specimen approaches, which was proven wrong, thus supporting the experimental evidence provided by morphological analyses and mechanical tests. Secondly, by resorting to the LSC-based normalization method, the construction of the R-curves - resistance curves where the fracture toughness parameter is expressed as a function of crack advancement - for highly demineralized trabecular bone tissues was attempted.

The development of a reliable, brand new testing and data elaboration methodology for the study of structural integrity of cellular materials in the framework of FM was assessed. The method was successfully applied to the case of commercial pre-treated (and sometimes even markedly demineralized) heterologous trabecular bone tissues. Alongside the high scientific interest - as a comprehensive mechanical and at fracture characterization was yet to be carried out for such peculiar and complex systems - the importance of the method extends to the industrial area as well, providing fundamental information that would help design, manufacturing and quality control of commercial tissues tailored on the specific application in regenerative medicine.

Contents

1	Introduction	I
2	Fracture Mechanics: theoretical background	15
3	Architected ductile polymer cellular model structures produced by 3D printing	33
3.1	Additive manufacturing of ACMs	33
3.2	Experimental	37
	Material and fabrication of the structures	37
	Characterization	44
	Morphological analyses and density measurements	44
	Mechanical tests	47
3.3	Results and discussion	55
	Morphology and density of the structures	55
	Mechanical behaviour	57
	Tensile tests on ABS filament	57
	Compression tests	59
	Tensile tests	70
	Fracture behaviour	73
4	Trabecular bone tissues used as heterologous bone grafts	91

CONTENTS

4.1	Trabecular bone: introduction and applications in regenerative medicine	91
4.2	Materials and methods	97
	Materials	97
	Methods	100
	Density measurement	100
	Morphology-based classification of the specimens for the mechanical characterization	100
	Mechanical tests	103
	Fracture tests	109
4.3	Results and Discussion	111
	Morphology and density	111
	Mechanical response in compression	113
	Monotonic tests	113
	Cyclic tests	127
	Creep tests	133
	Mechanical response in bending	136
	Fracture response	137
	Morphology of the structures	137
	Fracture data elaboration	143
	Fracture toughness	145
	Load Separation Criterion (LSC)	152
	Conclusions	167
	Future perspectives	175
	Acknowledgments	177
	Bibliography	179

I Introduction

Cellular materials: an overview

As the need for lightweight materials with adequate stiffness, strength and reliability over time, emerged as a critical issue in high-performance industry – automotive, aerospace, biomedical and sport – innovation in materials development became a crucial topic in scientific research. Indeed, in parallel with research and production of brand-new materials for the manufacturing of bulk components (*continuum*), a growing interest in the study of porous systems emerged in recent years. The reason for such inflating demand lies in their unique properties, not dependent on the bulk material only, but rather strongly influenced by their specific architectural parameters as well. A widely employed classification criterion consists in considering the degree of regularity of the systems, as well as the possibility for design optimization. Alongside foams, whose random (stochastic) structure – either of natural origin or manufactured *via* processes where control over geometrical and architectural parameters is limited – was studied in well-established in literature,¹ particular attention is currently being focused on Architected Cellular Materials, ACMs, character-

¹Lorna J. Gibson and Michael F. Ashby, *Cellular solids: Structure and properties, second edition* (Cambridge University Press, January 1997), 510, ISBN: 9781139878326, <https://doi.org/10.1017/CBO9781139878326>.

ized by periodic structure governed by a limited set of parameters easy-tailorable in design phase. "ACMs" and "Lattice Structures" are terms often used interchangeably, especially when nodes and struts are involved in the description of the systems as their building blocks. As both categories are commonly referred to as "cellular" materials, the same nomenclature is adopted here: however, keeping in mind the nature of their fundamental differences would prevent the engendered recurrent misunderstandings. Cellular materials can be classified on the basis of the degree of porosity interconnectivity, high in open-celled, low in closed-celled structures. Open cells are extremely functional when permability to fluid flow is a demanding requirement, such as in biomedical applications, as promoters of nutrient transport and cell proliferation and differentiation. Further, the possibility to reach extremely high surface-to-volume ratios makes them perfect in industrial applications in the energy field, as heat exchangers and thermal management components. Conversely, structures where edges and faces of cells are solid (closed-cell) are particularly suitable for insulation purposes, both acoustic and thermal. In general, the possibility for high-energy absorption raised interest in the sports sector, as light-weight yet highly-dissipative headgears are required to guarantee safety and protection to athletes.

Stochastic foams

Cellular materials, in the form of stochastic foams, are quite common in nature. One of the main reason lies in the their capability for mechanical purposes, clearly evident in the case of wood - whose role is to support tree growth and stability - and cancellous bone, whose extremely porous structure, in addition to its stiffness, provides a reliable and yet lightweight frame for animal bodies. In other cases - cork, sponges, stalks and leaves - the foam-like structure develops to optimize the specific properties of interest, may it be to fulfill mandatory requirements like fluid transport, thermal and acoustic insula-

tion and high energy-absorption. Everyday life presents examples of foams, like many starch-based food, where foaming is obtained by using CO₂ or yeast. Inspired by nature, man-made foams were designed and manufactured over time, by relying on a variety of constituent materials, as polymers, metals, ceramics and even highly-brittle glasses. The main applications for these materials are in the energy-absorption - packaging and crash protection - and light-weighting - standalone or as parts in highly heterogeneous materials, such as composites and sandwich panels - fields. The main purpose while relying on these materials can vary over a wide range of possibilities, however their high mechanical properties - stiffness and strength - especially when considered alongside their low density, always represent an highly-desirable buff.

Architected Cellular Materials, ACMs

The possibility to tailor the architectural parameters to obtain predictable results on the systems' properties - in addition to their inherent light-weighting nature - led to the use of "intelligent materials" or "meta-materials" as common terminology when referring to ACMs. The term "meta-materials" was also used to indicate that they can show physical properties absent in the constituent materials and originated from the specific architecture.² The versatility of such approach lies in the possibility to act on a very local scale, providing specific levels of the desired property (reinforcement, compliance...), by tuning local density, strut thickness and other geometrical parameters. A specific sub-category of ACMs, which is raising growing interest, is represented by minimal surfaces - structures made of curved sheets where connections are not provided by clearly-identifiable nodes - among which Triply Periodical Minimal Surfaces, TPMS, stand out.

²Meisam Askari et al., "Additive manufacturing of metamaterials: A review," *Additive Manufacturing* 36, no. September (2020): 101562, ISSN: 22148604, <https://doi.org/10.1016/j.addma.2020.101562>.

The synergistic effect of geometry and material, in addition to the possibility to tailor their mutual influence on global response, allowed to obtain unique and unprecedented property combinations, which could not be reached in the framework of *continuum* design. However, industrial high-performance applications require extremely property reliability in order to adopt ACMs as a broad scale solution. This, in addition to the high degree of geometrical complexity, whose realization put traditional manufacturing processes in severe trouble, confined ACMs almost only to academic and prototyping purposes. The situation was going to face a fundamental turning point when ACMs met Additive Manufacturing, AM, as a synergistic effect was going to establish between the two highly-innovative - but still far from being established and widespread - spheres.

Fracture in cellular materials

Fracture mechanics (FM) is the branch of mechanics whose aim consists in the study of the behaviour of solids containing flaws or cracks. In particular, the presence of geometrical inhomogeneities, defects and cracks leads to the premature failure of the component, at much lower stresses than those expected by *continuum* mechanics theory and design. The importance of flaw geometry and size can not be stressed enough. It represents a further variable concurring to the definition of design criteria, in addition to applied stress and the material property. In the case of FM, the material property is represented by fracture toughness, which can be described as the resistance offered by a material to the generation of new fracture surfaces, when subjected to external forces.³ More details about FM, including the theoretical approaches developed over time, are reported in Section 2.

³T.L. Anderson, *Fracture Mechanics : Fundamentals and Applications* (CRC Press, March 2017), ISBN: 9781315370293, <https://doi.org/10.1201/9781315370293>.

FM approaches developed for *continuum* were extended to cellular materials, especially for ACMs, whose regular structure could be described by using theoretical relationships, but also to the case of stochastic foams. Different constituent materials were examined in stochastic foams literature. Within natural materials, trabecular bone,⁴ wood,⁵ cork⁶ and bread⁷ were studied for the determination of their fracture toughness. Regarding laboratory-made foams, the materials addressed in the framework of FM include metals^{8,9},¹⁰ ceramics,¹¹ carbon¹² and polymers.¹³ Conversely, relevant literature

⁴R. B. Cook and P. Zioupos, "The fracture toughness of cancellous bone," *Journal of Biomechanics* 42, no. 13 (September 2009): 2054–2060, ISSN: 00219290, <https://doi.org/10.1016/j.jbiomech.2009.06.001>.

⁵Noah Matsumoto and John A Nairn, "Fracture toughness of wood and wood composites during crack propagation," *Wood and Fiber Science* 44, no. 2 (2012): 121–133.

⁶M. E. Rosa and M. A. Fortes, "Deformation and fracture of cork in tension," *Journal of Materials Science* 26, no. 2 (1991): 341–348, ISSN: 00222461, <https://doi.org/10.1007/BF00576525>.

⁷M. G. Scanlon, D. Fahloul, and H. D. Sapirstein, "A Measure of Fracture Toughness of Bread Crumb," *Cereal Chemistry* 74, no. 5 (1997): 612–613, ISSN: 0009-0352, <https://doi.org/10.1094/cchem.1997.74.5.612>.

⁸K. Y.G. McCullough, N. A. Fleck, and M. F. Ashby, "Toughness of aluminum alloy foams," *Acta Materialia* 47, no. 8 (1999): 2331–2343, ISSN: 13596454, [https://doi.org/10.1016/S1359-6454\(99\)00125-1](https://doi.org/10.1016/S1359-6454(99)00125-1).

⁹X. Badiche et al., "Mechanical properties and non-homogeneous deformation of open-cell nickel foams: Application of the mechanics of cellular solids and of porous materials," *Materials Science and Engineering A* 289, no. 1 (2000): 276–288, ISSN: 09215093, [https://doi.org/10.1016/S0921-5093\(00\)00898-4](https://doi.org/10.1016/S0921-5093(00)00898-4).

¹⁰Sadaf Kashef et al., "Fracture mechanics of stainless steel foams," *Materials Science and Engineering: A* 578 (2013): 115–124, ISSN: 09215093, <https://doi.org/10.1016/j.msea.2013.03.062>.

¹¹Jung Hye Eom, Young Wook Kim, and Santosh Raju, "Processing and properties of macroporous silicon carbide ceramics: A review," *Journal of Asian Ceramic Societies* 1, no. 3 (2013): 220–242, ISSN: 21870764, <https://doi.org/10.1016/j.jascer.2013.07.003>.

¹²S. Choi and B. V. Sankar, "Fracture Toughness of Carbon Foam," *Journal of Composite Materials* 37, no. 23 (2003): 2101–2116, ISSN: 00219983, <https://doi.org/10.1177/002199803036264>.

¹³Liviu Marşavina and Emanoil Linul, "Fracture toughness of rigid polymeric

about ACMs pointed out the effect of cell geometry, size and spacial repetition, in addition to the material properties provided by the specific constituent material selected.^{14, 15, 16} Indeed, the fracture toughness of high architectural complexity structures, like octet trusses¹⁷ and Triply Periodic Minimal Surfaces, TMPS,¹⁸ was investigated in the recent years.

When considering systems with relevant porosity degree ($\geq 70\%$), the concept itself of defect has to be carefully questioned. In *continuum*, large defects are supposed to preferentially guide crack propagation. Is it still valid for cellular materials? What about the nature of crack front and of the new surfaces generated during fracture propagation? Relevant literature about cellular materials proposed examples derived from natural stochastic foams¹⁹ and theoretical models developed for ACMs,²⁰ to tackle these questions (Figure 1.1).

foams: A review,” *Fatigue and Fracture of Engineering Materials and Structures* 43, no. 11 (2020): 2483–2514, ISSN: 14602695, <https://doi.org/10.1111/ffe.13327>.

¹⁴Seon Ju Yeo, Min Jun Oh, and Pil J. Yoo, “Structurally Controlled Cellular Architectures for High-Performance Ultra-Lightweight Materials,” *Advanced Materials* 31, no. 34 (2019): 1–26, ISSN: 15214095, <https://doi.org/10.1002/adma.201803670>.

¹⁵Angkur Jyoti Dipanka Shaikeea et al., “The toughness of mechanical metamaterials,” *Nature Materials* 21, no. 3 (2022): 297–304, ISSN: 1476-4660, <https://doi.org/10.1038/s41563-021-01182-1>.

¹⁶James Utama Surjadi and Yang Lu, “Design criteria for tough metamaterials,” *Nature Materials* 21, no. 3 (2022): 272–274, ISSN: 14764660, <https://doi.org/10.1038/s41563-022-01193-6>.

¹⁷M. R. O’Masta et al., “The fracture toughness of octet-truss lattices,” *Journal of the Mechanics and Physics of Solids* 98, no. September 2016 (2017): 271–289, ISSN: 00225096, <https://doi.org/10.1016/j.jmps.2016.09.009>.

¹⁸Abdulla Almomani and Abdel Hamid I. Mourad, “The fracture toughness of Schwarz Primitive triply periodic minimal surface lattice,” *Theoretical and Applied Fracture Mechanics* 125, no. May (2023): 103924, ISSN: 01678442, <https://doi.org/10.1016/j.tafmec.2023.103924>.

¹⁹R. B. Cook et al., “Fracture toughness and compressive properties of cancellous bone at the head of the femur and relationships to non-invasive skeletal assessment measurements,” *Medical Engineering and Physics* 32, no. 9 (2010): 991–997, ISSN: 13504533, <https://doi.org/10.1016/j.medengphy.2010.06.014>.

²⁰Gibson and Ashby, *Cellular solids: Structure and properties, second edition*.

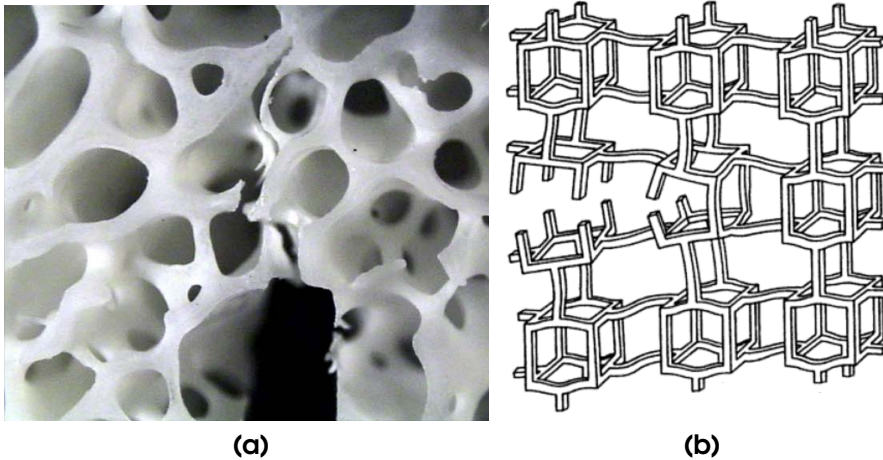


Figure 1.1: Examples of cellular materials of natural and artificial origin: (a) stochastic-foam-like trabecular bone, adapted from [Cook et al., “Fracture toughness and compressive properties of cancellous bone at the head of the femur and relationships to non-invasive skeletal assessment measurements”]; (b) ACM, adapted from [Gibson and Ashby, *Cellular solids: Structure and properties, second edition*].

Regarding ACMs, the application of FM theory led to the development of a solid theoretical basis, according to which the fracture toughness results dependent on the geometrical parameters of the systems (cell size and strut thickness), as well as on their fracture strength and normalized (relative) density. The tensional approach, which involves the evaluation of the stress field around crack tip and its evolution during load application, was widely applied for the determination of fracture toughness. Further, as literature focused the attention mainly on brittle-like response materials, Linear Elastic Fracture Mechanics (LEFM, see Section 2 for more details) was consolidated as reference scheme.²¹

²¹J. S. Huang and L. J. Gibson, “Fracture toughness of brittle foams,” *Acta Metallurgica Et Materialia* 39, no. 7 (1991): 1627–1636, ISSN: 09567151, [https://doi.org/10.1016/0956-7151\(91\)90250-5](https://doi.org/10.1016/0956-7151(91)90250-5).

Conversely, the extension of the theoretical relationships to the case of stochastic foams was not straightforward, as structural and material heterogeneity invalidated the regularity hypothesis. Indeed, natural stochastic foams required even further attention, as they present specific features depending on their architecture and composition. Thus, after suitable models were developed for each case, experimental studies - which gained increasing importance - were needed to support the analysis. The fracture toughness of these systems, once again evaluated in the framework of LEFM and applying the tensional approach, turned out to be dependent on the normalized (relative) density.

Indeed, a power-law dependency of fracture toughness on relative density was recorded for both ACMs and stochastic foams. The value of the power was provided by a specific physical significance, the exact same way it was carried out in the study of stiffness and strength of cellular materials in fundamental mechanical characterization.²² The results for a representative open-celled ACM and natural stochastic foam (wood) were reported in Figure 1.2. The graph was reported in normalized form for open-celled ACM, while using just fracture toughness for wood. A power of $3/2$ describes the response of both materials.

According to Gibson and Ashby²², the value $3/2$ is suitable for the description of the normalized fracture toughness dependency on relative density for cancellous bone as well. However, such statement is not supported by experimental data, relying only on the theoretical framework obtained by modeling it as an equiaxed foam. Despite the lack of consolidated literature, Cook and Zioupos²³ performed an experimental fracture characterization of trabecular bone tissues, by testing the specimens both in parallel and orthogonally to the main trabecular orientation, according to which a power value of ≈ 1.6 was determined. The data were represented in non-normalized form (fracture toughness vs apparent density), as the determination of

²²Gibson and Ashby, *Cellular solids: Structure and properties, second edition*.

²³Cook and Zioupos, "The fracture toughness of cancellous bone."

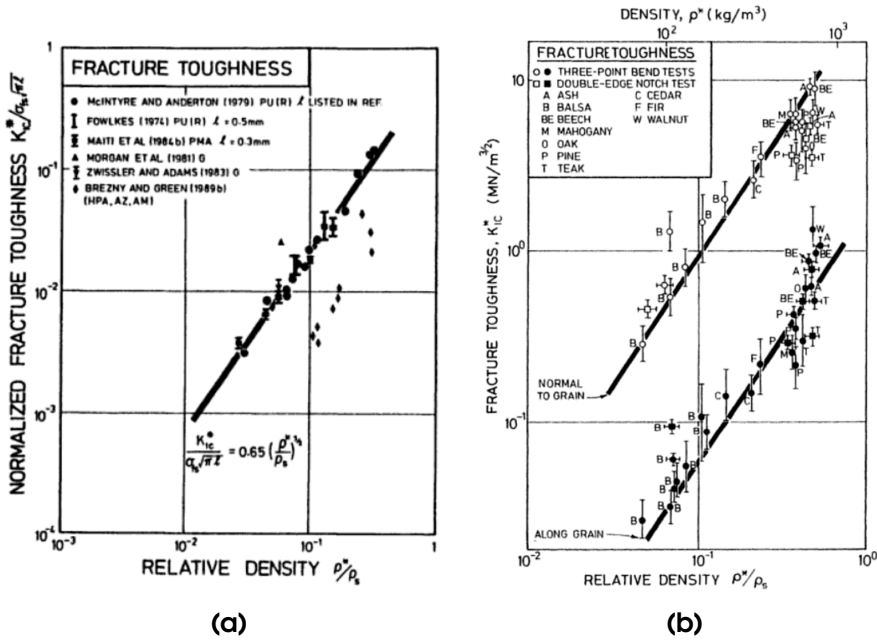


Figure 1.2: Fracture toughness of cellular materials against relative density in the case of (a) ACM (in normalized terms) and (b) stochastic-foam-like wood, adapted from [Gibson and Ashby, *Cellular solids: Structure and properties, second edition*]. Power-law trends with power of 3/2 - suitable to describe the response of both materials - are represented with full lines.

fracture toughness and density of the constituent material is complex due to its heterogeneous nature (Figure 1.3)

Aim of the research

The research was meant to study the structural integrity of cellular materials, and a twofold aim was pursued:

- the development of solid testing and data elaboration methods, especially in the framework of Fracture Mechanics, FM;

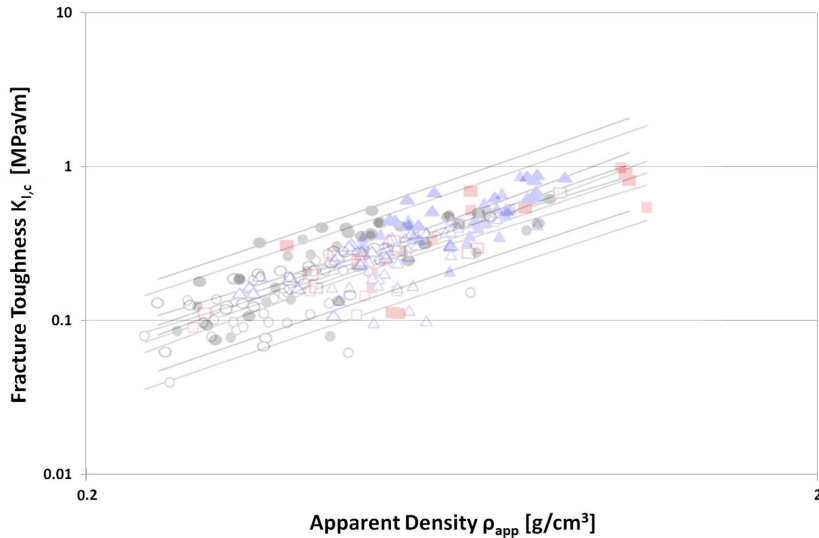


Figure 1.3: Fracture toughness vs apparent density of trabecular bone tissues tested both in parallel and orthogonally to the main trabecular orientation, adapted from [Cook and Zioupos, “The fracture toughness of cancellous bone”] Power-law trends with power ≈ 1.6 are indicated with full lines in bi-logarithmic axes.

- the research of structure-property relationships, performed by relying on the previously developed and validated testing and data elaboration methods.

As the pool of cellular materials is extremely various, making impossible an exhaustive characterization, the attention was focused on two cellular materials, considered as representative cases for both stochastic foams and ACMs. With regards to stochastic foams, trabecular bone was studied. Its high structural complexity and heterogeneity degree even with regards to material composition, suggested the possibility to address specific methodological problems for the study of structural integrity on way simpler structures. Thus, polymer-based ACMs were manufactured via AM techniques. Once the method was fully developed, the structural integrity of both trabecular bone tis-

sues and ACMs was extensively studied.

The analysis of relevant literature about cellular solids, and in particular on both ACMs and trabecular bone, led to theoretical and methodological limitations to be detected: 1) the closed solution, which can be derived from mathematical deductions for geometrically regular structures, can not be straightforwardly applied when relevant architectural and material heterogeneity occurs; 2) thus, the FM tensional approach traditionally applied, progressively loses its ability to predict the system response, requiring to resort to Finite Element Modeling (FEM) techniques - which can show a certain degree of inaccuracy, as heterogeneity at the constituent material level could induce troubles during modeling; 3) further, for materials showing marked non-linearity and relevant plasticity, the use of LEFM is no longer allowed, resulting in the need for other approaches - to deal with the elastic-plastic behaviour - to emerge. The present research addressed such problems recorded in literature, by developing strategies aimed at their solution. First, a bottom-up approach was adopted, according to which the attention was focused on experimental data, that would eventually led to the determination of structure-property relationships. It was preferred over the top-down approach, as it allowed the peculiar nature of each complex system to emerge. A comparison with the theoretical relationships proposed in literature was eventually carried out. Then, the architectural and material heterogeneity led to discard the tensional Fracture Mechanics approach - based on the stress intensity factor concept - as it requires the knowledge of the stress field in the region surrounding crack tip, whose determination is extremely difficult for such complex systems. Conversely, the energetic approach - which addresses the study of fracture process on a more global scale - had the chance to shine. It is completely independent on the local stress distribution, being only dependent on the system's energy variation - in addition to its geometry - which can be easily evaluated directly from loading curves. Further, as plasticity was observed as a peculiar mechanism for trabecular bone, especially in the case of the demineralized tissue,

Elastic Plastic Fracture Mechanics (EPFM) approaches were adopted. Indeed, the tissues with unchanged mineral content - where plasticity, even if present, is quite limited - were studied according to LEFM (as proposed in literature), while the ductile-like demineralized tissues, as well as ABS-based ACMs used as "model" structures, were addressed in the framework of EPFM. Finally, specific fundamental and methodological issues concerning the applicability of laboratory testing-schemes to the study of the structural integrity of cellular materials were studied in detail. Indeed, they were firstly addressed on ABS-based ACMs, before being extended to the case of trabecular bone once validated. In particular, relevant literature about fracture testing of *continuum* ductile polymers²⁴ provided some tools to investigate notching, fracture initiation, the contribution of specimen local indentation (especially in the more compliant systems) and the effect on local density on fracture response of the structures. In the case of ductile-like demineralized bone tissue, the possibility to rely on innovative FM approaches, based on the Load Separation Principle (LSC)²⁵ was investigated. In the framework of LSC, the applicability of multispecimen approaches was neglected, as each specimen gained increased importance due to the unique nature of its architectural and material features. Further, resistance R-curves, in which the fracture toughness varies as a function of crack advancement, were studied. The determination of R-curves, while being used as an important tool in the study of fracture behaviour of cortical bone,²⁶ has never been attempted before in literature about trabecular bone, providing this

²⁴D.R. Moore, J.G. Williams, and A. Pavan, *Fracture mechanics testing methods for polymers, adhesives and composites* (Elsevier Sci Ltd, 2001), 388, ISBN: 9780080531960.

²⁵M.H. Sharobeam and J.D. Landes, "The load separation criterion and methodology in ductile fracture mechanics," *International Journal of Fracture* 47 (1991): 81-104.

²⁶K J Koester, H D Barth, and R O Ritchie, "Effect of aging on the transverse toughness of human cortical bone : Evaluation by R-curves," *Journal of the Mechanical Behavior of Biomedical Materials* 4, no. 7 (2011): 1504-1513, ISSN: 1751-6161, <https://doi.org/10.1016/j.jmbbm.2011.05.020>.

final step a fundamental novelty character, whose impact affects both scientific and industrial world.

2 Fracture Mechanics: theoretical background

Introduction to Fracture Mechanics, FM

Fracture mechanics is the branch of mechanics whose aim consists in the study of the behaviour of solids containing flaws or cracks - either accidentally occurred during commissioning and in service, or already existent as either geometrical elements characterizing them or microstructural inhomogeneities due to production, manufacturing and shaping problems. Fracture mechanics developed - mainly during the last century - with the intent to explain the underlying mechanisms leading some objects to incur in failure at stress values significantly lower than the ones expected on the grounds of yield and ultimate strength properties evaluated thanks to standard laboratory tests.¹

When solids are mechanically stressed, the presence of a crack or a geometrical inhomogeneity results in the promotion of a local stress intensification effect in the proximity of the crack tip, which is the main responsible for the fracture-caused - intended as the generation of new surfaces - failure. In the framework of fracture mechanics, the response of a solid is described by relying on parameters that assume

¹Anderson, *Fracture Mechanics : Fundamentals and Applications*.

a critical value - which characterizes the specific material considered - in correspondence of fracture initiation. Considering one of these parameters - labelled Γ for the sake of simplicity - the Γ -value for a mechanically stressed solid is in general a function of its geometry, constraints and the configuration of the applied forces. The structural integrity verification is based on the comparison between the Γ -value for the concerned mechanical system and the critical value Γ_c - which is an intrinsic property of the specific material representing its fracture resistance (fracture toughness). As a consequence, *continuum* mechanics and fracture mechanics share the same general formulation for resistance criterions, where the second member of the equation is the material property determined as a result of experimental tests. However, the fundamental difference lies in the combination of parameters required to define them. In the framework of *continuum* mechanics, the anticipated design stress is compared with the flow properties of candidate materials; a material is assumed to be suitable for the desired purposes if its strength is greater than the expected applied stress. Recognizing that brittle fracture is the worst and most dangerous failure cause for the component, such an approach may attempt to guard against it by imposing a safety factor on stress, combined with minimum tensile elongation requirements on the material. The fracture mechanics approach has three important variables, rather than the two characterizing the continuum mechanics, as shown in Figure 2.1. The additional structural variable is flaw size, while fracture toughness replaces strength as the critical material property. Fracture mechanics is responsible for the quantification of the critical combinations of these three variables: as a matter of fact, in order to apply fracture mechanics concepts to design, a mathematical relationship between toughness, stress, and flaw size is required. An homogeneous solid containing a crack and mechanically stressed, may incur in failure at stresses significantly lower than the critical value expected by the continuum mechanics criterion of resistance: thus, as the flaw size has to be included in the analysis, fracture mechanics criterions are required.

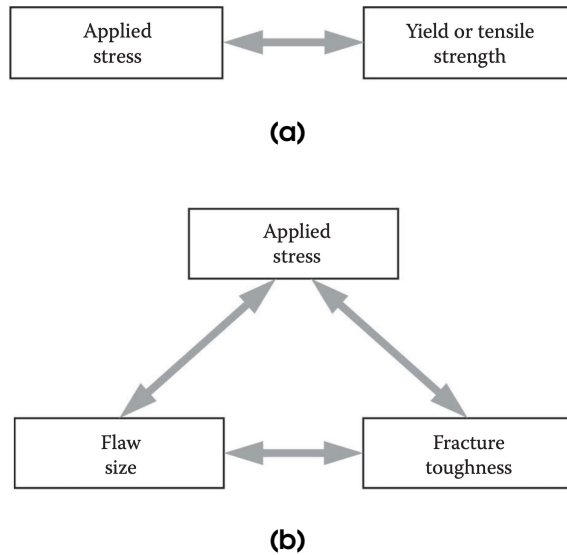


Figure 2.1: Comparison of (a) *continuum* mechanics and (b) fracture mechanics approaches, adapted from [Anderson, *Fracture Mechanics : Fundamentals and Applications*].

Linear Elastic Fracture Mechanics, LEFM

The Linear Elastic Fracture Mechanics (LEFM) is the simplest and firstly developed model to describe the fracture response of linear time-independent materials (Figure 2.7). More specifically, LEFM field of application consists in materials showing brittle response and linear elastic behaviour - as a matter of fact, Griffith² introduces the energy release rate as the key parameter to describe fracture resistance of extremely brittle glasses, laying the foundations for LEFM further development. Actually, LEFM can be extended to materials that show a little plasticity in the proximity of the crack tip. There are two alternative approaches to fracture analysis, the stress inten-

²A.A. Griffith, "The phenomena of rupture and flow in solids," *Philosophical Transactions of the Royal Society of London* 221 (1920): 163–198, ISSN: 00254576, <https://doi.org/10.1098/rsta.1921.0006>.

sity criterion and the energy criterion. For LEFM, the parameter Γ assumes different names and meanings depending on the approach considered - *i.e.* the stress intensity factor K and the energy release rate G respectively. It is worth pointing out that three different loading modes can be applied to a crack during the execution of fracture tests, as displayed in Figure 2.2:

- **Mode I** is the opening configuration and represents the most critical situation as it induces tensile stresses at the crack tip that encourage crack propagation (on the contrary, compression stresses tend to close and slow down the fracture process): for this reason, combined with the simplicity of the experimental apparatus required, it is the most widely used method;
- **Mode II** is the in-plane shear configuration, that induces shear stresses at the crack tip that lay in the crack plane;
- **Mode III** is the out-of-plane shear configuration, that induces shear stresses at the crack tip that lay in a plane orthogonal to the crack plane.

LEFM is the basic scheme used for the definition of the elastic modulus, determined from the elastic compliance from fracture tests, E_f ³ and it is based on two fundamental assumptions:

- all energy dissipation is associated with the fracture process;
- the deformation which occurs is linear elastic.

LEFM allows to describe situations like brittle failures in polymers and impact tests relying on simple methods - in contrast to metals and ductile polymers testing, for example, where plasticity and nonlinear effects can not be ruled out. It is worth pointing out that the following equations and considerations refer to plane stress configuration.⁴ As

³Moore, Williams, and Pavan, *Fracture mechanics testing methods for polymers, adhesives and composites*.

⁴Anderson, *Fracture Mechanics : Fundamentals and Applications*.

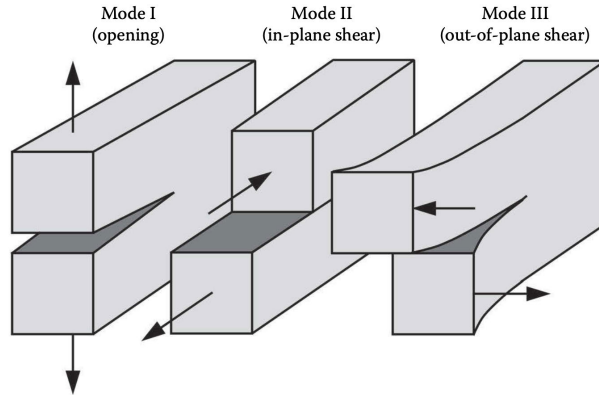


Figure 2.2: Schematic representation of the three loading modes that can be applied to a crack, adapted from [Anderson, *Fracture Mechanics : Fundamentals and Applications*].

already mentioned, LEFM describes the energy change which occurs in a linear elastic body already containing a sharp crack when it undergoes an increase in crack area (nothing can be said about the generation of new cracks in otherwise flawless bodies). More in detail, the fundamental parameter is the energy release rate (G) which is defined as the energy release rate during the crack growth - a measure of the energy available for an increment in crack extension

$$G = \frac{dU}{dA} \quad (2.1)$$

where dU is the energy variation - defined as the difference between the internal strain energy in the body and the work made by external forces - and dA is the area increase. Since dA is taken as positive for crack growth, a positive dU and hence G implies a positive energy release, which is the driving force for the crack growth overcoming the fracture resistance (G_c). Therefore, at fracture

$$G = \frac{dU}{dA} = \frac{dU}{B \cdot da} = G_c \quad (2.2)$$

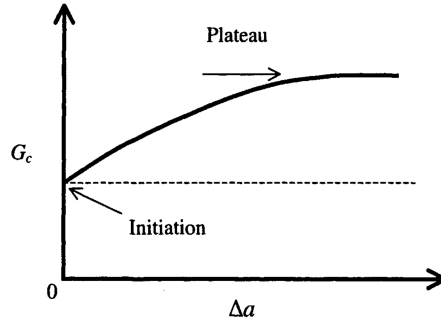


Figure 2.3: Resistance curve (R-curve), adapted from [Moore, Williams, and Pavan, *Fracture mechanics testing methods for polymers, adhesives and composites*].

where a is the crack length for a uniform thickness, B . It is worth noting that G is determined by the loading and geometry of the cracked body while G_c is a material property and is the energy per unit area necessary to create the new surface area of the crack, taking into account the effects of micro-mechanisms occurring in the region of the crack tip. An important aspect of fracture resistance G_c is that it may vary as the crack grows such that G_c is a function of the crack growth Δa (and this is one of the main differences between continuum and fracture mechanics): this typically rising G_c - Δa curve, which is termed the resistance or R-curve (see Figure 2.3), provides a complete description of the material's fracture toughness and its importance is such that specific testing methods have been specially developed to its determination.

For many beam-like specimens, it is possible to measure their stiffness, or more conveniently compliance C ($= (\text{stiffness})^{-1}$) as a function of crack length. For all loading systems, G may be defined as

$$G = \frac{dU}{dA} = \frac{dU_{ext}}{dA} - \frac{dU_s}{dA} - \frac{dU_k}{dA} - \frac{dU_d}{dA} \quad (2.3)$$

where U_{ext} is the external work, U_s is the strain energy, U_k is the kinetic

energy, U_d is the dissipated energy and $dA = Bda$ is the variation in crack area for a uniform thickness, B . For low testing rate $U_k = 0$ and if all the energy dissipation is concentrated at the crack tip $U_d = 0$. On the grounds of the LEFM load-deflection lines shown in Figure 2.4, in which the compliance increases while $a \rightarrow a + da$, the energy variations are

$$dU_{ext} = Pdu \quad (2.4)$$

and

$$U_s = \frac{1}{2}Pu \quad \implies \quad dU_s = \frac{1}{2}(Pdu + udP) \quad (2.5)$$

therefore G , which represents the energy variation represented by the shaded area in Figure 2.4 and has the following formulation:

$$G = \frac{1}{2B} \left(\frac{Pdu}{da} - \frac{udP}{da} \right) \quad (2.6)$$

By introducing the compliance definition

$$u = C \cdot P \quad \implies \quad du = CdP + PdC \quad (2.7)$$

and substituting it in equation (2.6), it is possible to express G in terms of the compliance C :

$$G = \frac{P^2}{2B} \frac{dC}{da} = \frac{Pu}{2B} \frac{1}{C} \frac{dC}{da} = \frac{u^2}{2B} \frac{1}{C^2} \frac{dC}{da} \quad (2.8)$$

Thus if $C(a)$ is known, dC/da may be found and hence G calculated from either load, load and displacement, and displacement alone.

Some geometries of practical interest do not lend themselves well to analysis via compliance measurements. Plates in tension and bending are examples and, although equations (2.8) are still formally correct, it is very difficult to obtain dC/da experimentally. A more accurate method consists in switching from the "energetic approach" to the "tensional approach" and considering the local stress field around the crack tip which has the form

$$\sigma = \frac{K}{\sqrt{2\pi r}} f(\theta) \quad f(0) = 1 \quad (2.9)$$

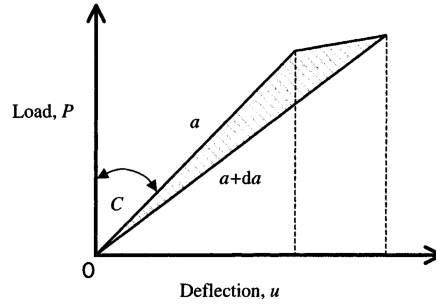


Figure 2.4: Load-deflection curves for LEFM, adapted from [Moore, Williams, and Pavan, *Fracture mechanics testing methods for polymers, adhesives and composites*].

where r is the distance from the crack tip and θ is the angle measured from the crack line. The stresses are singular as $r \rightarrow 0$ but the product $\sigma\sqrt{r}$ remains finite and is characterized by the Stress Intensity Factor K , which appears in two important relationships for specimen calibration: firstly, a generally valid equation that relates K and G

$$K^2 = EG \quad (2.10)$$

and then a relationship valid for the generic case of a large plate containing a central crack of length $2a$ subjected to a uniform stress σ

$$K^2 = \sigma^2 \pi a \quad (2.11)$$

whose combination allows to express G in terms of the elastic modulus E :

$$G = \frac{\sigma^2 \pi a}{E} \quad (2.12)$$

Noting that $\sigma = P/BW$, where W is the width, from equations (2.8) and (2.12) it is possible to obtain

$$\frac{dC}{d\alpha} = \frac{2\pi}{EB} \alpha \quad \alpha = \frac{a}{W} \quad (2.13)$$

The calibration factor is a function of α , leading to the general definition of stress intensity factor K

$$K = f(\alpha) \frac{P}{B\sqrt{W}} \quad (2.14)$$

where $f(\alpha) = \sqrt{\pi\alpha}$ in the case of a crack of length $2a$ in an infinite plate subject to a remote tensile stress σ . It is possible to express G_c in terms of $dC/d\alpha$ using the second of equations (2.8)

$$G_c = \frac{U_s}{BW} \left(\frac{1}{C} \frac{dC}{d\alpha} \right) = \frac{U_s}{BW\phi(\alpha)} \quad (2.15)$$

and eventually the elastic modulus E as a function of $f(\alpha)$ and $\phi(\alpha)$

$$E = \frac{2}{B} \frac{f^2}{dC/d\alpha} = \frac{2}{BC} f^2 \phi \quad (2.16)$$

The general analytical expression for $f(\alpha)$ and $\phi(\alpha)$ - which can be deduced from $f(\alpha)$ once the compliance at $\alpha = 0$ (C_u where u refers to the uncracked specimen) has been esteemed

$$\frac{dC}{d\alpha} = \frac{2}{EB} f^2(\alpha) \quad ; \quad \phi(\alpha) = \frac{1}{f^2(\alpha)} \left[\frac{EB}{2} C_0 + \int_0^\alpha f^2(\alpha) d\alpha \right] \quad (2.17)$$

can be applied to the case of SE(B) geometry with $S/W = 4$, resulting in

$$f(\alpha) = 6\alpha^{\frac{1}{2}} \frac{[1.99 - \alpha(1 - \alpha)(2.15 - 3.93\alpha + 2.7\alpha^2)]}{(1 + 2\alpha)(1 - \alpha)^{\frac{3}{2}}} \quad (2.18)$$

$$\phi(\alpha) = \frac{A + 18.64}{dA/d\alpha} \quad (2.19)$$

where

$$A = \frac{16\alpha^2}{(1-\alpha)^2} \left[8.9 - 33.717\alpha + 79.616\alpha^2 - 112.952\alpha^3 + 84.815\alpha^4 - 25.672\alpha^5 \right] \quad (2.20)$$

and

$$\begin{aligned} dA/d\alpha = \frac{16\alpha^2}{(1-\alpha)^2} \left[-33.717 + 159.232\alpha - 338.856\alpha^2 + 339.26\alpha^3 - 128.36\alpha^4 \right] + 16 \left[8.9 - 33.717\alpha + 79.616\alpha^2 - 112.952\alpha^3 + 84.815\alpha^4 - 25.672\alpha^5 \right] \left[\frac{2\alpha(1-\alpha) + 2\alpha^2}{(1-\alpha)^3} \right] \quad (2.21) \end{aligned}$$

Equation (2.16), as well as the $f(\alpha)$ (2.18) and $\phi(\alpha)$ (2.19), (2.20), (2.21) relationships for SE(B) specimen, will be used later to obtain the elastic modulus - calculated from the compliance determined in fracture tests - E_f for specific materials. In the framework of LEFM, it is important to point out that

$$E_f = \begin{cases} E & \text{in plane stress} \\ E/(1-\nu^2) & \text{in plane strain} \end{cases} \quad (2.22)$$

according to which the elastic modulus from fracture tests E_f and the Young's modulus E are coincident in plane stress conditions, while the contribution of the Poisson's ratio ν cannot be overlooked in case of plane strain conditions.⁵

Elastic Plastic Fracture Mechanics, EPFM

Materials showing nonlinear elastic and elastic-plastic mechanical behaviour (Figure 2.5) invalidate the LEFM, resulting in the need for proper theoretical apparatus that correctly describes them. Referring

⁵Anderson, *Fracture Mechanics : Fundamentals and Applications*.

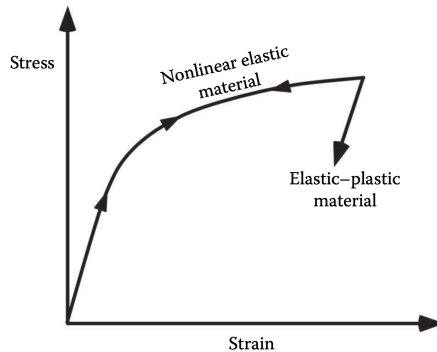


Figure 2.5: Schematic comparison of the stress-strain behavior of nonlinear elastic and elastic-plastic materials, adapted from [Anderson, *Fracture Mechanics : Fundamentals and Applications*].

to Figure 2.7, the suitable models developed are Elastic-Plastic Fracture Mechanics (EPFM) for nonlinear elastic time-independent materials and Dynamic, Viscoelastic and Viscoplastic Fracture Mechanics for time-dependent materials - *i.e.* in the region of the $\log(E)$ - $\log(De)$ graph (Figure 2.8) at low $\log(De)$ values, corresponding to high temperatures and high t_{exp} and thus where the effect of time can not be ruled out anymore.

Although the Crack Tip Opening Displacement (CTOD) was the first-introduced parameter for EPFM - as Wells⁶ proposed the displacement of the crack faces as an alternative fracture criterion when significant plasticity precedes failure - the parameter Γ typically adopted is *J-integral*, that owes the name to the way it was defined: as a matter of fact, when it was presented for the first time by Rice,⁷ it was actually proposed as the line integral of a particular function, to be

⁶A.A. Wells, "Unstable Crack Propagation in Metals: Cleavage and Fast Fracture," *Proceedings of the Crack Propagation Symposium 1* (1961): 84.

⁷J. R. Rice, "A path independent integral and the approximate analysis of strain concentration by notches and cracks," *Journal of Applied Mechanics, Transactions of the ASME* 35, no. 2 (1968): 379–388, ISSN: 15289036, <https://doi.org/10.1115/1.3601206>.

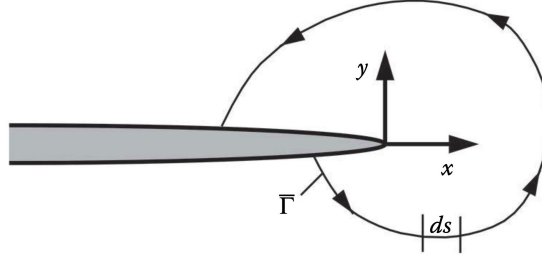


Figure 2.6: Schematic representation of J -integral integration line, adapted from [Anderson, *Fracture Mechanics : Fundamentals and Applications*].

evaluated along a curve that has to include the crack tip of the concerned solid, as shown in Figure 2.6. In particular, Rice showed that the value of the J -integral is independent of the path of integration around the crack, resulting in J being referred as *path-independent* integral as well.

Considering this arbitrary counter-clockwise path $\bar{\Gamma}$, the J -integral is given by

$$J = \int_{\bar{\Gamma}} \left(w dy - T_i \frac{\partial u_i}{\partial x} ds \right) \quad (2.23)$$

where w is the strain energy density, T_i are the components of the traction vector, u_i are the displacement vector components and ds is an infinitesimal length increment along the contour $\bar{\Gamma}$. More specifically, the strain energy density w is defined as

$$w = \int_0^{\epsilon_{ij}} \sigma_{ij} d\epsilon_{ij} \quad (2.24)$$

where σ_{ij} and ϵ_{ij} are the stress and strain tensors, respectively. The traction is a stress vector at a given point on the contour, whose components are given by

$$T_i = \sigma_{ij} n_j \quad (2.25)$$

where n_j are the components of the unit vector normal to $\bar{\Gamma}$.

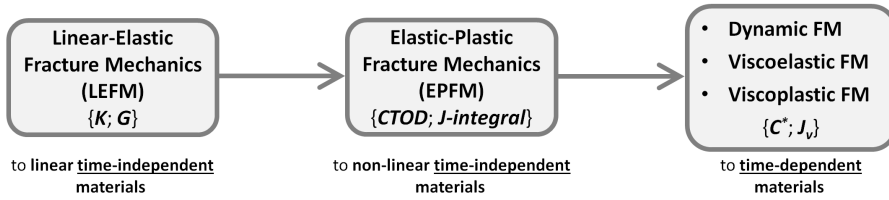


Figure 2.7: Schematic representation of Fracture Mechanics models, specific key parameters and field of application.

Moreover, J -integral was proven to be able to describe the stress intensification effect promoted at the crack tip in a mechanically stressed body as well: as a matter of fact, despite representing the energy release rate in EPFM (just like G in the LEFM), J can be linked to the stress intensity approach as well, by means of HRR equations involving the elastic modulus E .

In the specific case of polymeric materials (*i.e.* viscoelastic), the question arises as to whether the use of time-independent models would be correct and to what extent (Figure 2.7). In the first instance, the viscoelastic contribution could be disregarded since polymeric materials can be considered time-independent under particular conditions.

The region of applicability of the models for time-independent materials on the $\log(E)$ - $\log(De)$ is displayed in Figure 2.8, where E is the elastic modulus of the material and De is the Deborah number. De , which is defined as the ratio between the material-characteristic time $\lambda(T)$ - which is a function of the temperature T - and the experiment time t_{exp} , represents the competition between these two temporal terms: in particular, in the case of low T and short t_{exp} - which is the case of fracture mechanics tests - the material finds itself in the glassy plateau and its response can be legitimately considered time-independent.

In order to determine the J -values for a specific mechanical system, the use of the "integral" definition, although being theoretically correct, is prevented by calculation problems, even invoking the finite

2. FRACTURE MECHANICS: THEORETICAL BACKGROUND

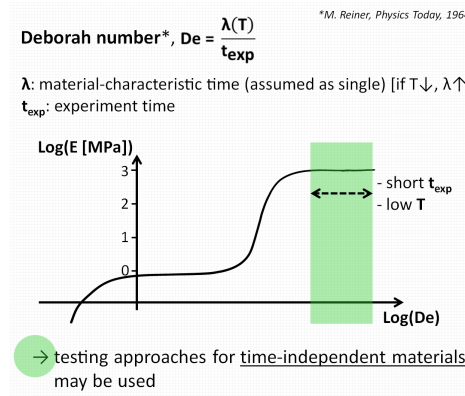


Figure 2.8: Representation of time-independent materials.

elements analysis support, resulting in experimental approaches to be preferred. In particular, the technically simplest method is based on the energetic definition of J -integral. It has been proven that J -integral can be seen as the energy (per unit area) required for the creation of new fracture surfaces and it is defined as G , expressed according to equation (2.1) but for nonlinear elastic materials. This concept can be explained considering a body of uniform thickness B (as well as the fracture mechanics testing specimens) and containing a crack of length a , as shown in Figure 2.9a.

By mechanically stressing the body in such a way to promote crack propagation, as well as laboratory fracture tests require, the loading curve - *i.e.* load-displacement of the element that applies the displacement to the body, in a displacement-control configuration, P - Δ curve - in Figure 2.9b may be obtained. It is worth noting that the curve stops in correspondence of S , which is the point where fracture propagation is supposed to begin. Under the hypothesis of stable crack propagation - as it typically occurs in ductile materials - it will lead to an infinitesimal increment da in crack length during the initial instants of propagation. Considering the loading curve in the situation of $(a + da)$ crack length, both analogy with the case of crack length equal to (a) and experimental evidences suggest that it will

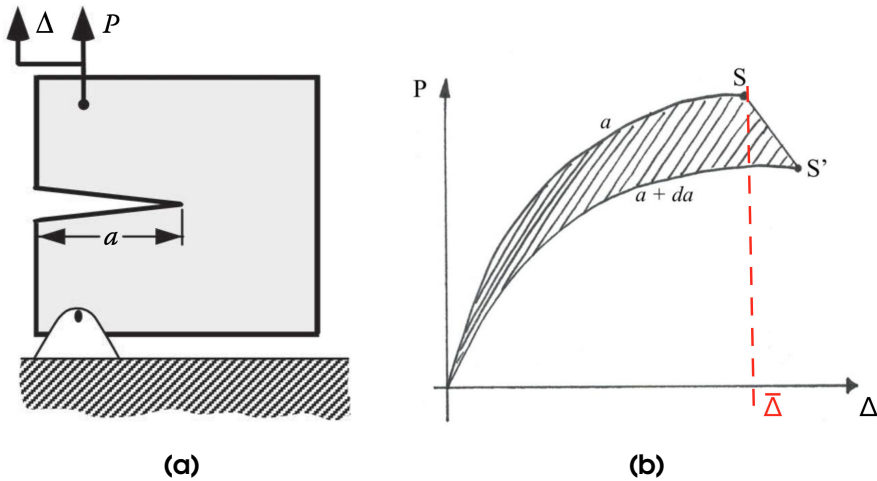


Figure 2.9: *J*-testing experimentals, adapted from [Anderson, *Fracture Mechanics : Fundamentals and Applications*]: (a) schematic representation of a cracked body mechanically stressed in fracture tests; (b) *P*- Δ curves for increasing crack lengths in EPFM (equivalent to LEFM load deflection curves represented in Figure 2.4).

stop at S' , which is the point where the crack propagation is supposed to initiate for $(a+da)$ crack length. It can be shown that the difference in the areas under the *P*- Δ curve corresponding to (a) and $(a + da)$ crack length until the limit point *S* (*i.e.* at constant displacement $\bar{\Delta}$) - which corresponds to the hatched area in Figure 2.9b except for an infinitesimal of higher order - is the potential energy variation associated to the increment da in a body with crack length equal to a . That said, it is possible to determine the *J*-value for the body with crack length equal to a in correspondence of *S*, by dividing this energetic term - labelled dU and indicating an energy released by the system - by the increase in crack area $dA = Bda$, resulting in the relationship

$$J = -\frac{1}{B} \frac{dU}{dA} \Big|_{\bar{\Delta}} \quad (2.26)$$

It is worth pointing out that the minus sign is due to the definition of dU , which is the difference in areas under the $P-\Delta$ curve between the $a + da$ and a crack length configurations, resulting in a negative value. The definition of J , as expressed by equation (2.26), prepares the path for the experimental determination of J -values associated to the concerned cracked body characterized by a specific geometry - *e.g.* a fracture test specimen. The determination of the J -integral value is based on the multi-specimen approach, according to which several tests on nominally identical specimens except for the increasing crack length a have to be carried out. From the load-displacement curves obtained by mechanical tests on the various specimens, it is possible to determine the J -value in every point of the loading curve, as long as the corresponding crack length is known. However, it has been proven that for some specific specimen geometries, the J -value can be determined using a single-specimen approach as well, starting from the load-displacement curve obtained from the mechanical test on a single specimen of given geometry. The requested parameters are the energy U absorbed by the system - which is evaluated as the area under the loading curve up to the concerned point - and the geometry of the specimen. In addition, the value of the dimensionless factor η is required, which may not be known *a-priori* in some configurations. In the cases where η is given, the J -integral value can be calculated as

$$J = \eta \frac{U}{B(W - a)} \quad (2.27)$$

where W is the width (uniform) of the specimen.

Alongside Compact Tension (CT), the most used test configuration, both for metals and polymers, is Single Edge notched in Bending SE(B), whose schematic representation is reported in Figure 2.10.

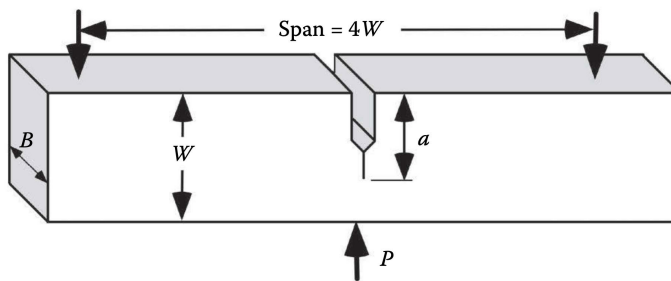


Figure 2.10: SE(B) fracture test specimen geometry, adapted from [Anderson, *Fracture Mechanics : Fundamentals and Applications*]

3 Architected ductile polymer cellular model structures produced by 3D printing

3.1 Additive manufacturing of ACMs

High reliability, geometrical complexity and manufacturing issues were the main issues for Architected Cellular Materials, ACMs, to be widely adopted in industrial application, confining them to academic research and prototyping. The scenario started to change when relevant and self-reinforcing progresses in Additive Manufacturing, AM, were reached. AM is commonly intended as a set of techniques where a layer-by-layer approach is adopted for the manufacturing of parts and products; it is usually characterized by small sizes, limited production volumes, and a complex, specifically tailored design. Just like ACMs, AM was initially limited to scientific research, as an innovative way to obtain prototypes with severe geometrical complexity, overcoming the problems of traditional manufacturing processes. Then, as different branches and techniques developed to deal with an increasing *spectrum* of materials - including metals, polymers, polymer composites and ceramics - and progresses were made in hardware and software design, AM became a widespread technology, now easily ac-

3. ARCHITECTED DUCTILE POLYMER CELLULAR MODEL STRUCTURES PRODUCED BY 3D PRINTING

cessible to anyone due to the dramatic decrease of costs. As processes became more and more sophisticated and high-quality, research towards porous materials and systems - which would greatly benefitted from their advances - received a great boost, to such extent that the newly-studied ACMs further stimulated the development of increasingly suitable and accurate AM techniques. Thus, a still-ongoing virtuous circle between research in materials field and progresses in additive manufacturing techniques was established.

However, plenty of steps still have be made before additive manufactured ACMs could reach the status of reliable systems with large-scale application in the most demanding industrial fields. While the advances in their design and fabrication were undeniable, the main concern about these lattice structures remains about their structural integrity, as they resulted particularly prone to fail due to damage accumulation and fatigue, both in quasi-static and dynamic conditions. More specifically, the porous nature of the systems, characterized by thin struts and junction points (nodes) that act as stress concentrators, leads to inherent structural weakness in comparison with *continuum*, at fixed material; further, the combination of high geometrical complexity, relatively poor AM process accuracy (if compared with well-established and hyper-refined traditional manufacturing techniques) and problems in dealing with the smallest details and perfect orientation of the struts, provides big challenges that are yet to be solved; further, as structural integrity is based on the concept of crack, ACMs are extremely sensitive to defects introduced by AM processes, which turn out to be preferential sites for damage accumulation, failure and crack initiation and propagation. In addition, as they are meant to be consistently used in load-bearing applications in the future, ACMs have to be characterized in a variety of loading conditions, in order for different stress conditions to be induced and their effect eventually evaluated.

While being initially conceived as a prototyping, quite limited technology to be used for almost academic purposes only, AM experienced an extremely rapid development in recent years. This led to the

proliferation of different techniques and their progressive refinement over time. However, the development of robust design principles, effective manufacturing guidelines, solid testing methodologies and validated international standards was not as fast. This is especially true as the scenario is being continuously modified by quick-fire innovations in AM processes.¹ Moreover, a further degree of variability is being provided by cutting-edge studies on innovative systems, such as Architected Cellular Materials, ACMs, characterized by a high porosity degree and a periodic and easy-tailorable structure. Thus, the development of well-established rulesets, in such ever-changing environment, is extremely challenging. Indeed, it is vital to tackle it in a systematic and strategic way, to bring some degree of order into chaos. To do so, research focused on topics of fundamental nature about additively manufactured ACMs, such as

- the study of their damage mechanisms in different stress conditions;
- the assessment of consensus on their structural integrity;
- the set-up of robust testing methodologies, to be used for both industrial and scientific purposes;

acquires an unprecedented importance.

The world of AM processes is traditionally divided into 7 categories: (a) material extrusion; (b) powder-bed fusion; (c) vat photopolymerization; (d) material jetting; (e) binder getting; (f) sheet lamination and (g) direct energy deposition. With regards to polymers, the most employed class of materials in AM, due to their versatility, low processing temperatures and wide range of properties achievable, the first three processes control the vast majority of the

¹S C Daminabo et al., “Fused deposition modeling-based additive manufacturing (3D printing): techniques for polymer material systems,” *Materials Today Chemistry* 16 (2020): 100248, ISSN: 2468-5194, <https://doi.org/10.1016/j.mtchem.2020.100248>, <https://doi.org/10.1016/j.mtchem.2020.100248>.

3. ARCHITECTED DUCTILE POLYMER CELLULAR MODEL STRUCTURES PRODUCED BY 3D PRINTING

market size.² Among these, material extrusion is undisputedly the most extensively employed, as it 1) does not require chemical post-processing (e.g. resin curing); 2) uses low-price machines and materials, 3) has low cycle times; 4) is extremely user-friendly, in terms of both skills needed and affordability. Even though some downsides have to be properly evaluated in process selection phase - low resolution in all directions depending on nozzle dimensions and anisotropy of the final parts - these benefits are so crucial not to prevent material extrusion from being the leader of AM processes in polymers field. Among the material extrusion processes, Fused Deposition Modeling (FDM) has become popular due to the low cost and large range of usable materials.³ In FDM of polymeric materials, a filament is heated and then deposited layer-by-layer from a nozzle on a platform according to the part model, which is sliced into several 2D layers to obtain the tool path motion of the nozzle. It was initially dedicated to prototypes, but thanks to recent technological advancements, nowadays it is used to print parts for industrial applications in a lot of sectors. In the aerospace and automobile industry, FDM manufactured parts are used to replace traditional metal components and reduce their weight maintaining appropriate robustness, this also reduces the turnaround time for part repair. Electronic applications take advantage of the development of polymer composites with tailored electrical properties to manufacture FDM parts for dielectric, conductive, sensors and energy storage applications. In biomedical applications,⁴ one of the greatest

²Carmen M González-Henríquez, Mauricio A Sarabia-Vallejos, and Juan Rodríguez-Hernández, "Progress in Polymer Science Polymers for additive manufacturing and 4D-printing : Materials , methodologies , and biomedical applications," *Progress in Polymer Science* 94 (2019): 57–116, ISSN: 0079-6700, <https://doi.org/10.1016/j.progpolymsci.2019.03.001>, <https://doi.org/10.1016/j.progpolymsci.2019.03.001>.

³Pavan Kumar Penumakala, Jose Santo, and Alen Thomas, "A critical review on the fused deposition modeling of thermoplastic polymer composites," *Composites Part B: Engineering* 201, no. August (2020): 108336, ISSN: 13598368, <https://doi.org/10.1016/j.compositesb.2020.108336>.

⁴Mohd. Javaid and Abid Haleem, "Additive manufacturing applications in medi-

advantages of AM is the straightforward process chain from diagnosis to surgery, using the same imaging and scanning results, necessary for the diagnosis, to create the digital design of the physical model. In this way, reverse engineering allows the manufacturing of highly customizable products. In tissue engineering, FDM allows the fabrication of complex internal architecture in scaffolds with controlled porosity and interconnected network. It is suitable for the manufacturing of polymer cellular structures, ensuring the possibility to obtain high shape complexity and size flexibility, while guaranteeing structural regularity and repeatability thanks to the controlled filament deposition and thermo-mechanical history imposed.

ABS resin is the most employed polymeric material in FDM, as well as Poly-Lactic-Acid, PLA. This is due to its versatility in synthesis stage, easy processability as a result of a wide window of work temperatures and possibility to be used in a variety of different fields and applications. Thus, well-established practical guidelines to be used for printing are widely available, in addition to the consolidated literature about the bulk material itself, which proved to be a textbook example of ductile response. So, ABS was regarded as the perfect candidate to be used as feeding material for the manufacturing of ACMs in ductile polymer. As process and material properties in the melt state - e.g. extrusion rate and viscosity - are reported to sensibly affect the quality of the extruded filament, special attention in the design phase was then dedicated.

3.2 Experimental

Material and fabrication of the structures

A commercial filament of ABS was selected as feeding material for the Original Prusa i3 MK3S+ FDM printer used for the manufacturing of the model structures. The appropriate process conditions and

cal cases: A literature based review," *Alexandria Journal of Medicine* 54, no. 4 (2018): 411-422, ISSN: 2090-5068, <https://doi.org/10.1016/j.ajme.2017.09.003>.

3. ARCHITECTED DUCTILE POLYMER CELLULAR MODEL STRUCTURES PRODUCED BY 3D PRINTING

systems' architecture were carefully selected in the preliminary design phase. The nozzle and plate temperatures were set at 220°C and 80°C, respectively. The material was extruded at 400 mm/min, corresponding to an apparent shear rate at the nozzle die (whose nominal diameter is 0.4 mm)⁵ of 133 s⁻¹. Such value, selected to be comparable with those typically used in standard die forming process, suggests the presence of a given (non-null) degree of macromolecular pre-orientation in extruded filament material. Differential Scanning Calorimetry (TA Instruments calorimeter, model Q100, with a scanning heating rate of 10°C/min, under a nitrogen atmosphere) analyses were performed on the samples collected from the 3D-printed structures. The glass transition temperature of the extruded filament material resulted of 104°C. The same process parameters were applied for the manufacturing of portions of filament used for the determination of the density of the extruded material. More specifically, by combining the outcomes of independent mass and volume measurements, the material density resulted of 1.06 ± 0.02 g/cm³. Mass was measured with a digital analytical balance with 10⁻¹ mg resolution, while volume was calculated from length measurements. The sample diameter was measured by means of 1 µm resolution micrometer, while optical microscope 90 Leica MS5 equipped a travelling xy-table moved by 1 µm-graduated micrometers, was used for the sample length.

The 3D-printed specimens examined in the fundamental mechanical characterization under compression were cubes and prisms with square- base, manufactured with a 30% "infill density". Taking as reference the completely solid systems, which would correspond to 100% "infill density", the specimens are nominally 70% hollow. Such nominal value makes the structures locate at the lower bound of the range for cellular materials definition (≥ 70%). The specimen base was on the X-Y plane, and the height along the Z direction (Figure 3.1). The deposition of a layer - line by line, in the X-Y plane (in-

⁵Christopher W Macosko, *Rheology Principles, Measurements and Applications* (Wiley-VCH, 1994), ISBN: 1560815795.

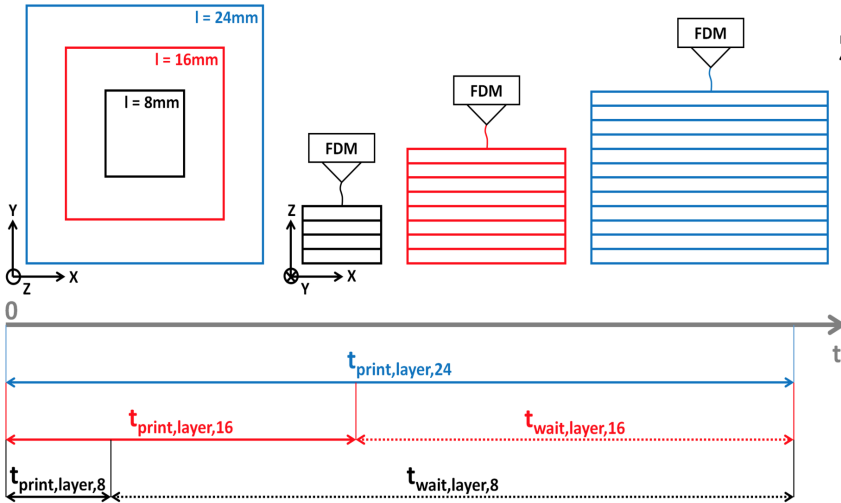


Figure 3.1: Visual representation of specimen manufacturing process. Printing and wait times were reported according to equation (3.1).

plane deposition) - was followed by the 0.4 mm upward shift of the nozzle (along the Z direction, from now on called layer stacking direction) and by the deposition of the subsequent layer (Figure 3.1). A ordered 4-layer sequence was designed to be the basic unit of the systems, with filament orientation of 0° , 45° , 90° and -45° , in the first, second, third and fourth layer, respectively (Figure 3.2). Such basic unit was then repeated along layer stacking direction (Z) to obtain the specimen prefixed height, composed of n layers (Figure 3.1), where n is a multiple of 4.

In order to study the effect of the specimen size on the mechanical response under compression, two shapes were selected: (i) cubes with varying side length values (8,16,24 mm); (ii) square-base prisms with 16 mm base side length and varying height (8 and 24 mm). The complete recap of the model structures for the basic mechanical characterization, as well as the convention adopted for their labelling, is presented in Table 3.1. In a continuous printing process with fixed

3. ARCHITECTED DUCTILE POLYMER CELLULAR MODEL STRUCTURES PRODUCED BY 3D PRINTING

material deposition rate, the time necessary to complete the deposition of a single layer varies according to the layer surface area of the specimen: the smaller this area, the lower the time. In the case of the cube-shaped specimens here examined (C_8 , C_{16} and C_{24}), a continuous deposition of material would therefore result in different cooling and solidification histories undergone by the polymeric material when varying the base length. The problem of eventual thermal history differences was seriously taken into consideration during the preliminary design phase, resulting in the following solution. The time necessary for the complete manufacturing of a C_{24} layer ($t_{\text{print,layer},24} = 58$ s) was taken as the reference, and for C_8 and C_{16} specimens an appropriate waiting time ($t_{\text{wait,layer},8(16)}$) - when no deposition took place - was introduced at the end of each layer printing phase (Figure 3.1) so that:

$$t_{\text{print,layer},8} + t_{\text{wait,layer},8} = t_{\text{print,layer},16} + t_{\text{wait,layer},16} = t_{\text{print,layer},24} \quad (3.1)$$

The mechanical response of the model structures was then studied in the framework of the Fracture Mechanics (FM). Rectangular-base prism ($B \times W \times L = 8 \times 16 \times 80$ mm³, referring to thickness, width and length, respectively) was selected as a suitable geometry for fracture test specimens. The ordered 4-layer basic unit repetition was achieved by filament deposition on the thickness-length plane and 3D growth along the width direction. Specimens with nominal 30% infill were manufactured. In addition, different porosity levels were explored, with the aim to study the underlying failure mechanisms of such peculiar cellular materials (which, by definition,⁶ are only the 30% infill, as they present nominal 70% porosity). Thus, different nominal infill values were selected, spanning from the 30% to the very highest 100%. Intermediate configurations (47%, 65% and 82%) were explored as well. Increasing input infill values resulted in decreasing space between adjacent windings of filament within a single layer of the structures.

⁶Gibson and Ashby, *Cellular solids: Structure and properties, second edition*.

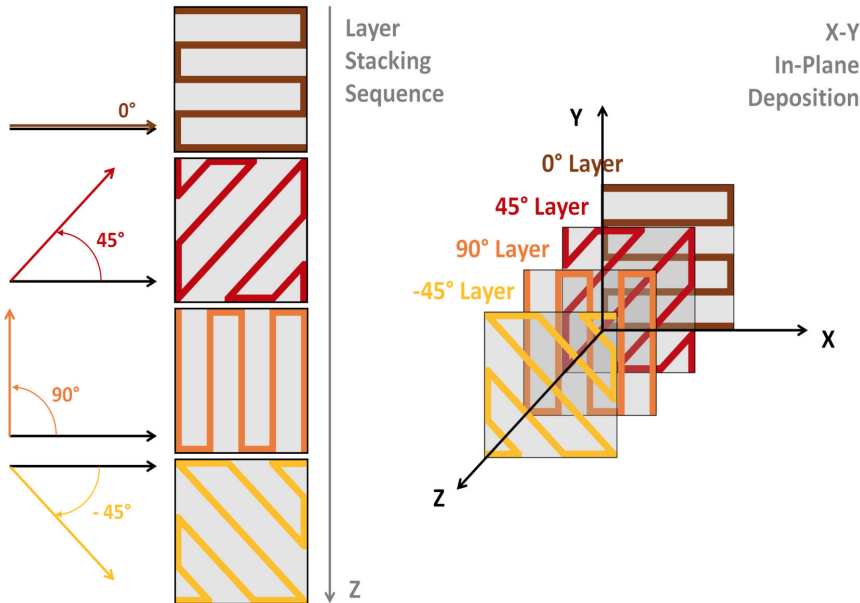


Figure 3.2: Infographic of the main 4 layers and their sequence in layer stacking direction to form the repeating basic unit for the 3D structures.

Well aware of the critical importance of the crack in FM testing, as well as of the inherent degree of complexity of the systems due to their porous nature, two different notching techniques were preliminary explored. The first one (Series A) was performed directly at the FDM printer, by imposing a specific *intra*-layer filament deposition pattern which resulted in a notch-like discontinuity; the second one (Series B) was based on the introduction of a sharp tip notch on one edge of the rectangular-base prisms, by means of a notching machine CEASt Notchvis. Both ways led to the obtainment of Single Edge notched in Bending, SE(B), specimens. Two fundamental requirements had to be met: 1) the notch had to be as sharp as possible, in order to replicate a natural crack in a component; 2) no damage ahead of the crack tip had to be induced as a result of notch introduction. Thus, in the case of series B, the setup configura-

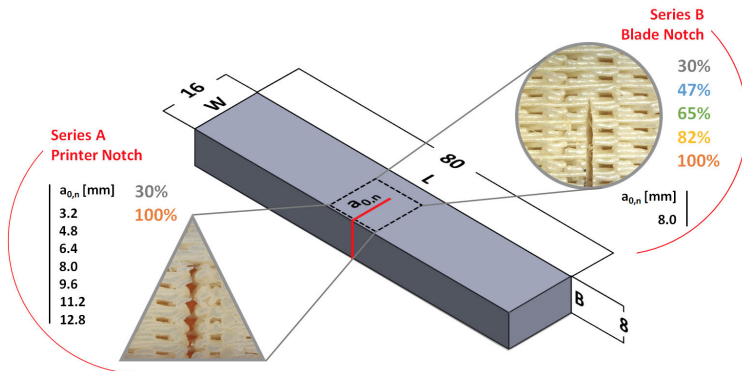
3. ARCHITECTED DUCTILE POLYMER CELLULAR MODEL STRUCTURES PRODUCED BY 3D PRINTING

tion was carefully developed to guarantee the obtainment of suitable specimens. More specifically, the notching machine (characterized by automatic vertical cutting movement and manual specimen advancement controlled via micrometers) was equipped with two sacrificial PA6 bars, positioned in such a way to sandwich the cellular "model" structures. This resulted in enhanced stability of the cutting process, leading to higher final quality and reproducibility of the specimens. The blade advancement during the cutting process was performed along the width (and thus the layer stacking) direction, which would have eventually been coincident with the loading direction used in the 3-point bending fracture tests. Conversely, with regards to series A, different values of nominal crack length were explored, for specimens with nominal infill level of 30% and 100% only. This was realized by imposing incomplete filament deposition in the layers up to the desired notch length, while the uncracked region was obtained in the classical way. Thus, as $a_0/W = 0.2, 0.3 \dots 0.8$ were selected, The crosshead speed had to be adapted when varying the initial crack length, in order to maintain the apparent strain rate as constant. Representative images of the series A and B notch are represented in Figure 3.3a.

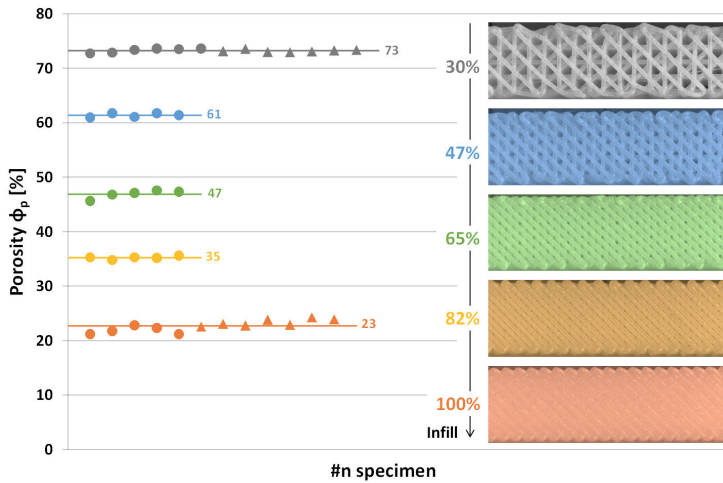
After evaluating the effect of the two different notching techniques on the fracture response, the notching machine was then selected as preferential method for crack introduction throughout the whole following experimentals. For each infill level, from 30% to 100%, sharp-notched and blunt-notched specimens were obtained. Nominal crack length (a_0) values of 8 mm were achieved, leading to nominal a_0/W values close to 0.5, so that one of the fundamental geometrical requirements of FM ($0.45 \leq a_0/W \leq 0.55$) could have been satisfied.⁷

As stresses in orthogonal direction would have resulted from loading in SE(B) configuration (Mode-I crack opening), special attention was paid to the study of the tensile response of the model structures, when tested orthogonally to the layer stacking direction. The design phase of suitable specimens for that task was challenging, since good

⁷Anderson, *Fracture Mechanics : Fundamentals and Applications*.



(a)



(b)

Figure 3.3: Fracture test specimens, characterized by varying infill levels (30%, 47%, 65%, 82%, 100%): (a) Geometry of the specimens: rectangular-based prisms with dimensions $B \times W \times L = 8 \times 16 \times 80 \text{ mm}^3$ and initial crack length $a_{0,n}$. The Series A - Printer Notch, and B - Blade Notch (see text), 30% infill structures are indicated with \triangle and \circ frames; (b) Overview of the pool of specimens tested. For each infill level, characterized by a specific chromatic convention, the porosity values, calculated using the actual filament density, are reported (\bullet and \blacktriangle). In addition, the series mean values are indicated (lines and adjacent numbers). The images of the structures at varying infill, taken at the optical microscope, are represented.

3. ARCHITECTED DUCTILE POLYMER CELLULAR MODEL STRUCTURES PRODUCED BY 3D PRINTING

grasping and load transfer between testing machine and specimen would have been required. A specific design strategy was adopted, based on a variable infill approach. More in detail, the specimens - rectangular-base bars ($B \times W \times L = 4 \times 8 \times 120 \text{ mm}^3$, referring to thickness, width and length, respectively) - were produced in such a way to present two distinct regions: 1) the central region, corresponding to the gauge length in standard tensile tests ($l_{o,p} = 60 \text{ mm}$), where the desired value of infill was applied; 2) the end zones, where grasping took place, where the maximum nominal infill level (100%) was imposed. In the case of 100% infill specimens, the same infill level was maintained, resulting in no differences between central and end regions. All the infill values used in for the production of fracture test specimens were explored in tensile testing.

It is important to point out that compression and tensile/fracture test specimens belong to different batches, as they were produced several months apart. As the FDM printer used for compression specimens had to be replaced in the meantime, the outcomes obtained in tensile and fracture tests can not be related to the ones coming from the first (compression) batch. Indeed, the stiffness results obtained from fracture tests could and will be related only to the corresponding values in tensile conditions. Further, mechanical testing of the extruded filament (whose results will be presented in the following) coming from both batches led to equivalent outcomes, meaning that no differences were induced within the constituent material by changing the FDM printer.

Characterization

Morphological analyses and density measurements

Morphological characterization of the specimens was carried out, at the macro-scale, by means of standard optical and digital microscopy techniques (Leica microscopes, models MS5 and DMS300). These analyses allowed also the assessment of the quality of the samples. Additional morphological analyses were performed on the C_{16} struc-

tures after deformation under compression at large strain levels (the compression tests on the 3D-structures are described below). Three nominal apparent strains, namely 20%, 40% and 60%, were analyzed on three different specimens. For each specimen, the load was rapidly removed once the pre-set level of deformation was reached, and the deformed specimen was then kept at room temperature for at least one week in order to allow most of the free strain recovery. A sharp pre-notch was then introduced at a given position into each of the three deformed specimens and into one undeformed specimen. Each specimen was then brought to complete fracture after a prolonged exposure to liquid nitrogen, in such a way that any plastic deformation associated with the fracture process that started from the tip of the pre-notch could be hindered. The cryogenic-fracture surfaces (parallel to the X-Z plane) of the various specimens were then observed at the microscopes.

For each compression and fracture test specimen, the apparent density, $\rho_{\text{app},3\text{D}}$, was determined as the ratio between the specimen mass and its volume. Mass measurements were carried out by means of a digital analytical balance with 10^{-1} mg resolution. The volume was determined from the specimen dimensions, measured using either a digital micrometer (with 1 μm resolution) or a Vernier caliper (with 50 μm resolution), for lengths lower or higher than 20 mm, respectively. In the case of tensile tests, the procedure adopted was slightly different. All specimens' dimensions were measured, as the corresponding values would have been later used for the normalization from load - displacement to stress - strain data. Conversely, only one specimen per infill level was selected to be measured in terms of mass. After testing, these representative specimens were divided into central and end zones by means of the same cutting blade used on the notching machine. The mass of the central region was measured as the difference between the mass values of the entire specimen and of the end zones; the volume, instead, was calculated using nominal gauge length value $l_{0,p} = 60$ mm, as well as the thickness and width measures previously performed. This procedure was used for

3. ARCHITECTED DUCTILE POLYMER CELLULAR MODEL STRUCTURES PRODUCED BY 3D PRINTING

the infill levels up to 82%, while in the case of 100% mass and volume measurements were performed on the entire specimen, as no infill variations were designed between central and end regions. The density of each tensile test specimen measured is considered representative of the corresponding infill level. An "apparent" character is attributed to the density of the specimens in consideration of the porous nature of the material. While in tensile tests the aim was to obtain an indication of the apparent density of the systems while varying infill level, in the case of fracture tests, more quantitative informations were researched. More specifically, the porosity of the structures (determined from apparent density by normalizing for ρ_{ABS}) in series A and B were compared, in order to ensure the compatibility of the outcomes, in terms of specimen preparation. The results are showed in Figure 3.3b. It clearly emerges that no relevant differences exist between series A and B specimens, which allows to state that the two different methods used for notch introduction led to the same porosity levels. Further, by comparing the mean porosity values calculated over the entire A and B population with the corresponding nominal porosity (complement to 100 of the infill level), differences increase with denser systems. The actual porosity levels span from $\approx 75\%$ (corresponding to the nominal 30% infill) to $\approx 20\%$, which refers to nominal 100% infill (3.3b). In the light of this outcome, a confirmation of the 30% infill structures being the only ones that could be considered as full-fledged cellular materials - as their definition requires porosity $\geq 70\%$ - was obtained. Indeed, the other systems are to be considered as solids containing isolated pores,⁸ with variable degree of hollow regions, used for deepening the knowledge about failure mechanisms of cellular materials. Interestingly, in 100% infill specimens, the actual mean porosity is 23%, rather than the nominal 0% expected. This implies that even the most *continuum*-like systems, with such FDM machine and filament parameters, presents relevant void percentage, that can and should not be overlooked.

The presence of significant degrees of porosity even in the max-

⁸Gibson and Ashby, *Cellular solids: Structure and properties, second edition*.

imum infill configuration stimulated more in-depth morphological analyses to be performed, aimed at evaluating the actual structure of the systems. To do so, an additional representative specimen for each infill level - not used for testing purposes, yet still considered in the porosity evaluation process, as represented in Figure 3.3b - was selected and its layers carefully hand-separated, one by one, by means of a sharp cutter. This step was rigorously performed in order not to modify the actual layer geometrical features, so that they would have been as similar as possible, after full separation. Once four layers with different orientations, characteristic of the basic unit, were separated for each infill level and images were taken at the optical microscope, the key geometrical parameters were determined *via* image processing software ImageJ. The geometrical features selected as representative were the diameter of the filament (d) and the separation (D) and the fillet radii (R) between adjacent windings. The values obtained were used to build up 3D CAD models of the fracture specimens, which were of fundamental importance for a bunch of reasons: 1) they were representations of the actual systems, as obtained from the FDM machine, so to take into account and to point out eventual deposition defects, in comparison with the STL model used during the printing process; 2) in the case of maximum infill specimens, the model allowed to prove the presence of residual porosity, as a result of void regions produced by juxtaposition of beam-like elements with circular cross section; 3) once the position of the notch was selected, the proper sections of the models provided reliable information about the structure in the notch plane (F - F), the crack front as a function of initial crack length and thus the resistant section generated. The key information about the method, applied to the cellular solid case (30% infill), were represented in Figure 3.4.

Mechanical tests

Tensile tests on the extruded filament Uniaxial tensile tests were carried out on portions of the filament produced with the same pro-

3. ARCHITECTED DUCTILE POLYMER CELLULAR MODEL STRUCTURES PRODUCED BY 3D PRINTING

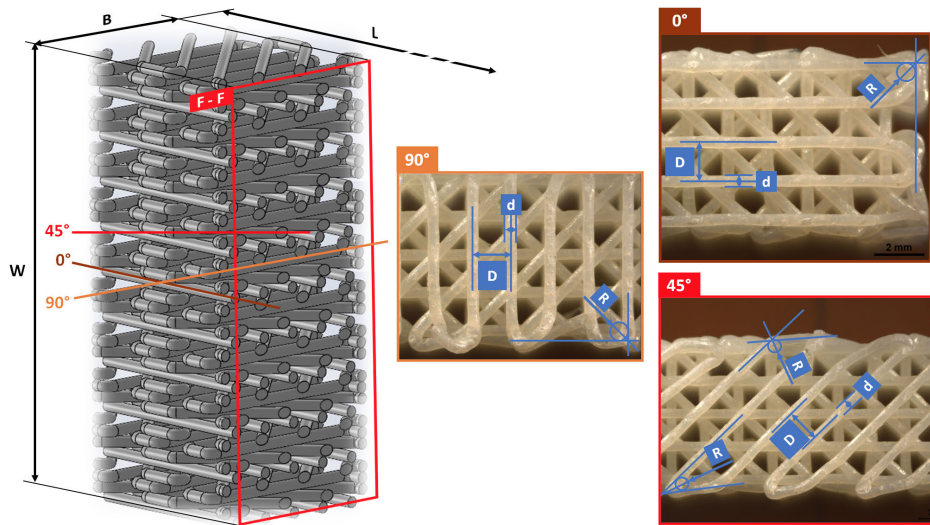


Figure 3.4: Determination of key geometrical parameters in $0^\circ, 90^\circ, \pm 45^\circ$ layers for representative 30% infill configuration. The diameter of the filament (d) and the spacing (D) and fillet radii (R) between adjacent windings, used to build up the 3D CAD model of the structure, are indicated. The model is cut along its length, L , by section plane $F - F$, to provide information about the structure in correspondence of notch position. Notches are introduced always in the same position and crack front locates always within the same filament, regardless of the infill level considered.

cess conditions used for the manufacturing of the 3D-structures. An Instron test system (model 3366) equipped with a 500 N load cell was used, and the tests were performed at room temperature. The testing configuration is showed in Figure 3.5. A graph paper mask was used in order to make the specimen handling and correct positioning phases easier. The distance between the grips, l_0 , was fixed at 70 mm, and the crosshead speed was set at 3.5 mm/min in such a way to obtain a nominal strain rate equal to that used in the compression tests on the 3D-structures (see below, in this Section). Five different samples were tested. For each sample, the load vs crosshead displacement curve was recorded, and then converted into a nominal tensile

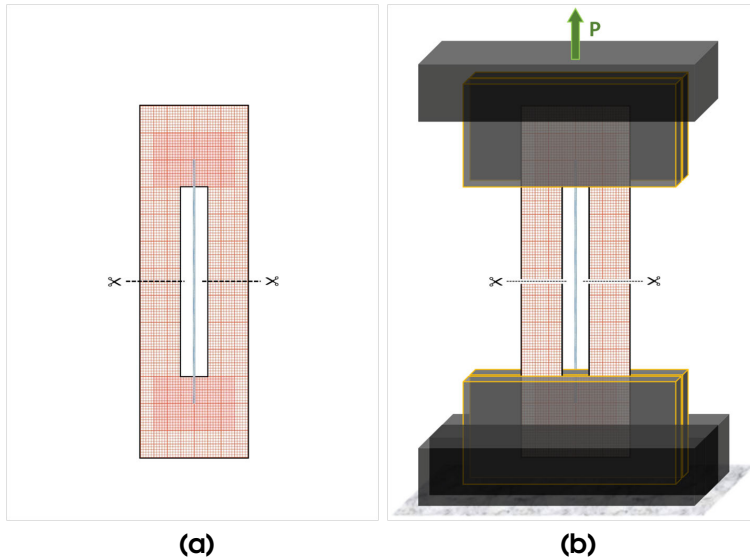


Figure 3.5: Tensile test procedure on the extruded filament of ABS. (a) Preparation of the graph paper mask for handling and positioning phases; (b) execution of the test.

stress vs nominal tensile strain curve. The stress was determined as the load over the initial sample cross section (the filament diameter was measured as described at Section 3.2); the strain was calculated from the crosshead displacement, divided by l_0 .

Compression tests on the 3D-structures Compression tests were performed by using the Instron test system 3366 equipped with a 10 kN load cell, at room temperature. Both monotonic (one-way) and cyclic compression tests were carried out. In the monotonic tests, the crosshead speed was varied depending on the height of the specimen under analysis, in order to obtain the same apparent compression strain rate, which was 0.05 min^{-1} . A thin layer of paraffin oil was deposited on each compression plate in order to reduce the friction between the specimen and the plate. The testing configuration is

3. ARCHITECTED DUCTILE POLYMER CELLULAR MODEL STRUCTURES PRODUCED BY 3D PRINTING



Figure 3.6: Compression tests on 3D-printed cellular structures.

showed in Figure 3.6. The experiments were meant to explore the following effects (see Table 3.1):

- loading direction effect, from tests on C_{16} specimens carried out with the loading direction either parallel or orthogonal to the 3D-growth (Z) direction;
- size effect, from tests on C_8 , C_{16} and C_{24} specimens loaded along the Z direction;
- height effect, from tests on P_8 , C_{16} and P_{24} specimens loaded along the Z direction.

For each specimen geometry and loading direction examined, four specimens were tested. For each specimen tested, the load, P , vs

crosshead displacement, u_r , curve, output of the test, was converted into the apparent stress, σ_{app} , vs apparent strain, ϵ_{app} , curve. σ_{app} was calculated as P over the initial cross section of the specimen, ϵ_{app} as the crosshead displacement, u_{cor} - properly corrected to remove the "foot zone" of the P vs u_r curve corresponding to the approaching and plate-specimen contact establishment phases - divided by the initial height of the specimen. The dimensions of the specimens were measured as described at Section 3.2. The compression stress and strain here determined were considered as "apparent" because of the cellular nature of the systems examined. Tests were interrupted at an ϵ_{app} level higher than 50%, with the only exception of the experiments on the C_{24} specimens that were interrupted at smaller strains, when the load reached the full-scale of the load cell.

The cyclic compression tests were carried out on the cube-shaped specimens with different side lengths (C_8 , C_{16} , C_{24}) - one single specimen for each size. Each cycle consisted of a loading phase, characterized by the same apparent compression strain rate used in the monotonic tests, followed by an unloading phase at a doubled speed. The crosshead displacement, u_r , reached at the end of the loading phase increased from cycle to cycle according to the scheme presented in Figure 3.7a. Load, P , vs u_r curves were collected as output, and then properly corrected for the "foot zone", as mentioned above, in order to obtain the P vs u_{cor} curve (Figure 3.7b). The tests were interrupted at $\epsilon_{app} \approx 25\%$. For each cycle, the maximum apparent deformation applied, $\epsilon_{app,max,appl}$, and the residual apparent deformation after the unloading phase, $\epsilon_{app,res}$, which are regarded as the fundamental quantities for this kind of analysis, were determined. In particular, $\epsilon_{app,res}$ was taken in correspondence of the last point of monotonic decrease on the unloading curve below the threshold value of 0.5 N.

Fracture tests on the 3D-structures Fracture tests were performed by using the same Instron test system 3366 equipped with a 10 kN load cell, at room temperature. The experimental configura-

3. ARCHITECTED DUCTILE POLYMER CELLULAR MODEL STRUCTURES PRODUCED BY 3D PRINTING

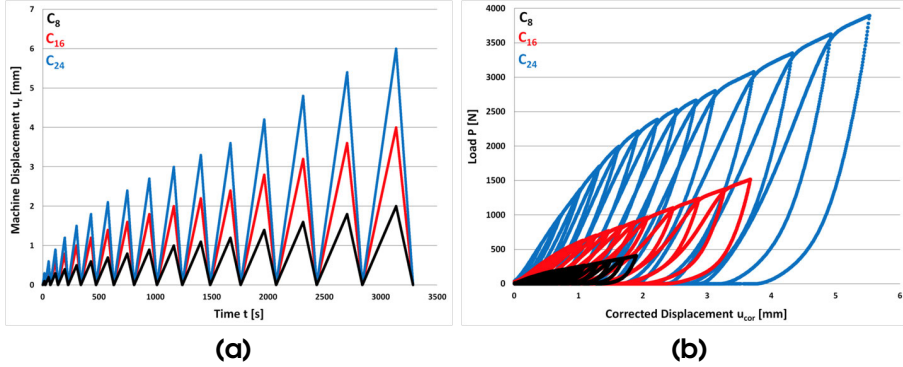


Figure 3.7: Cyclic compression tests on cube-shaped C_8, C_{16}, C_{24} specimens. (a) Test input as Machine Displacement, u_r , vs Time, t , plot; (b) output curves expressed in terms of Load, P , vs Corrected Displacement, u_{cor} (see text).

tion adopted was 3-point bending, characterized by two lower rolls (whose distance, called span, S , is a fundamental parameter for Fracture Mechanics) on which the specimen was positioned, and by an upper central roll (in correspondence of the notch), through which the load was transferred to the specimen. The tests were performed by selecting a value of span $S = 4W = 64$ mm, where W is the nominal width of the specimens, so that the classical FM closed solution could be successfully used.⁹ The experimental configuration of 3-point bending on SE(B) specimens is represented in Figure 3.8a. The tests were performed in quasi-static conditions, in displacement control. Considering the specimens with $a_0/W = 0.5$, a crosshead speed equal to 1 mm/min was set, a value which is typically used in fracture tests on polymeric materials. Thus, an apparent tensile strain rate of 0.0117 min^{-1} , which is comparable to the one applied in compression tests (0.05 min^{-1}), was imposed. This strain rate level was maintained constant for all the fracture tests, resulting in differ-

⁹Moore, Williams, and Pavan, *Fracture mechanics testing methods for polymers, adhesives and composites*.

ent crosshead speed needed in the case of varying initial crack length values, during the study of the notching technique effect. During this preliminary activity, six 30% infill specimens (each one with different a_0/W) for each technique (Series A: 3D-printed notch; Series B: blade-machined notch) were tested. Conversely, the main fracture testing activity (where initial cracks were only machine-notched) involved three sharp-tipped specimens for each infill level. It is important to point out that notches were introduced in the same position in each specimen, and that the resulting crack fronts were located in correspondence of the same layer, in order for the structure to be always equivalent (except for the varying infill level). Load vs displacement raw curves were taken as output of the tests.

Fracture tests on *continuum* SE(B) specimens in ductile polymer are extremely prone to be affected by indentation, pin penetration and machine compliance contribution⁹. Thus, load vs displacement raw curves had to be properly corrected to obtain suitable results. Specific compliance correction techniques had been developed⁹ requiring, in the case of SE(B) specimens, the execution of tests in a span $S = 0$ configuration, to point out just the undesired side effects (Figure 3.8b). The porous nature of the cellular systems, however, required special attention in dealing with compliance correction tests, with respect to the case of *continuum*. The structure of the specimens in correspondence of the top and bottom contact points with the rolls during fracture tests was evaluated by means of optical microscopy analyses. After fracture testing, the same filament patterns were rigorously researched in the side regions of the specimens, far from the notch area and thus not affected by test-induced damage (Figure 3.8c). This activity was carried out for the infill levels of 30%, 47% and 65%, while 82% and 100% were excluded due to the low porosity of the systems, which led to i) high difficulties in the correct individuation of the correct repeating patterns; ii) less pronation to structure-sensitivity of the compliance correction tests. Thus, compliance correction tests were performed for 82% and 100% infill levels regardless of the local structure.

3. ARCHITECTED DUCTILE POLYMER CELLULAR MODEL STRUCTURES PRODUCED BY 3D PRINTING

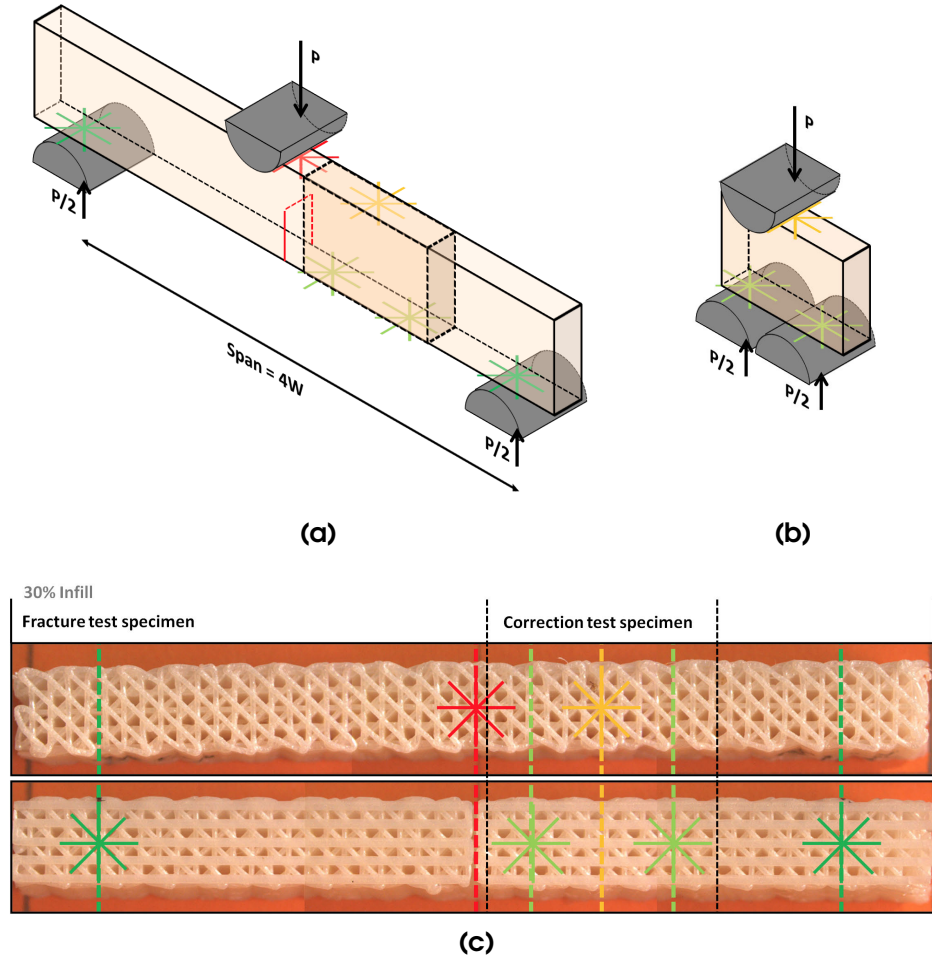


Figure 3.8: Fracture tests on SE(B) specimens, characterized by varying infill levels (30%, 47%, 65%, 82%, 100%): (a) 3-point bending configuration used in fracture tests; (b) compliance correction test experimental setup; (c) top and bottom (BxW) images of a 30% infill representative specimen used for the structure research phase. Red and green asterisks refer to the specific filament pattern in correspondence of the top and bottom points where load was applied, respectively. The same structures, researched in different positions within the specimen, in order to obtain proper correction test specimen, are represented in yellow and light-green.

Tensile tests on the 3D-structures Tensile tests were performed by using the same Instron test system 3366 equipped with a 10 kN load cell, at room temperature. The distance between the grasping elements was set to be equal to the gauge length $l_{o,p} = 60$ mm. The crosshead speed was set to 0.7 mm/min, in order to obtain the same apparent strain rate maintained in fracture tests, which was 0.0117 min^{-1} . The grasping process introduced compression stresses in the specimens before the start of the tests. With the aim to study the tensile response of the systems, only the data points with non-negative load values were considered. To do so, the displacement level corresponding to the zero-load condition was determined and then used as shift value of the loading curves on the displacement axis. Load and displacement data were normalized over the specimen dimensions, obtaining the apparent stress vs apparent strain curves. The apparent elastic modulus, $E_{app,t}$, was then determined as the slope of the stress vs strain curves in the initial linear elastic region.

3.3 Results and discussion

Morphology and density of the structures

The two-dimensional development of the 3D-structure can be easily detected by looking at the manufactured 3D-specimens along an axis parallel to the 3D-printing growing direction (Z direction). Figure 3.9a shows the X-Y top surface view of compression test specimens C_{24} , C_{16} and C_8 . The 3D-structures appear characterized, on the X-Y plane, by a repetition of figures. Each figure, whose characteristic size is in the order of 1 mm, is generated from the complex overlapping, along the Z direction, of the layers with different orientation. This defines space frames (cells) with different shapes and dimensions. Figures and cells can be seen also from the sectional view of the structure that is reported in Figure 3.9b, obtained from a CAD model from the relief of the C_8 specimen. The cells are fully interconnected,

3. ARCHITECTED DUCTILE POLYMER CELLULAR MODEL STRUCTURES PRODUCED BY 3D PRINTING

and they even give rise to corridors along the entire height of the specimen.

The structure of the 8mm-side specimen (C_8) can be regarded as the fundamental building block to perform a morphological analysis of the specimens with different sizes. As shown in Figure 3.9a, the C_8 structure can be found right in the centre of the C_{16} structure, which in turn can be found right in the centre of the C_{24} structure. Further, C_{24} shows C_8 structures at its corners, embedded in incomplete C_{16} structures. These latter (i) overlap partially the central C_{16} structure in co-shared regions, and (ii) are mutually joined by connecting zones. These observations suggest that these lattice structures could be regarded, at the macro-scale, as a form of cellular solids characterized by a regular repetition of a basic pattern - C_8 and its supersets - formed by cells with different shapes and sizes. The degree of structural heterogeneity, ensured by such design strategy, effectively turned out to be higher than that commonly observed in the literature on FDM structures.^{10, 11, 12, 13}

The key parameter that characterizes the structures is their apparent density, $\rho_{app,3D}$. From classical literature on cellular solids,¹⁴

¹⁰I Maskery et al., “Insights into the mechanical properties of several triply periodic minimal surface lattice structures made by polymer additive manufacturing,” *Polymer* 152 (2018): 62–71, ISSN: 0032-3861, <https://doi.org/10.1016/j.polymer.2017.11.049>.

¹¹Aliaa M Abou-ali and Oraib Al-ketan, “Mechanical Response of 3D Printed Bending-Dominated Ligament-Based Triply Periodic Cellular Polymeric Solids,” *Journal of Materials Engineering and Performance* 28, no. 4 (2019): 2316–2326, ISSN: 1544-1024, <https://doi.org/10.1007/s11665-019-03982-8>.

¹²Chen Ling et al., “Mechanical behaviour of additively-manufactured polymeric octet-truss lattice structures under quasi-static and dynamic compressive loading,” *Materials & Design* 162 (2019): 106–118, ISSN: 0264-1275, <https://doi.org/10.1016/j.matdes.2018.11.035>.

¹³Ogulcan Eren, Hüseyin Kürsüd Sezer, and Necati Yalcin, “Effect of lattice design on mechanical response of PolyJet additively manufactured cellular structures,” *Journal of Manufacturing Processes* 75, no. January (2022): 1175–1188, <https://doi.org/10.1016/j.jmapro.2022.01.063>.

¹⁴Gibson and Ashby, *Cellular solids: Structure and properties, second edition*.

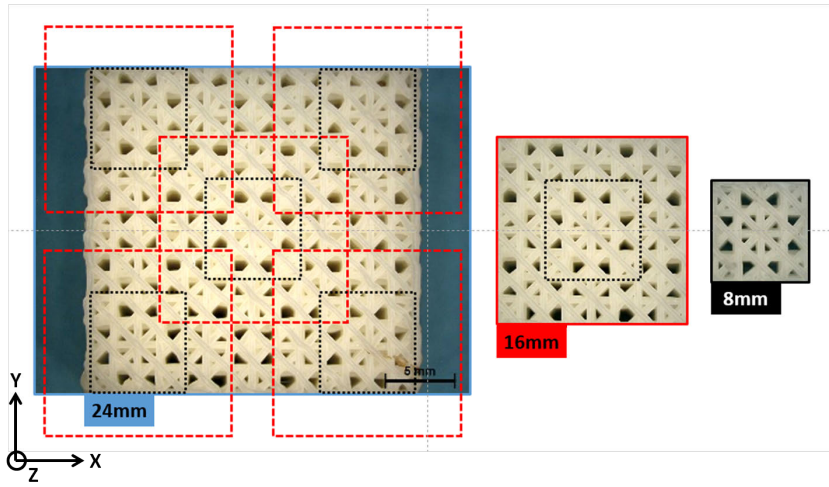
the most widely employed specimen-related parameter is the relative density, $\rho_{\text{rel},3\text{D}}$, which is the ratio between $\rho_{\text{app},3\text{D}}$ and the material density, which in the case of the structures here examined is the density of the filament extruded from the 3D-printer, ρ_{ABS} . As expected by considering that the various specimens were ideally identical from the structural point of view, the differences recorded among their $\rho_{\text{rel},3\text{D}}$ values were very small. A 3.2% standard deviation was obtained with a $\rho_{\text{rel},3\text{D}}$ mean value of 0.35. It is worth recalling that, according to Gibson and Ashby¹⁴, such a value of $\rho_{\text{rel},3\text{D}}$ is typical of structures that are on the border between "true cellular solids" (with relative density smaller than 0.3) and "solids containing isolated pores". In order to rely on a more homogeneous base of data, the specimens with a value of $\rho_{\text{rel},3\text{D}}$ outside 0.35 ± 0.02 were not considered in the analysis. This is the case of only two specimens belonging to the C₈ series.

Mechanical behaviour

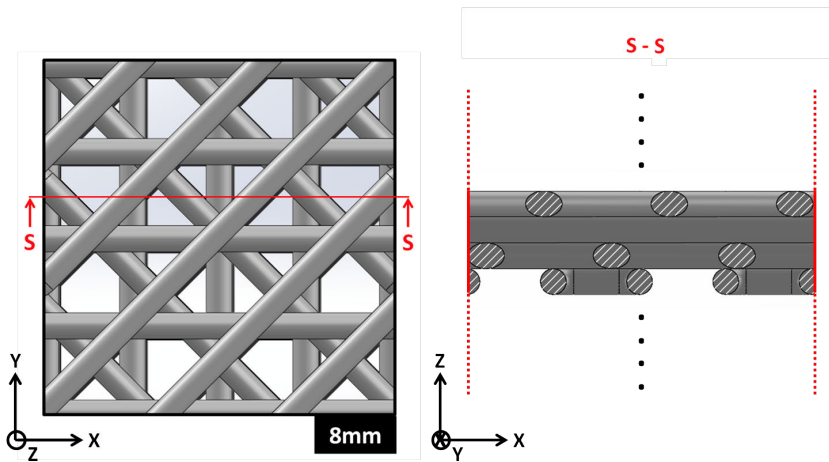
Tensile tests on ABS filament

Under uniaxial tension, the extruded filament of ABS exhibited a typical ductile behaviour, as shown by the nominal tensile stress vs nominal tensile strain curve in Figure 3.10. The material showed yielding at a strain level of $\approx 3\%$, and reached breakage at a strain level close to 35%. From the stress-strain curves obtained for the five different samples examined, the mechanical stiffness (Young's modulus, E_{ABS}) and strength (tensile stress at yield, $\sigma_{\text{y,t,ABS}}$) of the material were determined. E_{ABS} , evaluated from the slope of the curve in the initial linear region, resulted of 1910 ± 110 MPa (mean value \pm standard deviation); $\sigma_{\text{y,t,ABS}}$, taken at the peak of the curve, resulted of 36.2 ± 2.6 MPa. On the macro-scale, strain localization phenomena characterized by a progressive development of whitened zones along the deformed strand (Figure 3.10) were noticed during the test, just after yielding. These whitened zones should be directly related, on the micro-scale, with the deformation mechanism of voiding (rubber

3. ARCHITECTED DUCTILE POLYMER CELLULAR MODEL STRUCTURES PRODUCED BY 3D PRINTING



(a)



(b)

Figure 3.9: Morphological analyses of the cellular structures. (a) Top view (X-Y) of the cube-shaped structures with side 24,16,8 mm. The morphological repeating patterns of the smaller structures are detected in the larger ones (C_8 in C_{16} , C_8 and C_{16} in C_{24}) and highlighted by means of dashed lines of the corresponding colour. (b) Top view (X-Y) of the CAD 3D model of the C_8 structure, accompanied by the cross section (X-Z) of a single 4-layer basic unit, **S - S**.

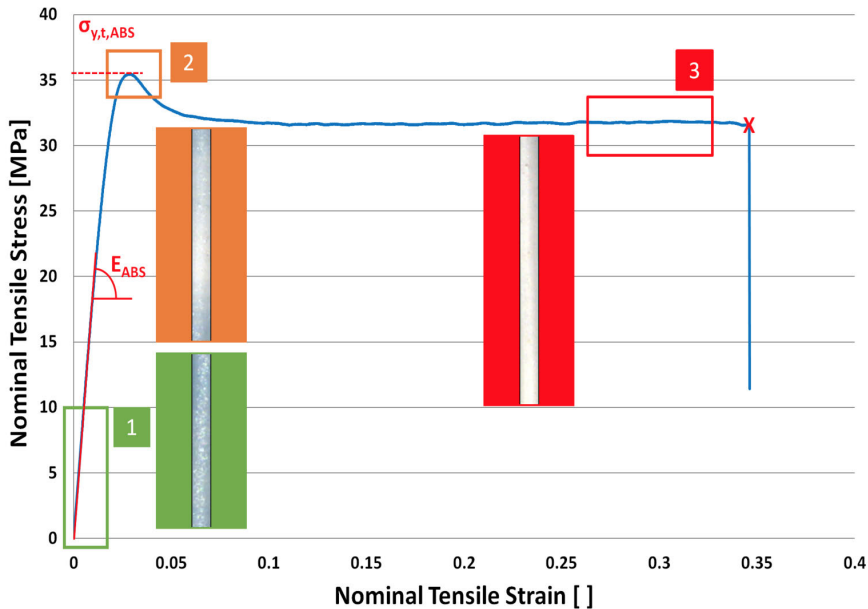


Figure 3.10: Nominal Tensile Stress vs Nominal Tensile Strain of the extruded ABS filament, accompanied by pictures of the specimen taken during the test.

particle cavitation and multiple crazing¹⁵). By increasing the applied strain, the whitened zones tend to coalesce up to the breakage of the strand.

Compression tests

The apparent stress, σ_{app} , vs apparent strain, ϵ_{app} , curves obtained from the monotonic compression tests carried out on the 3D-specimens are presented in Figure 3.11. The σ_{app} - ϵ_{app} curves of specimens loaded along the layer stacking direction show a characteristic trend,

¹⁵S. Agnelli et al., “Study of the plastic deformation behaviour of ductile polymers: Use of the material key curves,” *Mechanics of Materials* 117, no. July 2017 (2018): 105–115, ISSN: 01676636, <https://doi.org/10.1016/j.mechmat.2017.11.002>.

3. ARCHITECTED DUCTILE POLYMER CELLULAR MODEL STRUCTURES PRODUCED BY 3D PRINTING

irrespective of the type of 3D-specimen examined. The curves can be described using a tri-linear model, with three distinct regions (I, II and III) and the slope in region II smaller than the other two (Figure 3.11a). Between adjacent regions, the curve shows a knee, which is broader in the region II-III. The comparison of the four $\sigma_{app}-\epsilon_{app}$ curves obtained from the C_{16} specimens loaded along the Z direction (Figure 3.11b) provides an indication of the high repeatability degree of the results. This whole trend, up to test interruption, might be interpreted on the basis of the behaviour of an elastic-plastic cellular solid under compression presented by Gibson and Ashby.¹⁶ The three different regions would correspond to: the linear-elasticity region at low strain levels (region I); the structure plastic collapse zone (region II); the structure densification zone (region III). The actual confirmation that this interpretation could be appropriate also for the 3D-structures here examined, when loaded along the 3D-growth direction, was given by the results got from i) the compression cyclic tests (Figure 3.11c), and ii) the observation of the structures deformed at large strain levels (Figure 3.12). Indeed, for the cyclic tests (Figure 3.7b), the $\epsilon_{app,max,appl}$ applied to the specimen is assumed to be the sum of only two strain contributions: (i) a recoverable and (ii) a residual contribution (indicated with $\epsilon_{app,res}$). The latter is "stored" in the specimen and, due to the mainly elastic-plastic response of the constituent material (ABS), can be directly related to plasticity. In general, the $\epsilon_{app,res}$ data cannot be considered completely independent from the specific strain history applied during the experiment. Nevertheless, considering the specific scope of these experiments within the work, its influence on the outcomes can be assumed as negligible. The apparent residual deformation, represented as a function of $\epsilon_{app,max,appl}$ in Figure 3.11c, shows that irrespective of the size, the 3D-structures start accumulating residual strain at deformation levels (between 3% and 5%) just smaller than the region of the I-II knee in the $\sigma_{app}-\epsilon_{app}$ curves. This indicates that this knee can be therefore associated with the plastic failure of the specimen. The absence of

¹⁶Gibson and Ashby, *Cellular solids: Structure and properties, second edition*.

any residual strain contribution at the very beginning of the region I, at low strains, confirmed that the mechanical response could be considered as linear-elastic within this specific zone. In consideration of these outcomes, by resorting to a bi-linear representation of the curve around the I-II knee (Figure 3.11a), a stress value representative of the plastic failure of the structure ($\sigma_{\text{app, failure}}$) and an apparent elastic modulus of the structure (E_{app}) were determined and taken as indexes of the mechanical strength and stiffness of the structure loaded along the Z direction, respectively. Their values are reported in Table 3.1. It is worth noting that the viscoelastic character of the constituent material is inherently set aside, giving it only a secondary role in the mechanical response of the structure.

Figure 3.12 shows the internal sectional views of the C_{16} structure after deformation under compression along the Z direction at strain levels of 0%, 20%, 40% and 60%, and subsequent cryogenic fracture. They provide information about the deformation mechanisms associated with region II and III of the $\sigma_{\text{app}}-\varepsilon_{\text{app}}$ curve. A similar approach was adopted by Wang et al.¹⁷ The direct relationship between the structural details emerging from the image corresponding to the undeformed structure and the sectional view of the CAD model reported in Figure 3.9b clearly comes out. Assuming the four specimens nominally identical, the results in the different photos can be considered as consecutive frames of a unique progressive deformation process. By comparing the undeformed structure with that obtained at 20% strain, it can be observed that the structure collapses homogeneously at a macro-scale, via shape distortion and size reduction of the framed spaces defined by the ABS filament. Interestingly, whitened zones appear. Considering that ABS extruded filament whitening (Figure 3.10) is associated to voiding - a volumetric deformation mechanism under tension - it follows that the ABS walls in the 3D structure undergo local tensile stresses equal to $\sigma_{y,t, \text{ABS}}$ (36.2 ± 2.6 MPa). This

¹⁷Xinxin Wang et al., “Effect of geometric configuration on compression behavior of 3D-printed polymeric triply periodic minimal surface sheets,” *Mechanics of Advanced Materials and Structures* 30, no. 11 (2023): 2304–2314.

3. ARCHITECTED DUCTILE POLYMER CELLULAR MODEL STRUCTURES PRODUCED BY 3D PRINTING

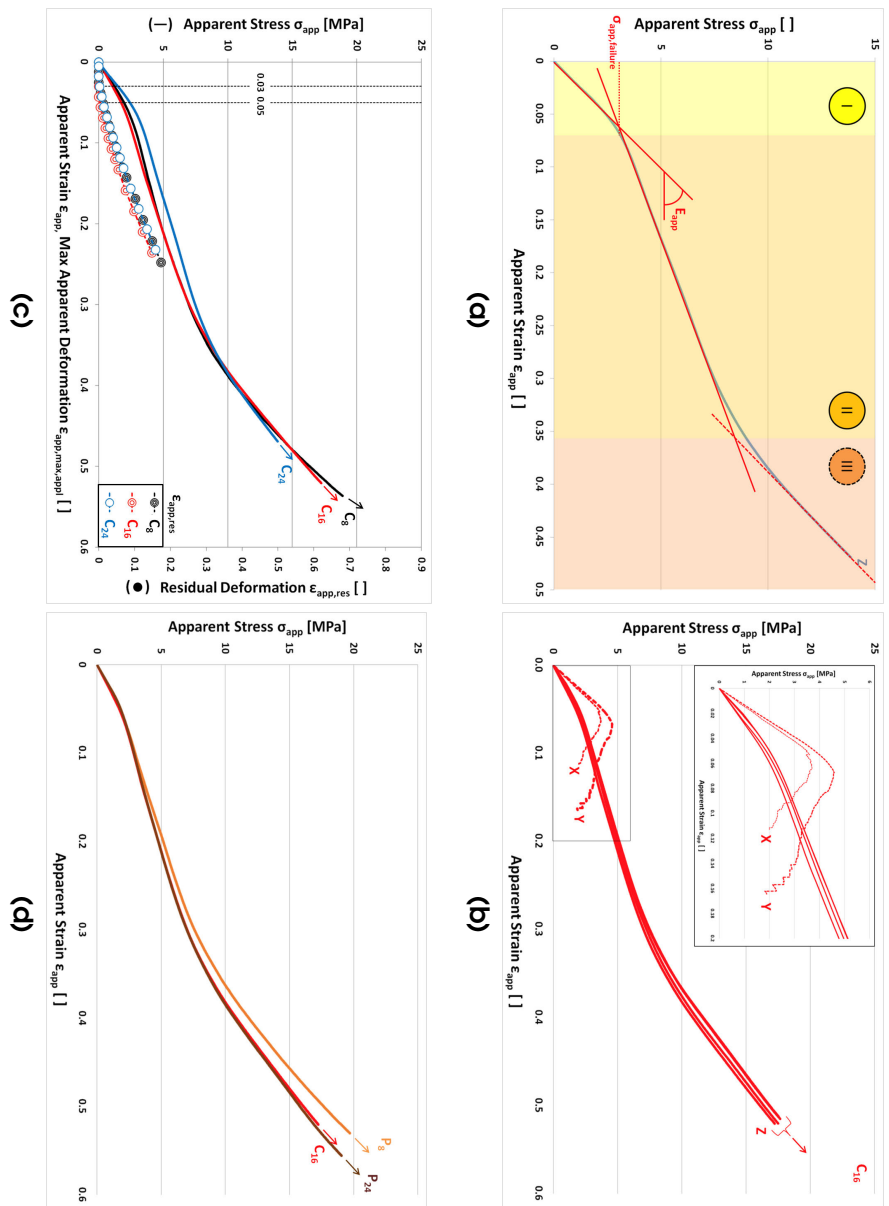


Figure 3.11

Figure 3.11: Compression tests on 3D printed cellular structures: output Apparent Stress, σ_{app} , vs Apparent Strain curve, ϵ_{app} . (a) Response of the cellular structures tested in Z (from a C_{24} specimen) and interpretation according to the tri-linear model proposed (see text). (b) Effect of testing direction (X, Y, Z), from tests carried out on C_{16} specimens. (c) Effect of size of cube-shaped specimens (C_8 , C_{16} , C_{24}) on the mechanical response of the systems in layer stacking direction, Z (-). In addition, the final results of compression cyclic tests, expressed in terms of Residual Deformation $\epsilon_{app,res}$, vs Max Apparent Deformation applied, $\epsilon_{app,max,appl}$, is reported (\bullet). The region where residual deformation starts to accumulate is indicated by black dashed lines. (d) Effect of height in specimens (P_8 , P_{16} , P_{24}) characterized by the same square base side length (16 mm), on the mechanical response of the systems in Z. Tests in Z are interrupted at about 50% apparent strain.

value is about seven times higher than the corresponding apparent stress resisted by the structure under compression at 20% strain (Figure 3.11b), and this confirms the high degree of complexity of the state of stress undergone at large strains by the material that forms a cellular solid.¹⁸ Figure 3.12 clearly shows that by increasing the level of applied deformation, the extent of shape distortion and cell size reduction increases giving rise to an evident densification of the structure. The whitened zones increase in number and area extension, and tend to concentrate along Z-oriented lines at the filament contact points between the stacking layers (see the image of the 40% deformed structure). The structures deformed at apparent strain levels of 20%, 40% and 60% exhibited non-recoverable strain levels of 9.6%, 29.2% and 51.3%, respectively. By comparing the data of $\rho_{rel,3D}$ measured on the deformed structures with those taken in the undeformed state, an increase in apparent density values of 7%, 29% and 54%, respectively, emerged. Interestingly, this outcome indicates the occurrence of densification already at an applied strain of 20%, which is right in the middle of the region II of the σ_{app} - ϵ_{app} curve (Figure 3.11a). Therefore, this specific region, initially associated

¹⁸Gibson and Ashby, *Cellular solids: Structure and properties, second edition*.

3. ARCHITECTED DUCTILE POLYMER CELLULAR MODEL STRUCTURES PRODUCED BY 3D PRINTING

only to the structure plastic collapse, has to be related also to structure densification. In agreement with Egan et al.,¹⁹ who worked on 3D-printed polymeric systems with 0° , 45° , 90° , -45° orientations and with relative density similar to that of the structures here examined, the occurrence of structure densification in the region II is probably at the basis of the slope exhibited by the $\sigma_{\text{app}}-\varepsilon_{\text{app}}$ curve in this specific region (largely higher than that expected for an ideal elastic-plastic behaviour, which is ≈ 0). By comparing the response (stress-strain curve) exhibited by the structures examined with that showed by other elastic-plastic cellular solids within the region II, it emerges that such a smooth trend (completely free of stress oscillations) seems to be typical of structures where struts in Z-direction are either not present^{20,21} or characterized by low slenderness. On the contrary, when such high-slenderness struts are present, a scattering trend with repeated peaks is typically observed^{22,23} which can be attributed to their local buckling.

Regarding the specimen size effects, the $\sigma_{\text{app}}-\varepsilon_{\text{app}}$ curves of the cube-shaped specimens with different sizes (C_8 , C_{16} , C_{24}) loaded along the Z direction (Figure 3.11c) show a very similar response for C_8 and C_{16} specimens, whereas C_{24} presents slightly higher stresses in both region I and II. Therefore, C_{24} has slightly higher values of

¹⁹Paul F Egan et al., “Mechanics of 3D-Printed Polymer Lattices with Varied Design and Processing Strategies,” *Polymers* 14 (2022): 5515, <https://doi.org/10.3390/polym14245515>.

²⁰Faezeh Shalchy, Christopher Lovell, and Atul Bhaskar, “Hierarchical porosity in additively manufactured bioengineering scaffolds: Fabrication & characterisation,” *Journal of the Mechanical Behavior of Biomedical Materials* 110, no. April (2020): 103968, ISSN: 18780180, <https://doi.org/10.1016/j.jmbbm.2020.103968>.

²¹Emilio Omar Bachtiar, Virginia Cary Ritter, and Ken Gall, “Structure-property relationships in 3D-printed poly(L-lactide-co- ϵ -caprolactone) degradable polymer,” *Journal of the Mechanical Behavior of Biomedical Materials* 121, no. April (2021), ISSN: 1751-6161, <https://doi.org/10.1016/j.jmbbm.2021.104650>.

²²Eren, Sezer, and Yalcin, “Effect of lattice design on mechanical response of PolyJet additively manufactured cellular structures.”

²³Wang et al., “Effect of geometric configuration on compression behavior of 3D-printed polymeric triply periodic minimal surface sheets.”

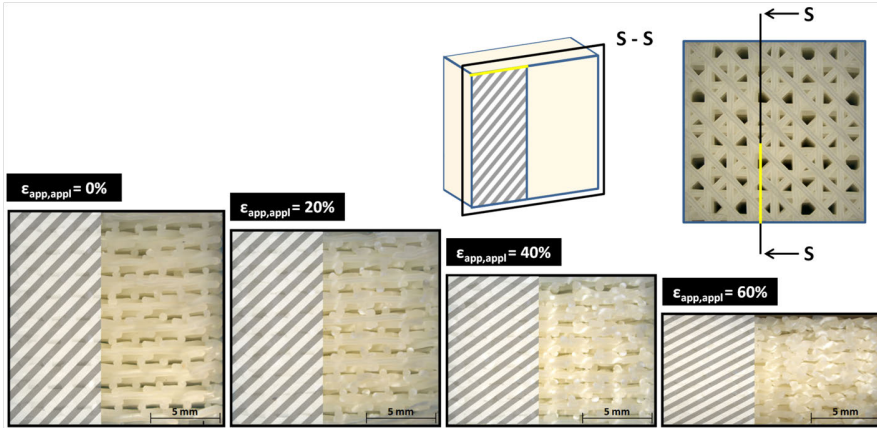


Figure 3.12: Optical microscope pictures of the **S - S** cross sections (from cryogenic fracture in liquid nitrogen) from four **C₁₆** specimens tested at different levels of $\epsilon_{app,max,appl}$ (0%, 20%, 40%, 60%). The sharp notch, introduced in the specimens (in the same position showed in Figure 3.9b) after testing, is indicated in yellow. The portion of specimen containing the notch is overshadowed using grey stripes pattern.

E_{app} and $\sigma_{app, failure}$, with respect to **C₈** and **C₁₆** (see Table 3.1). The response of the prism-shaped specimens having the same square base of **C₁₆** but different heights (**P₈** and **P₂₄**) - Figure 3.11d and Table 3.1 - suggests that the higher values of E_{app} and $\sigma_{app, failure}$ measured for **C₂₄** are related to its two-dimensional development on the X-Y plane rather than to its height. Indeed **P₂₄**, with same base of **C₁₆** and same height of **C₂₄**, exhibits the same stiffness of **C₁₆**, and even a smaller strength. The way the five different **C₁₆** structures (Figure 3.9a) combines to form the **C₂₄** specimen might be responsible of a synergistic effect that promotes the increase in the mechanical properties observed for **C₂₄**. Regarding the effect of the loading direction (Figure 3.11b), the compression response along a direction orthogonal to Z (either X or Y) shows a $\sigma_{app}-\epsilon_{app}$ curve very different from the tri-linear trend observed for compression along the Z direction. This peculiar trend is characterized by the achievement of a peak

3. ARCHITECTED DUCTILE POLYMER CELLULAR MODEL STRUCTURES PRODUCED BY 3D PRINTING

in the stress associated to the onset of delamination phenomena between two adjacent layers, originating from the weakest points of the structure. The progress of the delamination phenomena, even accompanied by buckling, explains the irregular stress decrease observed beyond the stress peak. The stress at the peak was taken as $\sigma_{app, failure}$ and, from the linear region of curve at very low strains, the value of E_{app} was determined (Table 3.1). As expected, given the geometrical symmetry of the structure, no difference was observed between the values of E_{app} and $\sigma_{app, failure}$ measured along X or Y. When loaded along a direction that is orthogonal to the layer stacking one, the structure is ≈ 1.8 times stiffer and ≈ 2 times stronger than along Z (from a forced relation between strength data associated to two different failure mechanisms).

Table 3.1: Specimens tested in compression tests (with indication of geometry, dimensions and loading direction) and mechanical properties measured under compression (in terms of Apparent Elastic Modulus, E_{app} , and Apparent Stress at Failure, $\sigma_{\text{app, failure}}$). For each property, the mean value \pm standard deviation is reported. The structures are full-fledged ACMs, being characterized by an effective porosity of $\approx 75\%$.

3D Compression Specimens						
Geometry	Nominal Characteristic Dimension ^a [mm]	Test Loading Direction ^b	Code	E_{app} [MPa]	$\sigma_{\text{app, failure}}$ [MPa]	
Cube	8	Parallel	C ₈	45 \pm 4.8	2.4 \pm 0.23	^c
	16	Parallel	C ₁₆	39 \pm 3.9	2.1 \pm 0.12	
	16	Orthogonal _x	C _{16-X}	71 \pm 2.7	3.9 \pm 0.47	
	16	Orthogonal _y	C _{16-Y}	71 \pm 3.9	4.2 \pm 0.53	
	24	Parallel	C ₂₄	54 \pm 3.9	3.0 \pm 0.29	
Prism ^d	8	Parallel	P ₈	40 \pm 3.5	2.3 \pm 0.43	
	24	Parallel	P ₂₄	40 \pm 1.2	1.5 \pm 0.13	

^a: for the cube-shaped specimens, the characteristic dimension is the length of the side of the cube; for the prism-shaped specimen, it is the height of the prism, read along the specimen 3D-growth direction according to the layer-to-layer fabrication approach of the FDM technology. ^b: "Parallel" indicates that the specimen loading direction used in the compression tests was parallel to the specimen 3D-growth direction; "Orthogonal" indicates that the loading direction was perpendicular to the specimen 3D-growth direction (subscript "X" or "Y" specifies the loading direction used in the test, as shown in Figure 3.1 and Figure 3.11b). ^c: Average of two values, measured on the two specimens with ρ_{rel} between 0.33 and 0.37 (Section 3.3); uncertainty determined as the semi-dispersion. ^d: Rectangular prism with 16mm-side square base.

3. ARCHITECTED DUCTILE POLYMER CELLULAR MODEL STRUCTURES PRODUCED BY 3D PRINTING

Following the approach typically used in literature for cellular solids,²⁴ the values of E_{app} and $\sigma_{\text{app, failure}}$, normalized over the elastic modulus and yield stress of the constituent material, E_{ABS} and $\sigma_{\text{y,t, ABS}}$ respectively, are plotted against the relative density, $\rho_{\text{rel, 3D}}$ (Figure 3.13a and 3.13b, respectively). One data-point corresponds to one specimen; the data-points corresponding to the two C₈ specimens having $\rho_{\text{rel, 3D}}$ outside 0.35 ± 0.02 (see Section 3.3) are also indicated. For both E_{app} and $\sigma_{\text{app, failure}}$, the data coming from the X and Y loading directions are visibly above those measured along the Z direction. The two series of data in the density region of interest are very well grouped, especially in the stiffness plot, and the data-points coming from the specimens with different sizes or heights mix well with each other. By referring to the data measured under compression along the Z direction, only the variation of $\rho_{\text{rel, 3D}}$ can induce an appreciable effect on the mechanical properties of the 3D-structure in agreement with the cellular material analysis approach²⁴ described by a power law curve:

$$y = d \cdot x^f \quad (3.2)$$

In Figure 3.13a, which refers to the stiffness, such a curve was traced imposing $d = 1$ and taking f as the mean of the f -values obtained by forcing this expression to each single Z direction data-point, including also those coming from the two C₈ specimens with $\rho_{\text{rel, 3D}}$ outside the region limited by the dot lines (the mean f -value resulted equal to 3.63). In Figure 3.13b, which refers to the strength, such a curve was traced according to the theoretical relationship proposed for the plastic-collapse strength of open-celled foams (with d and f equal to 0.3 and 3/2, respectively); it intercepts the group of experimental Z-direction data-points. The extent to which the constituent polymer (ABS) contributes to the 3D-structure stiffness is smaller with respect to that to which it contributes to the 3D-structure strength, in

²⁴Gibson and Ashby, *Cellular solids: Structure and properties, second edition*.

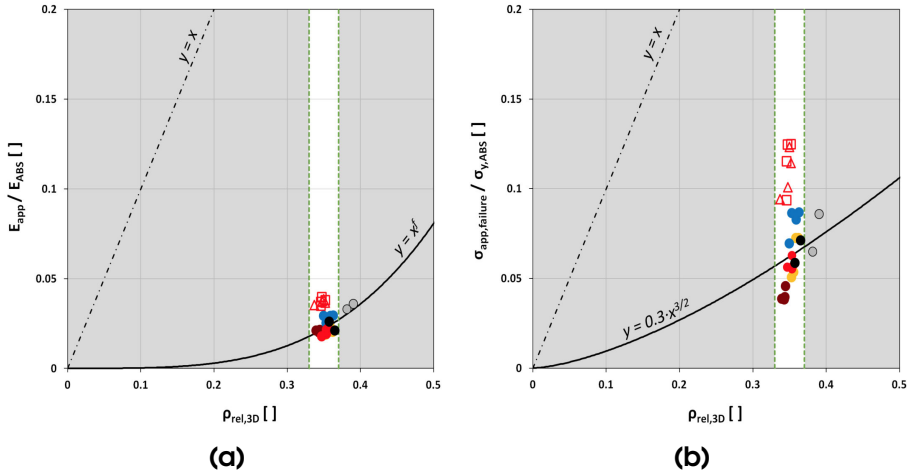


Figure 3.13: (a) Relative stiffness, E_{app}/E_{ABS} , and (b) relative strength, $\sigma_{app,failure}/\sigma_{y,ABS}$, as a function of the relative density, $\rho_{rel,3D}$, of the 3D-structures. ●: data-points from tests carried out with the loading direction parallel to the layer stacking direction (black, C₈; red, C₁₆; blue, C₂₄; orange, P₈; brown, P₂₄; grey circles refer to C₈ specimens with $\rho_{rel,3D}$ outside 0.35 ± 0.02). Red open symbols: data-points from tests carried out with the loading direction orthogonal to the layer stacking direction (\triangle , C_{16-X}; \square , C_{16-Y}). The continuous line is the power law curve traced according to equation (3.2) by using $d = 1$ and $f = 3.63$ in (a) and $d = 0.3$ and $f = 3/2$ in (b) (see text). Vertical dashed lines traced at $\rho_{rel,3D} = 0.33$ and at $\rho_{rel,3D} = 0.37$.

agreement with what observed by Pagano et al.²⁵ for a very different 3D-structure manufactured by FDM (based on a different polymer, with a different architecture and much denser).

²⁵Claudia Pagano et al., “Relationships between size and mechanical properties of scaffold-like structures,” *Mechanics of Advanced Materials and Structures* 28, no. 17 (2021): 1812–1817, ISSN: 1537-6494, <https://doi.org/10.1080/15376494.2019.1709675>.

Tensile tests

The apparent stress, σ_{app} , vs apparent strain, ϵ_{app} , curves obtained from the monotonic tensile tests carried out on the 3D-specimens are presented in Figure 3.14a. For each infill level, an high degree of repeatability, both in terms of low-strain (elastic) and high-strain (post-yield) behaviour, was recorded between the various specimens tested. The only exception was in the 82% infill series, where two different responses (provided by two specimens each) could be observed. The apparent deformation, ϵ_{app} , determined directly from the crosshead displacement, has a global nature. In order to assess the validity of this parameter from a more local point of view, additional visual analyses were performed, by recording the tests (one specimen per infill level) with an high-speed camera. The local deformation was evaluated on different positions of the specimens (left side, centre and right side) in various moments during the tests, and the results obtained were correlated with the corresponding (from time perspective) global values, as reported in Figure 3.14b. No effect of the position selected for local deformation was observable, since visual analyses on left side, centre and right side resulted in extremely similar trends. The local strain values obtained were in accordance to the global results, as testified by the slope of the curves very close to 1. Thus, the global approach can legitimately be used as a reliable measure of the deformation during the tests. However, it has to be pointed out a slight general overestimation when considering the crosshead-related global strain, in comparison with the more punctual approach based on local strain. In consideration of these outcomes, an apparent elastic modulus of the structure (E_{app}) was determined as the slope of the initial linear elastic region of the curves (considering the global ϵ_{app}), and taken as an index of the mechanical stiffness of the structure loaded orthogonally to the 3D layer stacking direction, Z. For each infill level, mean values of elastic modulus \pm standard deviations were determined. While being aware of the two different responses, the same approach was applied to

the case of 82% infill as well, leading inevitably to higher standard deviation values. The results are reported in Table 3.2.

Eventually, it is worth recalling the extremely complex nature of the systems under analysis, in particular linked to (i) the absence of struts in Z-direction and (ii) cell walls defined by a single filament of polymeric material, which assumes the role of basic the structural element. For such peculiar systems, a fundamental study aimed at the evaluation of the effect of tensile and compressive test conditions on their mechanical response - at fixed basic architecture - still lacks in literature. Considering this, the study here proposed, consisting in design, manufacturing and testing of *ad-hoc* specimens in tensile conditions turned out to provide promising results. However, it has to be stressed the tentative nature of such analysis, and the possible uncertainties linked to it, especially in terms of (i) selection of suitable and representative specimen geometries and (ii) load distribution at the interface between the central region - with variable porosity levels - and the end zones, produced at maximum infill. Thus, the comparison of the results, in terms of elastic modulus, between compressive and tensile conditions seems premature at the moment, suggesting the possibility for a future comprehensive study of the geometry effect on the mechanical response to be useful to shed light on it.

Following the approach proposed by Gibson and Ashby²⁶ (and already used for compression tests), relationships between the mechanical properties and the system-related parameters were researched. More specifically, the mean elastic modulus values were represented as a function of the apparent density, ρ_{app} , by recalling that the ρ_{app} values used here refer to one single specimen per infill level, considered as representative of the corresponding series (see Section 3.2 for more details). The graph, expressed on logarithmic axes, was reported in Figure 3.14c. An evident correlation was clearly observable, testifying the strong dependency of the mechanical property on the apparent density in tensile configuration as well.

²⁶Gibson and Ashby, *Cellular solids: Structure and properties, second edition*.

3. ARCHITECTED DUCTILE POLYMER CELLULAR MODEL STRUCTURES PRODUCED BY 3D PRINTING

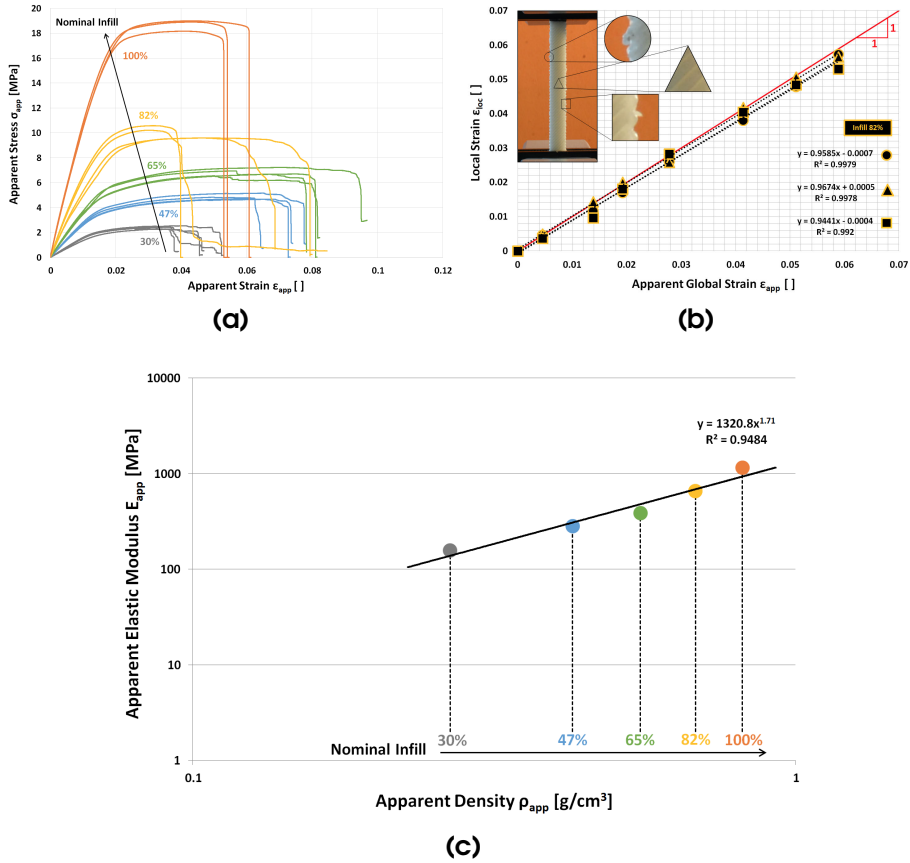


Figure 3.14: Tensile tests of 3D specimens with varying infill levels (30%, 47%, 65%, 82%, 100%): (a) Apparent Stress, σ_{app} , vs Apparent Strain, ϵ_{app} , curves, output of the tests; (b) comparison between global strain, ϵ_{app} , evaluated from crosshead displacement, and local strain, ϵ_{loc} , determined from high-speed image analysis, in the 82% infill scenario. \circ , \triangle and \square shapes refer to different positions on the specimen, where the image analysis was performed (left, centre and right, respectively); (c) Apparent Elastic Modulus, E_{app} , vs Apparent Density, ρ_{app} data, represented in logarithmic axes, accompanied by the best fit trend line. For each infill level, the ρ_{app} is calculated on a single specimen, considered as representative of the corresponding series, while E_{app} refers to the mean value within the series (see Section 3.2 for more details).

Table 3.2: Specimens tested in tensile tests (with indication of geometry, loading direction and nominal infill levels) and mechanical stiffness measured under tension (in terms of Apparent Elastic Modulus, E_{app}). The data are reported as mean value \pm standard deviation.

3D Tensile Specimens			
Geometry	Test Loading Direction	Infill [%]	E_{app} [MPa]
Prism ^a	Orthogonal ^b	30	158 \pm 10
		47	284 \pm 10
		65	385 \pm 16
		82	657 \pm 82 ^c
		100	1160 \pm 40

^a: Rectangular prism with $B \times W \times L = 4 \times 8 \times 120 \text{ mm}^3$. ^b: "Orthogonal" indicates that the specimen loading direction used in the compression tests was orthogonal to the specimen 3D-growth direction. ^c: Average of four values, referring to two different mechanical responses.

Fracture behaviour

Load, P , vs displacement, u , curves were obtained as output from fracture tests on series A and B specimens. The series A activity was specifically designed to evaluate the effect of different notching procedures on the apparent elastic modulus derived from fracture tests, $E_{app,f}$, as well as to tailor the compliance correction test methods and evaluate the impact of indentation on the results. Images taken at the optical microscopy of the notch region in the 30% and 100% infill specimens, accompanied by a_0 and a_0/W values, are reported in Figure 3.15a. Apparent elastic modulus was determined from raw curves according to equations (2.16-2.21), leading to the results showed in Figure 3.15b (\triangle indicator). However, data had to be properly corrected to take into account the indentation effect during the tests. The standard procedure for data correction, well established

3. ARCHITECTED DUCTILE POLYMER CELLULAR MODEL STRUCTURES PRODUCED BY 3D PRINTING

in FM of ductile polymeric materials,²⁷ required the determination of the compliance lines in the initial linear region for both fracture and correction tests. The corrected fracture test curve was then characterized by an initial linear region with slope equal to the difference of the so-obtained stiffnesses. However, unlike the case of *continuum*, the fully-developed elastic regions in fracture and correction tests were reached at significantly different load levels in the systems under analysis (see Figure 3.17a, which shows equivalent results for a 30% infill series B representative specimen fracture and correction curves). Thus, it was expected that the standard procedure would not have produced reliable results, as the stress state experienced by the polymeric material in the two experimental configurations could not be considered as comparable. The rigorous approach adopted during the structure research activity was then applied, by searching for more promising alternatives. As correction curves reached far higher load levels, in comparison with raw fracture data, the selected solution required the determination of the difference of displacement values, at fixed load. Thus, each data point of the corrected curve was characterized by a corrected displacement, to be evaluated as the difference between values obtained in the same stress conditions (Figure 3.17b). The compliance of the corrected curve was determined from the slope of the initial linear elastic region and then used in equation (2.16) to obtain the corrected elastic modulus, derived from the compliance in fracture tests (▲ indicator in Figure 3.15b). From the comparison between raw and corrected data, both 30% and 100% infill specimen present a relevant effect of indentation on the low-strain fracture response. Interestingly, if percentage variations are considered, no substantial differences were observed between the two extreme porosity configurations. Thus, in relative terms, the effect of indentation can be considered as equivalent both in the highly-compliant 30% and in the stiffer 100% infill case. From a more quantitative point of view, by comparing the mean values

²⁷Moore, Williams, and Pavan, *Fracture mechanics testing methods for polymers, adhesives and composites*.

across the different series of data points, indentation causes at least a 20% underestimation in the value of $E_{app,f}$ (see Table 3.3 for further information). Further, as extreme a_0/W ratios had to be overlooked according to classic FM theory²⁸ (for which boundary effect contribution is significant), $E_{app,f}$ resulted almost constant in the interval $0.3 \leq a_0/W \leq 0.7$, proving its independence from the normalized crack length.

The same data analysis procedure was adopted for specimens belonging to the series B, where the crack was obtained via notching machine. Load levels in correspondence of the fully-developed initial linear elastic regions for raw and correction curves were not comparable. Thus, it was necessary to rely on the displacement analysis at same load once more. The corrected $E_{app,f}$ mean values and corresponding standard deviations for each infill level (30%, 47%, 65%, 82%, 100%, three specimens each) were reported in Table 3.3.

In order to evaluate the effect of the different notch introduction technique, the $E_{app,f}$ results coming from both series A and B were plotted, on logarithmic axis, as a function of the normalized initial crack length, a_0/W , as represented in Figure 3.16 (▲ and ● indicators, respectively). It clearly emerges the high degree of repeatability of the results within a specific infill level, already observed for series A and now confirmed by series B analysis. Further, in the case of 30% and 100%, no relevant differences could be observed between outcomes from series A and B. This is an extremely important result, as it allows to state the non-sensitivity of $E_{app,f}$ to the notch introduction technique used, leading to the substantial equivalence of the two different approaches. Series A notches were inherently forced to assume specific values, depending on the filament thickness, as a result of the FDM machine deposition. Thus, the notching machine used for the preparation of series B specimens, where blade advancement (and the consequent crack lengths) was controlled by a micrometer, was expected to be a more versatile and accurate technique. This was confirmed by the degree of repeatability of a_0/W results, which not

²⁸Anderson, *Fracture Mechanics : Fundamentals and Applications*.

3. ARCHITECTED DUCTILE POLYMER CELLULAR MODEL STRUCTURES PRODUCED BY 3D PRINTING

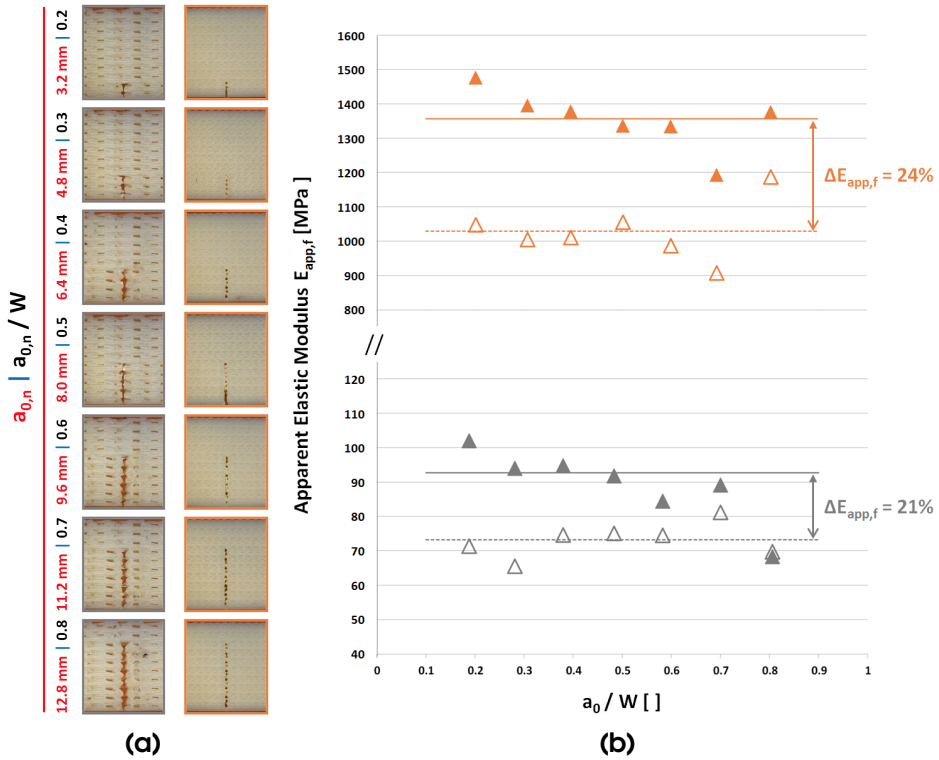


Figure 3.15: Series A - Printer Notch: results of the experimental activity. (a) Optical microscopy images of the 3D-printed notch in 30% and 100% nominal infill specimens. For each infill level, the nominal initial crack length, $a_{0,n}$, and the normalized crack length, $a_{0,n}/W$, are indicated; (b) Apparent Elastic Modulus from fracture tests, $E_{app,f}$, as a function of $a_{0,n}/W$, for both infill levels. Y-axis is interrupted for the sake of representation and clarity. \triangle stand for elastic modulus data before compliance and indentation correction tests were performed, while \blacktriangle refer to corrected data. Mean values of non-corrected and corrected data are represented with dashed and full lines, respectively (the 30% specimen with highest $a_{0,n}/W$ was excluded in these calculations). The % error (underestimation) between mean values obtained if corrections tests were not performed are reported for both infill levels.

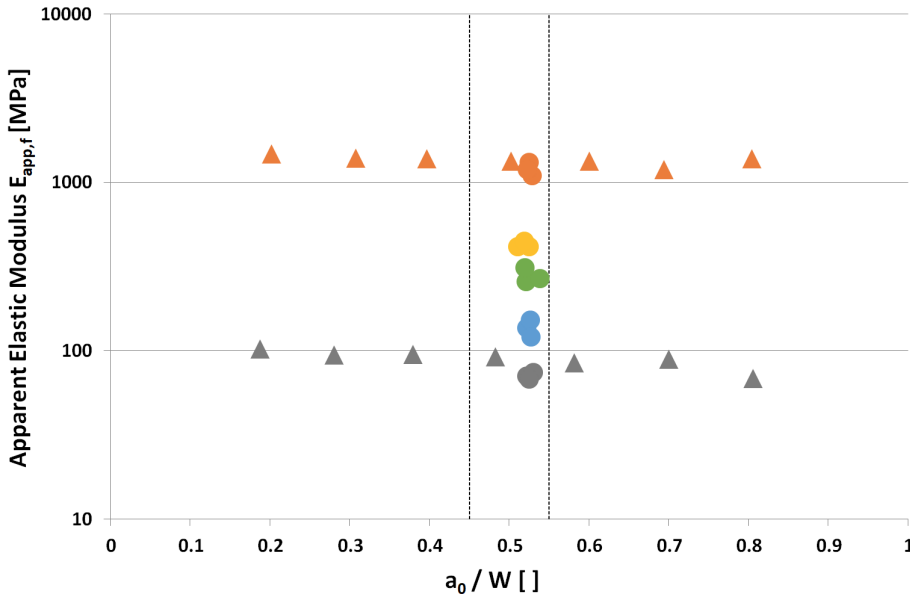


Figure 3.16: Series A - Printer Notch (▲) and Series B - Blade Notch (●): comparison of the results for specimens with varying infill level (30%, 47%, 65%, 82%, 100%). Apparent Elastic Modulus from fracture tests, $E_{app,f}$, vs normalized crack length, a_0/W . Y-axis is represented in logarithmic scale for improved visualization. Black dashed lines delimitate the target interval $0.45 \leq a_0/W \leq 0.55$ desired during the notching phase of series B specimens, according to classic theory of FM.

only respected the target condition $0.45 \leq a_0/W \leq 0.55$ required by FM,²⁹ but also turned out to be located into a much narrower window. Summing up, at the end of this activity the notching machine was legitimately selected to be the preferential way for proper notch introduction, as it provided reliable and consistent results and higher versatility and accuracy in the cutting process.

²⁹Anderson, *Fracture Mechanics : Fundamentals and Applications*.

Table 3.3: Specimens tested in fracture tests (with indication of geometry, loading direction and nominal infill level). The elastic modulus from fracture tests, $E_{app,f}$, is reported for both Series A and B (corresponding to different notching techniques, see text). Fracture toughness at initiation $J_{c,i}$, and at a specific point representing undoubted crack propagation $J_{c,iN}$ (see text) are reported for Series B specimens (mean value \pm standard deviation).

3D Fracture Specimens						
Geometry	Test Loading Direction	Infill [%]	Series A		Series B	
			$E_{app,f}$ [MPa]	$E_{app,f}$ [MPa]	$J_{c,i}$ [N/mm]	$J_{c,iN}$ [N/mm]
		30	89 ± 9.9	71 ± 2.6	0.78 ± 0.09	0.93 ± 0.07
		47	-	136 ± 13	0.49 ± 0.05	0.73 ± 0.08
SE(B) ^a	Parallel ^b	65	-	279 ± 23	0.66 ± 0.2	0.98 ± 0.33
		82	-	424 ± 15	0.42 ± 0.2	0.79 ± 0.33
		100	1356 ± 80	1201 ± 90	1.23 ± 0.3	1.90 ± 0.38

^a: Single Edge notched in Bending, SE(B), specimen. Rectangular prism with $B \times W \times L = 8 \times 16 \times 80$ mm³ and nominal initial crack length $a_{0,n} = 8$ mm, tested with span $S = 4W = 64$ mm. ^b: "Parallel" indicates that the specimen loading direction used in the fracture tests was parallel to the specimen 3D-growth direction.

After dealing with the low-strain fracture behaviour, characterized by $E_{app,f}$, the analysis was focused on crack initiation and propagation during testing. The peculiar nature of the systems under analysis, characterized by complex architecture and high degree of porosity, required extra-care in dealing with such phenomena, with respect to the *continuum* case. Thus, fracture tests were accompanied by high resolution image acquisition (1 image per second), to provide real-time information about the damage phenomena, at least at the macro-scale. Further, from the point of view of data elaboration, a dual approach was followed: the analyses of the loading curves, direct output of the tests, and of the corresponding image sets, were performed separately, to avoid mutual influence of the outcomes during the elaboration phase. Starting from loading curves, just for exposition purposes, their peaks were identified and marked, as they were supposed to be points where some kind of damage was induced. The nature of such damage could not be directly inferred, however the peaks' height was regarded as a potential indicator about the underlying mechanisms (filament decohesion or crack propagation), as well as provide information about damage magnitude. Then, the analysis of high resolution images taken during the tests was performed, by detecting both morphological changes in the structures and eventual crack propagation. The frames where such variations took place were selected and then correlated with the corresponding data points on loading curves, by resorting to time values comparison (directly provided by the test machine, indirectly determined in the case of camera images). Figure 3.17c shows the data elaboration method applied to a representative series B specimen with 30% nominal infill. A good agreement was found in the outcomes of the two independent approaches. Further, camera images analysis allowed to provide meaning to load drops, by discriminating between filament relative movements and decohesion and actual crack propagation. Thus, it was possible to determine the fracture process initiation, represented as \bigcirc in Figures 3.17c-3.17d. The entire procedure was repeated for all infill levels, with 3 specimens tested each. While being confident

3. ARCHITECTED DUCTILE POLYMER CELLULAR MODEL STRUCTURES PRODUCED BY 3D PRINTING

about the validity of the elaboration method, as well as of the results obtained, it was decided to go one step forward, in search of an upper bound for fracture initiation. By considering both initiation (P_i) and maximum (P_{max}) load levels, specific data points (P_{iN}) were selected according to the relationship

$$P_{iN} = P_i + \frac{P_{max} - P_i}{N} \quad N \in \mathbb{N}^+ \quad (3.3)$$

More specifically, an esteem of a suitable increase in load values - such that crack propagation in the corresponding data point was undeniably going on - was researched. Such increment was expressed as the normalized difference between P_{max} and P_i over N , where N had to be tailored in order to fit the desired task. Ideally, the fraction had to assume the lowest value, so that the corresponding data point was as close as possible to initiation. By resorting to the camera images inspection, $N = 4$ turned out to be a suitable value. The results of this analysis were reported in Figure 3.17d with ● indicator, for each specimen and infill level. The importance of this rigorous approach and the corresponding results obtained can not be stressed enough. Thus, a bunch of points have to be noted:

- First, it is fundamental to remember that, in the case of *continuum*, more critical stresses are experienced in the inner part of the specimens - rather than on the surfaces - thus leading to more likely crack initiation. As a consequence, the individuation of fracture initiation turned out to be extremely difficult from merely surface observations, and supposed to be preceded by real initiation in the inside, dominated by plain strain conditions. In the case of cellular materials, as porosity grows, the *continuum* approach increasingly fails to accurately describe the response of the systems. Further, the possibility to detect structural failure from high-resolution images progressively increased with the porosity degree.

- The curves-images synergistic approach proved that fracture initiation took place in correspondence of discontinuities in loading curves, sometimes in the form of full-fledged load drops, sometimes as significant slope variations. This is an extremely important result, as it suggests that such local events could be traced by referring to the macroscopic global response of the specimen.
- The possibility of inherent uncertainties in the position of the initiation point, due to non-detected damage mechanisms at lower scale and errors in datapoints-images synchronization, has to be taken into account; however, by setting a rock-solid upper threshold, reliable information about the maximum error in the evaluation of initiation point could be obtained, allowing to focus the attention on a narrower region of the curve, in further analyses aimed at studying the nature of fracture mechanisms.

In classical literature about FM of ductile polymers, the material toughening resulting from crack propagation was studied by resorting to data at different crack lengths. However, the high complexity, heterogeneity and porosity of the structures under analysis prevented from applying this method straightforwardly, suggesting that fracture toughness data evaluated at the initiation point would have been more representative of the true response of the systems.

Following the classic approach used for cellular materials by Gibson and Ashby,³⁰ the mechanical properties were plotted as a function of density and expressed in relative terms. Relative Elastic Modulus, E_{rel} , vs Relative Density, ρ_{rel} , graph was reported in Figure 3.18. Data for each infill level were reported as mean values and standard deviations. Further, the *continuum* case, characterized by unitary values on X- and Y-axis, was indicated as limit condition. Thanks to the use of a variety of significantly different infill levels in design phase, the data

³⁰Gibson and Ashby, *Cellular solids: Structure and properties, second edition*.

3. ARCHITECTED DUCTILE POLYMER CELLULAR MODEL STRUCTURES PRODUCED BY 3D PRINTING

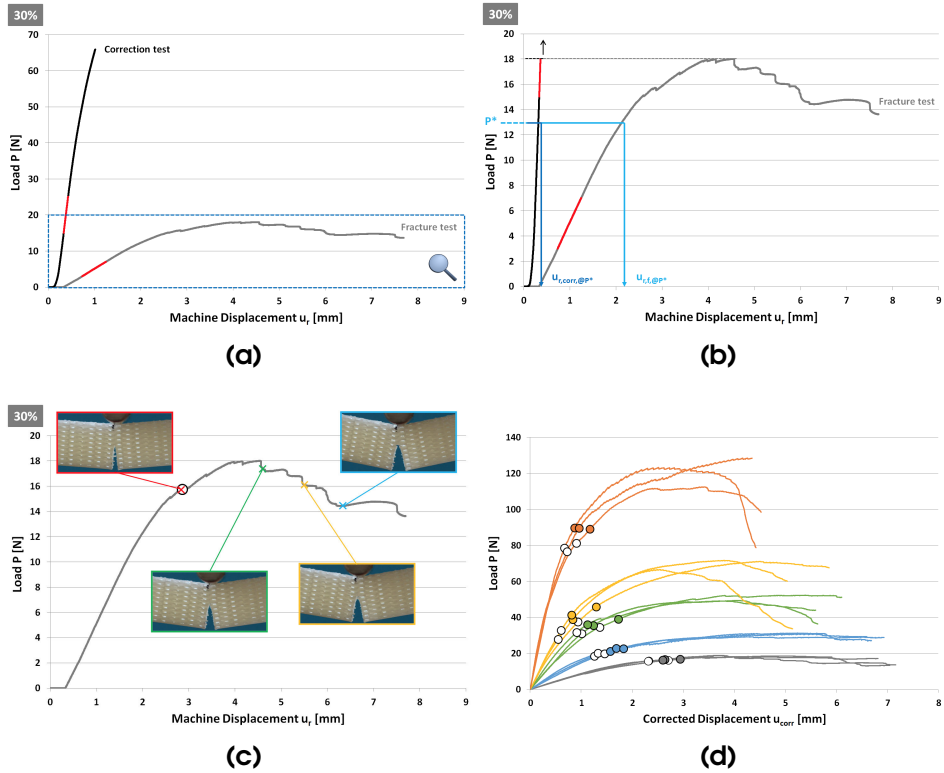


Figure 3.17: Series B - Blade Notch. (a) Raw loading curves from fracture and correction test on a representative 30% nominal infill specimen. The initial linear elastic regions are indicated in red; (b) magnification of the raw loading curve from fracture test: the procedure of displacement identification at same load level (P^*) is represented; (c) correlation between camera images and loading curve analysis in correspondence of morphological and structural changes; (d) Load, P , vs Corrected Displacement, u_{corr} , curves from specimens with varying infill level (30%, 47%, 65%, 82%, 100%, three curves each). The curves are preliminary shifted and then linearized. ○ refer to the fracture initiation point (see text for more details), while ● stand for specific points of undeniable crack propagation.

spanned across a wide range in relative density, thus allowing to draw some meaningful conclusions about the trend observed. Specimens with nominal infill level up to 82% - corresponding to $\rho_{\text{rel}} \approx 0.65$ - were characterized by E_{rel} values drawing a unique trend, which was fitted by using a power law function: thus, the same type of relationship expected in compression tests in by Gibson and Ashby³⁰ was observed for fracture tests, characterized by significantly different stress conditions. This means that systems characterized by a wide range of porosity levels and micro-architectural parameters, share the same low-strain fracture response. Interestingly, when increasing the infill level even further, approaching the most *continuum*-like conditions, the trend was no longer valid: indeed, in the case of 100% nominal infill ($\rho_{\text{rel}} \approx 0.8$), the dispersion of relative modulus data radically increased, while the mean value resulted far higher in comparison with model prediction. Such outcome could be explained by hypothesizing a transition region when reaching conditions close to *continuum*-like configuration.

After dealing with low-strain response, the attention was focused on the initiation of fracture process. The Fracture Toughness at Initiation, $J_{\text{c,i}}$, and in conditions of undeniable crack propagation, $J_{\text{c,iN}}$, were calculated according to Equation (2.27). Thus, this FM relationship - which assumes the absence of crack advancement, as well as the validity of the *continuum* hypothesis - was used in the very early stages of fracture propagation as well. The fracture toughness data were plotted against the relative density, ρ_{rel} , as represented in Figure 3.19 (○ and ● indicator, respectively). Data were reported as mean values, accompanied by the corresponding standard deviation bands. The amplitude of data variability increased with ρ_{rel} , suggesting that eventual defects in filament deposition within the same class of specimens could play a more relevant role on fracture response in the case of low-porosity systems. The fracture toughness of the systems, both at initiation and in propagation conditions, resulted almost constant over a wide range of infill levels, up to 82%, thus resulting independent of the micro-architecture of structures. Inter-

3. ARCHITECTED DUCTILE POLYMER CELLULAR MODEL STRUCTURES PRODUCED BY 3D PRINTING

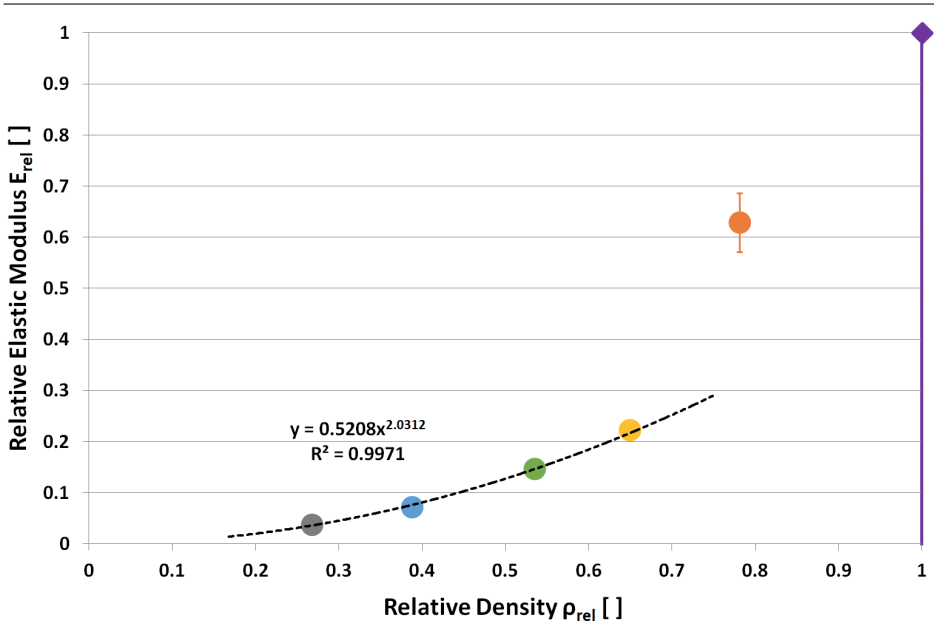


Figure 3.18: Series B - Blade Notch. Relative Elastic Modulus, E_{rel} , vs Relative Density, ρ_{rel} for specimens with varying infill level (30%, 47%, 65%, 82%, 100%). The represented data are mean values (●), accompanied by standard deviation bands. In addition, the *continuum* configuration, characterized by unitary value in relative properties, is represented as limit case in cellular materials analysis (◆). The best fit power law trend, forced on data points corresponding to 30% to 82% infill levels, is represented by black dashed line, and its equation indicated alongside.

estingly, as already pointed out for $E_{app,f}$, data for 100% nominal infill were not aligned, assuming far higher values, indeed. Such outcome was regarded as a further indication of the presence of a transition region when *continuum*-like conditions were approached. In search of evidences supporting/disproving this hypothesis, the structure of the architected systems was analyzed (Figure 3.19). More specifically, it was observed that filament junctions were limited to *inter*-layer type in specimens up to 82% infill level: thus, the only junction points in the entire structures were those where contact between filaments in

two consecutive layers, during material deposition, was realized. On the contrary, further analyses on 100% infill specimen at the optical microscope pointed out the presence of *intra*-layer type junctions, in addition to the *inter*-layer previously discussed. More in detail, the infill level imposed during the design phase was so high that no space remained between consecutive windings of filament within the same layer, regardless of its orientation: thus, additional contact surfaces, with far larger extension in comparison with the still present *inter*-layer contribution, were realized in this configuration.

This outcome was confirmed by the 3D-CAD models of the structures, as well as by further more in-depth visual analyses. For each infill level, the dimensions, spacing and fillet radii of the filaments, determined from layers of actual representative specimens, were used to build-up a 3D-CAD model of the real structures, as obtained from the FDM machine. Sections taken in correspondence of the position of notch introduction (see Figure 3.20) pointed out the discontinuous nature of the crack front, where filament and void regions were intercepted in an alternate form. It is important to recall that notches were introduced in the same position in each specimen, and that the resulting cracks front were located in correspondence of the same layer. This finding, being accurate up to 82% infill level, was no longer valid in 100% infill configuration, where contact and occasionally superposition between *intra*-layer adjacent filament windings was detected by optical microscopy analyses and then reported in the CAD model. Thus, in this specific scenario, the crack front turned out to be continuous, as close as possible to the *continuum* case. However, the nature of the systems - characterized by juxtaposition of filament - was regarded to be the primary responsible for fracture toughness values significantly different from *continuum* ABS material: more specifically, even in the case of maximum packing, the contact and adhesive properties of the junctions between filaments were considered to play a dominant role, in comparison with the bulk material properties.

Finally, by normalizing properties over apparent density, the relationship between fracture toughness at initiation, $J_{c,i}/\rho_{app}$, and elastic

3. ARCHITECTED DUCTILE POLYMER CELLULAR MODEL STRUCTURES PRODUCED BY 3D PRINTING

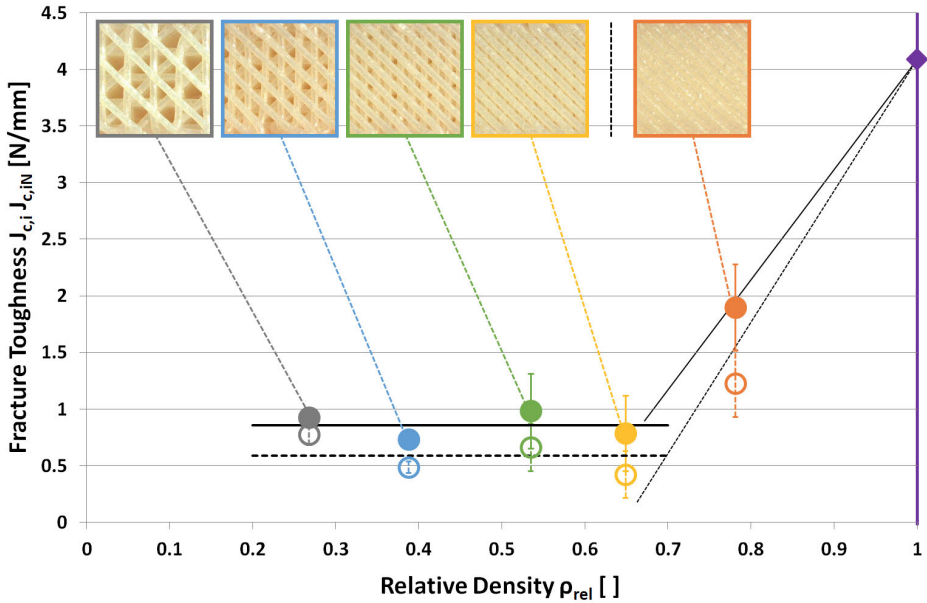


Figure 3.19: Series B - Blade Notch. Fracture Toughness, $J_{c,i}$ and $J_{c,iN}$, vs Relative Density, ρ_{rel} for specimens with varying infill level (30%, 47%, 65%, 82%, 100%). Subscript c,i (\circ) and c,iN (\bullet) refer to initiation and in-progress propagation points, respectively. The *continuum* configuration, characterized by unitary value in relative properties, is represented as limit case in cellular materials analysis (\blacklozenge). Standard deviation bands are indicated as well. Mean values forced on data points corresponding to 30% to 82% infill levels, are represented as black lines. In addition, thin black lines are drawn in the transition region characterized by increasing fracture toughness with increasing ρ_{rel} , for the sake of representation. Optical microscopy images of the structures used for data interpretation are reported as well.

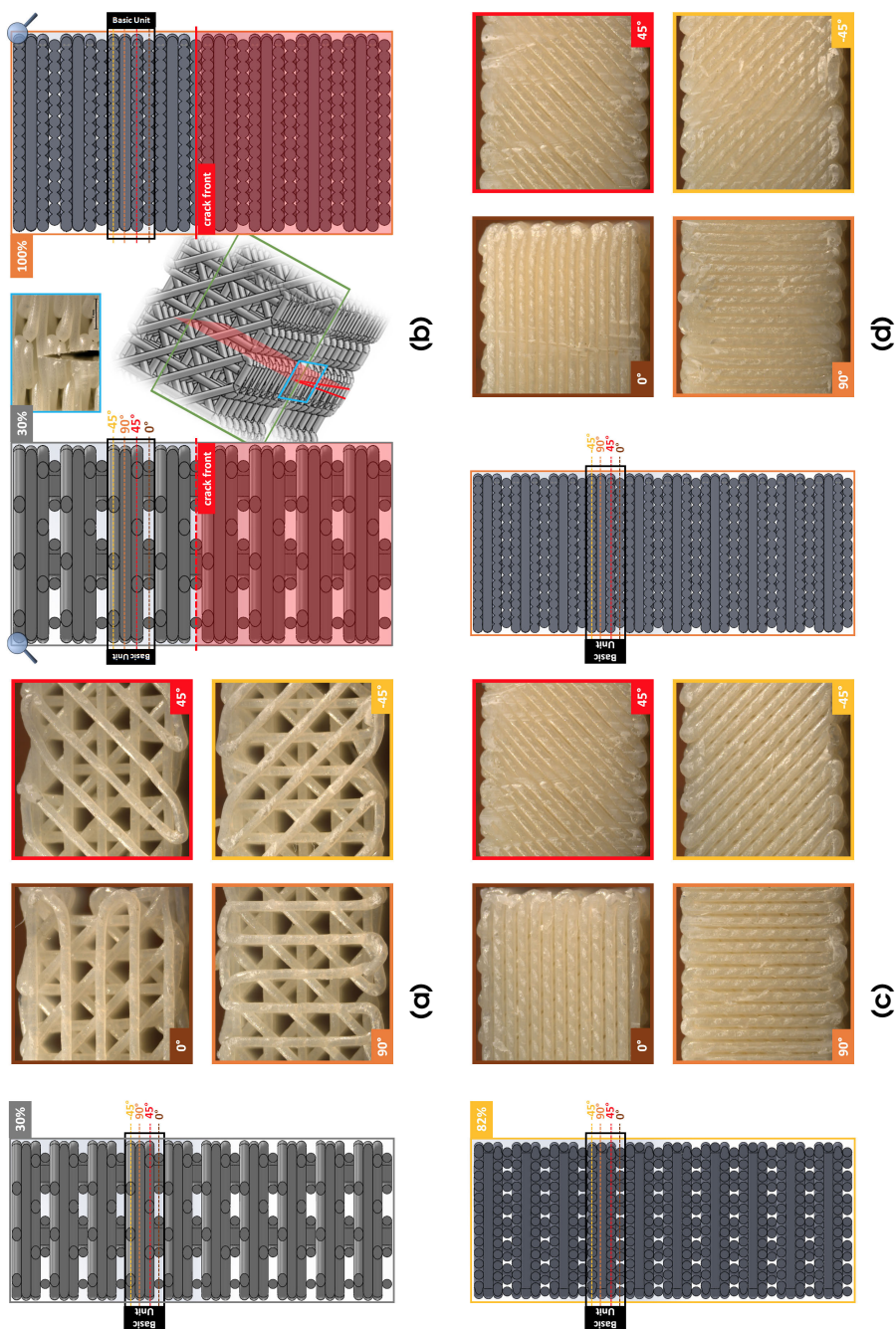


Figure 3.20

3. ARCHITECTED DUCTILE POLYMER CELLULAR MODEL STRUCTURES PRODUCED BY 3D PRINTING

Figure 3.20: 3D-CAD model of the architected cellular materials with infill levels of (a) 30%, (c) 82%, (d) 100% : sections taken in correspondence of the position selected for notch introduction. For each infill, the images of the 4 basic unit representative layers, used to detect the actual size - dimensions, spacings and fillet radii - are reported. For the two extreme infill configurations (30% and 100%), the crack front and the notching region are indicated in red (b), alongside a representative image of the frontal view of 30% sharp notch (in light-blue frame).

modulus from fracture tests, E_f/ρ_{app} , was studied, as reported in Figure 3.21. The results suggest a U-shaped trend at varying infill, with the minimum corresponding to intermediate configuration between 82% and 100% nominal infill configuration. Thus, while being characterized by significantly different specific moduli, the normalized fracture toughness values for 100% were perfectly equivalent to those coming from 47% and 65%. Indeed, the 30% infill structures (the only properly defined as cellular materials) proved to be even tougher, in specific terms, proving once more their capability for high-energy absorption, which makes highly-porous ACMs so interesting from both a scientific and industrial point of view.

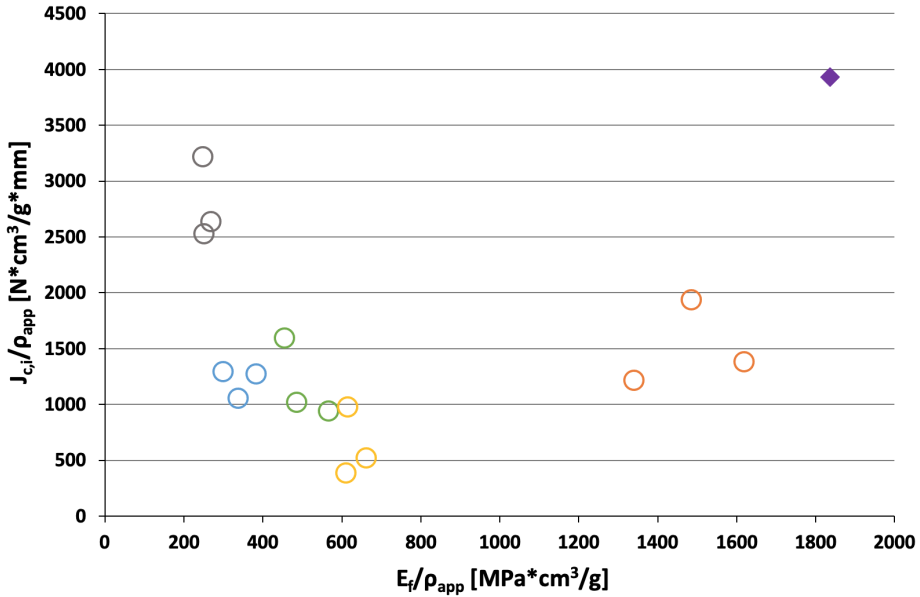


Figure 3.21: Series B - Blade Notch. Normalized Fracture Toughness at Initiation, $J_{c,i}/\rho_{app}$, vs Normalized Elastic Modulus from fracture tests, E_f/ρ_{app} , for specimens with varying infill level (30%, 47%, 65%, 82%, 100%). The *continuum* configuration is represented as limit case in cellular materials analysis (◆).

4 Trabecular bone tissues used as heterologous bone grafts

4.1 Trabecular bone: introduction and applications in regenerative medicine

Bone tissue is a complex and dynamic living tissue, which constantly undergoes a process called *remodeling*, consisting in both building of new bone tissue and breaking down of old bone tissue.¹ This process was demonstrated by observing the effect of applied strain on overall bone density, which resulted in massive decrease for minimum strains (*e.g.* in zero-gravity environment) and significant increase for high strains (*e.g.* in professional sports). Similar to many natural materials, the structure of bone tissue is highly hierarchical, as specific architectural features develop at differing length scales. The hierarchical structure of mammalian bone tissues covers numerous architectural levels, spanning from the individual collagen molecules and mineral platelets (nanoscale) to the whole bone (macroscale).²

¹G. J. Tortora, *Principles of Human Anatomy*, 12th (Wiley, 2010), 1056, ISBN: 9780470567050.

²Elizabeth A Zimmermann, Björn Busse, and Robert O Ritchie, “The fracture mechanics of human bone: influence of disease and treatment,” *BoneKEy Reports* 4 (2015): 743, <https://doi.org/10.1038/bonekey.2015.112>.

4. TRABECULAR BONE TISSUES USED AS HETEROLOGOUS BONE GRAFTS

The building blocks of bone tissues are the *lamellae*, which are constituted of fibers of collagen impregnated with hydroxyapatite crystals. At the mesoscale (100 μm), two different *lamellae* arrangements can be observed: the compact and dense cortical bone, and the porous and spongy trabecular bone. Cortical bone - where *lamellae* are regularly arranged into osteons - constitutes the surface of bones, even if it can extend deeper into bone tissue. At a first glance, it seems compact and dense, however it is quite porous, due to the abundant presence of microscopic spaces and canals. Cortical bone has the fundamental functions of support, protection and load bearing due to movement and weight. Conversely, trabecular bone consists of *lamellae* arranged in irregular patterns of thin struts called *trabeculae*. Trabecular bone has a far more porous structure - thus it is always protected by a layer of cortical bone - and it tends to be located in low or multidirectional stress areas. Its porous structure is ideal for lightweighting and for hosting, supporting and protecting the red marrow.

The number of bone defects caused by pathologies or traumas has constantly increased over time and is expected to grow even more in the upcoming decades.³ The restoration of such defects may need medical devices (bone grafts) to promote tissue regeneration, resulting in a raising interest in clinical practice.^{4,5,6} The porous structure of trabecular bone makes it an ideal environment to host and promote cell proliferation and differentiation. The use of autologous

³A. Odén et al., “Burden of high fracture probability worldwide: secular increases 2010–2040,” *Osteoporosis International* 26, no. 9 (2015): 2243–2248, ISSN: 14332965, <https://doi.org/10.1007/s00198-015-3154-6>.

⁴A Seth Greenwald et al., “Bone-graft substitutes: facts, fictions, and applications,” *Journal of Bone and Joint Surgery - Series A* 83-A, no. Supplement 2, Part 2 (2001): 98–103.

⁵Rusin Zhao et al., “Bone grafts and substitutes in dentistry: A review of current trends and developments,” *Molecules* 26, no. 10 (2021): 1–27, ISSN: 14203049, <https://doi.org/10.3390/molecules26103007>.

⁶Markus Rupp et al., “The clinical use of bone graft substitutes in orthopedic surgery in Germany—A 10-years survey from 2008 to 2018 of 1,090,167 surgical interventions,” *Journal of Biomedical Materials Research - Part B Applied Biomaterials* 110, no. 2 (2022): 350–357, ISSN: 15524981, <https://doi.org/10.1002/jbm.b.34911>.

4.I. Trabecular bone: introduction and applications in regenerative medicine

bone^{7,8,9} is still considered as the “gold standard”¹⁰ but its limitations in terms of availability and post-operative complications call for valid alternatives, among which heterologous bone (of mammalian origin) stands out.¹¹ Indeed, mammalian and human bones display strong similarities in terms of mineral content and trabecular structure^{12,13,14,15} Furthermore, non-human mammalian collagen - the main organic component of the extracellular bone matrix - shows a high degree (> 95%) of protein sequence identity with respect to hu-

⁷Jason A. Lowe et al., “Complications associated with negative pressure reaming for harvesting autologous bone graft: A case series,” *Journal of Orthopaedic Trauma* 24, no. 1 (2010): 46–52, ISSN: 08905339, <https://doi.org/10.1097/BOT.0bo13e31819c0ccb>.

⁸Rozalia Dimitriou et al., “Complications following autologous bone graft harvesting from the iliac crest and using the RIA: A systematic review,” *Injury* 42, no. SUPPL. 2 (2011): S3–S15, ISSN: 18790267, <https://doi.org/10.1016/j.injury.2011.06.015>.

⁹Ahmet Kinaci, Valentin Neuhaus, and David C. Ring, “Trends in bone graft use in the United States,” *Orthopedics* 37, no. 9 (2014): e783–e788, ISSN: 19382367, <https://doi.org/10.3928/01477447-20140825-54>.

¹⁰M. K. Sen and T. Miclau, “Autologous iliac crest bone graft: Should it still be the gold standard for treating nonunions?,” *Injury* 38, no. SUPPL. 1 (2007): 2–7, ISSN: 00201383, <https://doi.org/10.1016/j.injury.2007.02.012>.

¹¹Markus Rupp et al., “Bone transplantation or biomaterials?: An analysis of 99,863 surgical procedures in orthopedic and trauma surgery in Germany from 2018,” *Unfallchirurg* 124, no. 2 (2021): 146–152, ISSN: 01775537, <https://doi.org/10.1007/s00113-020-00861-z>.

¹²Jeroen Aerssens et al., “Interspecies differences in bone composition, density, and quality: Potential implications for in vivo bone research,” *Endocrinology* 139, no. 2 (1998): 663–670, ISSN: 00137227, <https://doi.org/10.1210/endo.139.2.5751>.

¹³S. Weiner and H. D. Wagner, “The material bone: Structure-mechanical function relations,” *Annual Review of Materials Science* 28, no. 1 (1998): 271–298, ISSN: 00846600, <https://doi.org/10.1146/annurev.matsci.28.1.271>.

¹⁴Rossella Bedini et al., “The use of microtomography in bone tissue and biomaterial three-dimensional analysis,” *Annali dell'Istituto Superiore di Sanita* 45, no. 2 (2009): 178–184, ISSN: 00212571.

¹⁵Adam D. Sylvester and Claire E. Terhune, “Trabecular mapping: Leveraging geometric morphometrics for analyses of trabecular structure,” *American Journal of Physical Anthropology* 163, no. 3 (2017): 553–569, ISSN: 10968644, <https://doi.org/10.1002/ajpa.23231>.

4. TRABECULAR BONE TISSUES USED AS HETEROLOGOUS BONE GRAFTS

man's.¹⁶ Such evidences make heterologous bone highly suitable for this application. Little is known about the mechanical behaviour of the bone tissues used in heterologous bone grafts, which are obtained by subjecting the origin bone tissues to specific treatments aimed at achieving the biological characteristics necessary for their implantation in patients. Whereas several studies have been carried out to examine their clinical performance,¹⁷ bioactivity¹⁸ and safety profile,¹⁹ a comprehensive study aimed at investigating their mechanical response is still lacking.

In this work, the mechanical and fracture behaviour of various cancellous bone tissues used for the manufacturing of heterologous bone grafts was investigated. The materials examined were supplied by Bioteck S.p.A. (Arcugnano, Vicenza, Italy), a company dealing with the research and production of tissue substitutes for regenerative medicine. They consisted of cancellous bone tissues taken from different equine bones, femur and humerus, which proved to be valid anatomic sites for harvesting.²⁰ They were subjected to a specific

¹⁶Nunzia Gallo et al., "An overview of the use of equine collagen as emerging material for biomedical applications," *Journal of Functional Biomaterials* 11, no. 4 (2020): 1–27, ISSN: 20794983, <https://doi.org/10.3390/jfb11040079>.

¹⁷José Luis Calvo-Guirado et al., "Biological response to porcine xenograft implants: An experimental study in rabbits," *Implant Dentistry* 21, no. 2 (2012): 112–117, ISSN: 10566163, <https://doi.org/10.1097/ID.ob013e3182425991>.

¹⁸Jung Sang Cho et al., "Preparation of a novel anorganic bovine bone xenograft with enhanced bioactivity and osteoconductivity," *Journal of Biomedical Materials Research - Part B Applied Biomaterials* 101 B, no. 5 (2013): 855–869, ISSN: 15524973, <https://doi.org/10.1002/jbm.b.32890>.

¹⁹Piotr Wychowanski et al., "Preliminary Clinical Data and the Comparison of the Safety and Efficacy of Autogenous Bone Grafts Versus Xenograft Implantations in Vertical Bone Deficiencies Before Dental Implant Installation," *Transplantation Proceedings* 52, no. 7 (2020): 2248–2251, ISSN: 18732623, <https://doi.org/10.1016/j.transproceed.2020.02.099>.

²⁰Raffaele Russo, Marco Maiotti, and Ettore Taverna, "Arthroscopic bone graft procedure combined with arthroscopic subscapularis augmentation (ASA) for recurrent anterior instability with glenoid bone defect: a cadaver study," *Journal of Experimental Orthopaedics* 5, no. 1 (2018), ISSN: 21971153, <https://doi.org/10.1186/s40634-018-0121-0>.

4.1. Trabecular bone: introduction and applications in regenerative medicine

Bioteck proprietary enzymatic-based treatment to achieve perfect biocompatibility and preserve both the mineral and collagen components in the native conformation, leading to improvement in *in-vivo* formation of new bone.²¹ The preservation of the collagenous part of the tissue cyan enhances bone regeneration and prevents the pronounced embrittlement typically associated to collagen removal and allows the tissue to be manufactured in 3D formats. The most commonly used techniques to achieve biocompatibility, based on thermal treatments, result in the removal of collagen, causing the embrittlement of the tissue that makes the material usable only in granular form in clinical practice. Equine collagen proves to be extremely valid in biomedical applications due to its high degree of sequence homology with respect to human's. Indeed, it prevents the risk of zoonosis transmission - which characterizes the most widely employed alternatives, bovine and porcine collagen - without causing any documented immune re-

²¹Danilo Di Stefano et al., "Bone Formation Following Sinus Augmentation with an Equine-Derived Bone Graft: A Retrospective Histologic and Histomorphometric Study with 36-Month Follow-up," *The International Journal of Oral & Maxillofacial Implants* 31, no. 2 (2016): 406-412, ISSN: 08822786, <https://doi.org/10.11607/jomi.4373>.

4. TRABECULAR BONE TISSUES USED AS HETEROLOGOUS BONE GRAFTS

action.²² Further, by comparing equine^{23, 24, 25, 26}) and human^{27, 28} cancellous bone tissues, it emerges that the mechanical properties of the two different types of tissue are similar.

Three different types of tissue were examined: two of these had the mineral content of the bones of origin, *i.e.* femur and humerus; the third tissue (femur) was markedly demineralized to obtain a tissue suitable for manufacturing grafts characterized by a high degree of flexibility. For each type, specimens with different geometries and, for some geometries, with different sizes, were supplied. The tissues analyzed have a trabecular structure, where struts and plates - mostly made of hydroxyapatite and collagen - form the edges and the faces (incomplete) of the cells. Such open-celled structure is intrinsically inhomogeneous and complex. A morphological analysis of the materials in the various specimens was carried out by means of optical microscopy techniques, and model structures to deal with

²²Gallo et al., "An overview of the use of equine collagen as emerging material for biomedical applications."

²³R. Hodgkinson and J. D. Currey, "Young's modulus, density and material properties in cancellous bone over a large density range," *Journal of Materials Science: Materials in Medicine* 3, no. 5 (September 1992): 377-381, ISSN: 1573-4838, <https://doi.org/10.1007/BF00705371>.

²⁴C. M. Les et al., "Estimation of material properties in the equine metacarpus with use of quantitative computed tomography," *Journal of Orthopaedic Research* 12, no. 6 (1994): 822-833, ISSN: 1554527X, <https://doi.org/10.1002/jor.1100120610>.

²⁵P. Devin Leahy et al., "Correlation of mechanical properties within the equine third metacarpal with trabecular bending and multi-density micro-computed tomography data," *Bone* 46, no. 4 (2010): 1108-1113, ISSN: 87563282, <https://doi.org/10.1016/j.bone.2010.01.366>.

²⁶Jennifer E Symons et al., "Mechanical and morphological properties of trabecular bone samples obtained from third that syndrome," *American journal of veterinary research* 73, no. 11 (2012).

²⁷Hodgkinson and Currey, "Young's modulus, density and material properties in cancellous bone over a large density range."

²⁸Benedikt Helgason et al., "Mathematical relationships between bone density and mechanical properties: A literature review," *Clinical Biomechanics* 23, no. 2 (2008): 135-146, ISSN: 02680033, <https://doi.org/10.1016/j.clinbiomech.2007.08.024>.

the systems' inherent anisotropy were defined to research possible relationships between the material structure (at a macroscopic level) and the observed mechanical response. The mechanical behaviour was studied by means of monotonic compression tests in quasi-static conditions. Special attention was paid to the analysis of the effects of specimen geometry and size, and, in some cases, to the effect of test loading direction. Where high levels of strain could be achieved without showing any clear sign of brittleness, but rather exhibiting plasticity, a more in-depth microstructural analysis was carried out to investigate the origin of this peculiar response. The deformation behaviour of some tissues was further studied by means of cyclic compression tests, which allowed to investigate the strain accumulation processes exhibited by the tissues. Flexural tests were carried out and the behaviour exhibited in bending tentatively compared to that showed under compression.

Fracture tests on tissues with unchanged mineral content and markedly demineralized were performed. Special attention was dedicated to all stages of testing and data elaboration method set-up. The fracture behaviour was studied by resorting to high-resolution images and morphological analyses of the structures, leading to the determination of the fracture toughness parameter. An innovative approach, based on the application of the Load Separation Criterion (LSC), was applied to the case of highly demineralized ductile-like tissues, aiming at the construction of the resistance R-curves.

4.2 Materials and methods

Materials

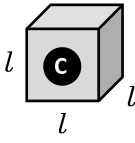
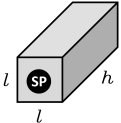
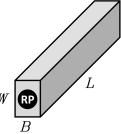
Three different types of cancellous bone tissue, indicated with F, H and FF, were examined. The tissues F and H were obtained from equine femur and humerus, respectively, by means of a proprietary enzymatic-based treatment (Zymo-Teck[®] process, Bioteck S.p.A., Arcugnano, Vicenza, Italy) aimed at the selective removal of antigens,

4. TRABECULAR BONE TISSUES USED AS HETEROLOGOUS BONE GRAFTS

preserving the collagen in its natural configuration. For F and H, the mineral content is left unchanged with respect to the tissue of origin. By contrast, the tissue FF was obtained from tissue F after a final demineralization treatment specifically aimed at promoting a pronounced reduction in the mineral content. This turns out in the enhancement of the mechanical compliance of the tissue, so that it can be easily deformed to fit even complex shapes at the recipient site. The resulting mineral content in FF was around the 10% of that in the tissue or origin (and of that in the F tissue), which was around 75%. These data, provided by the manufacturer, were confirmed by complementary laboratory analyses. With these analyses, the mineral content was determined after a demineralization in an aqueous solution of acetic acid (3% vol.), at room temperature. For each of the three tissues examined, a representative specimen (prism-shaped specimen with nominal dimensions 10x10x40 mm³) was immersed in 80 ml of solution and the specimen mass monitored over time (after 10 days of immersion the demineralization process could be considered completed). Each specimen was then rinsed in distilled water, and subsequently dried. From the mass lost, the mineral content of the specimen was calculated. The mineral content values obtained for F and H tissues are consistent with the scientific literature on cancellous bone.²⁹ For each type of tissue, specimens with different geometries - cubes (C), square-base prisms (SP) and rectangular-base prisms (RP) - and for C- and SP-types also with different sizes, were supplied after sterilization by beta-rays irradiation at 25 kGy. Geometries and sizes were chosen according to the mechanical testing program (see Section 4.2). The complete list of the specimens supplied, with their geometrical details, is reported in Table 4.1. It is worth underlining that the use of bone tissues properly treated by the manufacturer makes sample handling far easier with respect to tissues in the origin state as it prevents difficulties associated with conditioning procedures and

²⁹R. Bruce Martin et al., *Skeletal Tissue Mechanics*, Second Edi (New York: Springer Science+Business Media, 2015), 501, ISBN: 9781493930012, <https://doi.org/10.1007/978-1-4939-3002-9>.

Table 4.1: Geometries and dimensions of the specimens for the mechanical characterization. The values of the key dimensional parameters and the number of specimens supplied are reported for each material - F, FF and H - and geometry - cube (C), square prism (SP) and rectangular prism (RP). A chromatic convention, which is maintained throughout the whole work, is applied to the different types of bone tissue considered, according to which red, blue and green are assigned to F, FF and H, respectively.

Specimen Geometry		Type of Bone				
		F	FF	H		
Geometry	Label	Dimensions [mm]		#n Specimens		
	C	<i>l</i>				
	C _{l10}	10	20	20	20	
	C _{l15}	15	5	5	5	
	C _{l20}	20	5	5	5	
	C _{l25}	25	5	5	5	
	C _{l30}	30	5	5	5	
	SP	<i>l</i>	<i>h</i>			
	SP _{h20}	10	20	5	5	5
	SP _{h30}	10	30	5	5	5
	RP	<i>B</i>	<i>W</i>	<i>L</i>		
	RP _{L50}	5	10	50	5	5

avoids variability due to different degrees of cleaning^{30,31}

³⁰Cook and Zioupos, "The fracture toughness of cancellous bone."

³¹C. J. Hernandez et al., "Quantitative relationships between microdamage and cancellous bone strength and stiffness," *Bone* 66 (2014): 205–213, ISSN: 87563282, <https://doi.org/10.1016/j.bone.2014.05.023>.

Methods

Density measurement

For each specimen, the apparent density, ρ_{app} , was evaluated as the ratio between its own mass and volume. Mass data were measured by means of a digital analytical balance with 10^{-1} mg resolution. The volume was determined from the specimen dimensions, measured by means of either a digital micrometer (with 1 μ m resolution) or a Vernier caliper (with 50 μ m resolution), for lengths lower or higher than 20 mm, respectively. An "apparent" character is attributed to the density of the specimen in consideration of the porous nature of the material.

Morphology-based classification of the specimens for the mechanical characterization

With the aim of researching possible relationships between macroscopic structure and mechanical properties, the specimens were preliminarily classified according to a specifically developed morphology-based criterion.

Each specimen supplied was analyzed to identify the Main Porosity Development Directions, MPDDs, which represent the preferential orientations of the material porosity in the specimen. The MPDDs are regarded as the key parameter to describe the structure of each specimen's trabecular architecture. For the analysis of the morphology of the material (pore geometry, size and orientation), standard optical purple and digital microscopy techniques (Leica microscopes, models MS5 and DMS300) were used. Five different model structures (labeled 1Da, 1Db, 2Da, 2Db and 3D), defined on the basis of the MPDDs and their geometrical relation with the Specimen Principal Directions, SPDs, identified by the edges of the specimens which are coincident with the possible loading directions in the mechanical test, were taken as references. Figure 4.1 provides a prototypical example in which the method is applied to detect the 1D and 2D model structures: for

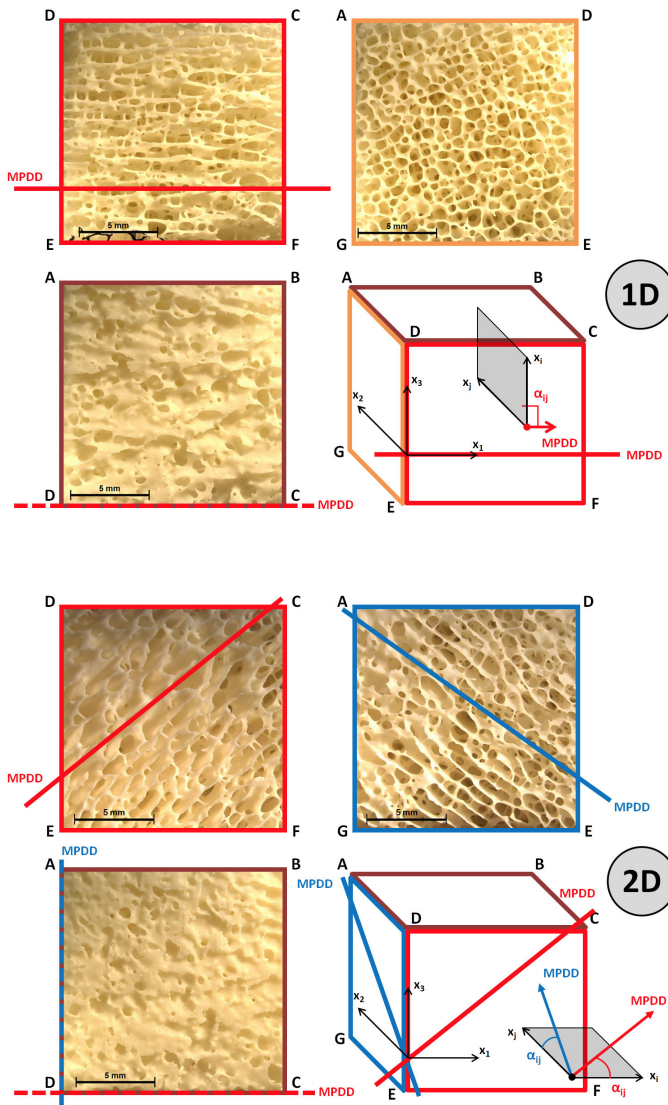


Figure 4.1: Representation of 1D- and 2D-type model structures detected on actual specimens (F tissue specimens belonging to the C_{115} series), with particular emphasis on the interrelation (given by α_{ij}) between the the Main Porosity Development Directions, MPDDs, and the generic plane representative of the Specimen Principal Directions, SPDs, identified by the directions (X_i, X_j).

4. TRABECULAR BONE TISSUES USED AS HETEROLOGOUS BONE GRAFTS

each specimen, microscopy analyses were carried out on the surface of the faces in order to study the interrelation of the MPDDs with the SPDs. The structure 1D is characterized by the existence of a single MPDD ($n_{\text{MPDD}} = 1$, where n_{MPDD} is the number of MPDDs detected), which can either satisfy or not the parallelism/orthogonality condition with respect to a generic plane defined by the SPDs and identified by the directions (X_i, X_j) , where (X_i, X_j) can be either (X_1, X_2) , (X_1, X_3) or (X_2, X_3) . The parallelism/orthogonality condition is considered fulfilled when the angle α_{ij} between the single MPDD (identified directly from the direction along which the pores appear oriented on the surface under analysis) and the generic plane (X_i, X_j) is either 0° or $90^\circ (\pm 3^\circ)$. If so, the structure is labelled with 1Da, otherwise it is labelled with 1Db. The structure 2D is characterized by the existence of two MPDDs ($n_{\text{MPDD}} = 2$), forming a plane on which the porosity is bi-oriented. The label 2Da is assigned to a specimen for which each of the two MPDDs is parallel/orthogonal to a generic plane (X_i, X_j) defined by the SPDs, after measuring the angle α_{ij} for each MPDD, and verifying that α_{ij} is either 0° or $90^\circ (\pm 3^\circ)$. If the parallelism/orthogonality condition is not fulfilled, the structure is given the label 2Db. The specimens for which the structure could not be classified as 1D or 2D (where no MPDD could be clearly detected due to multiple orientation of the pores) are labelled with 3D. Table 4.2 shows the criterion used for the definition of the five model structures. The approach here adopted is quite similar to that used by Cook and Zioupos³² as a means to take into account the intrinsic anisotropy of the materials examined. This approach is largely simpler with respect to the method based on the construction of a fabric tensor - via the "mean intercept length" or the "volume orientation" concepts (see, for example, the works by Odgaard et al.³³ and Zysset³⁴) - from both a

³²Cook and Zioupos, "The fracture toughness of cancellous bone."

³³A. Odgaard et al., "Fabric and Elastic Principal Directions of Cancellous," *Journal of biomechanics* 30, no. 5 (1997): 487-495.

³⁴Philippe K. Zysset, "A review of morphology-elasticity relationships in human trabecular bone: Theories and experiments," *Journal of Biomechanics* 36, no. 10

conceptual and an experimental point of view. The choice of a simpler approach is motivated by the fact that this study is not intended to develop a model suitable for predicting mechanical properties from morphological characteristics. This approach aims only at providing a classification of the specimens in such a way to verify the existence of a possible relationship between the porosity orientation and the mechanical response of the tissues. In connection with this, it is worth underlining that the specimens were harvested from the bones of origin without taking into account the different anatomic sites and their specific trabecular orientations. As a consequence, different porosity directions - which may be qualitatively related to the adaptive nature of bone in response to external mechanical loading³⁵ - may coexist within the same specimen, resulting in a MPDDs detection that was not always straightforward. However, in general, opposite faces of the same specimen exhibited the same main trabecular orientation, thus supporting the validity of the morphology-based criterion proposed.

Mechanical tests

Compression tests The quasi-static compression tests were performed by using an Instron test system (model 3366) equipped with a 10 kN load cell, in air, at room temperature. Both monotonic (one-way) and cyclic compression tests were carried out.

In the monotonic tests, the crosshead velocity was varied, depending on the specimen under analysis, in such a way to obtain an apparent (see below) compression strain rate of 0.05 min^{-1} - similar to that used by Chen and McKittrick³⁶ - in every test, irrespective of specimen size. A thin layer of paraffin oil was deposited on each

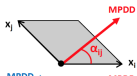
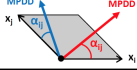
(2003): 1469–1485, ISSN: 00219290, [https://doi.org/10.1016/S0021-9290\(03\)00128-3](https://doi.org/10.1016/S0021-9290(03)00128-3).

³⁵Martin et al., *Skeletal Tissue Mechanics*.

³⁶Po Yu Chen and Joanna McKittrick, “Compressive mechanical properties of demineralized and deproteinized cancellous bone,” *Journal of the Mechanical Behavior of Biomedical Materials* 4, no. 7 (2011): 961–973, ISSN: 17516161, <https://doi.org/10.1016/j.jmbbm.2011.02.006>.

4. TRABECULAR BONE TISSUES USED AS HETEROLOGOUS BONE GRAFTS

Table 4.2: Definition of the model structures, as a combination of two parameters: 1) the number of Main Porosity Development Directions, n_{MPDD} ; 2) the angle, α_{ij} , formed by the MPDDs and the generic plane representative of the Specimen Principal Directions, SPDs (see caption of Figure 4.1 for further details). Specimens where no MPDD could be clearly detected are classified with 3D-label.

Model Structure			
n_{MPDD}	Model	Angle α_{ij}	
		$0^\circ; 90^\circ$	$\neq 0^\circ; 90^\circ$
1		1Da	1Db
2		2Da	2Db

compression plate in order to reduce the friction between the specimen and the plate. Tests were interrupted after failure for F and H specimens, at about 5% in apparent (see below) compression strain, while being continued up to 35% in the case of FF specimens.

For each tissue, the tests were performed in such a way to explore the following effects:

- "testing direction effect": the specimens belonging to the C_{l10} series (see Table 4.1) with structure of type 1Da (see Table 4.2 and Figure 4.1) were used; the loading direction was either orthogonal or parallel to the MPDD; a similar approach was followed by Cook and Zioupos.³⁷ For the tissue H only, a possible testing direction effect was researched on specimens belonging to the C_{l10} series with 2Da-type structure as well.
- "size effect": specimens belonging to the C series were used (see Table 4.1). Regarding the specimen size range examined: the smallest size (*i.e.* series C_{l10}) was selected to ensure that

³⁷Cook and Zioupos, "The fracture toughness of cancellous bone."

the key dimensional parameter of the specimen was at least 10 times the maximum pore dimension (see Section 4.3); the largest size (*i.e.* series C_{l30}) was the maximum size obtainable from the three bones of origin.

- "height effect": specimens belonging to the SP_{h20} and SP_{h30} series (see Table 4.1) were used. Specimens with height-to-width ratio up to 3 were tested. Higher ratios were not taken into consideration since preliminary tests pointed out that significant specimen distortions could occur during a test on specimen with height-to-width ratio higher than 3, thus preventing from the obtainment of reliable and comparable results.

It is worth underlining that only the smallest specimen size (C_{l10} series) was selected for the evaluation of the testing direction effect (1Da- and 2Da-type only) in order to minimize the probability for different trabecular orientations to manifest within the same sample.

For each specimen tested, the load, P , vs crosshead displacement, u , curve, output of the test, was converted into an "apparent" stress, σ_{app} , vs "apparent" strain, ϵ_{app} , curve. σ_{app} and ϵ_{app} are engineering quantities since determined from the initial dimensions of the specimens under examination: σ_{app} was calculated as the load over the initial cross section, ϵ_{app} as the crosshead displacement - properly corrected to remove the "foot zone" of the P vs u curve corresponding to the approaching and plate-specimen contact establishment phases - divided by the initial height of the specimen. Stress and strain have an "apparent" character because of the porous nature of the systems.

In the cyclic tests, carried out on F and FF tissues only, each cycle consisted of a loading phase, characterized by the same apparent compression strain rate used in the monotonic tests, followed by an unloading phase at 0.1 min^{-1} (Figure 4.2). The displacement reached at the end of the loading phase increased, over time, from cycle to cycle according to the scheme presented in Figure 4.2a. Load vs crosshead displacement curves were collected as output. For each tissue examined, four specimens belonging to the C_{l10} series were

4. TRABECULAR BONE TISSUES USED AS HETEROLOGOUS BONE GRAFTS

used. F specimens reached breakage during the test, whereas, for the FF specimens, the tests were interrupted at $\epsilon_{app} \approx 15\%$. The elaboration of the data involved the determination of the specimen initial compliance (Figure 4.2c) necessary for the "foot zone" correction procedure. For each cycle, the maximum apparent deformation applied, $\epsilon_{app,max,appl}$, the corresponding apparent stress, $\sigma_{app}@_{\epsilon_{app,max,appl}}$, and the residual apparent deformation after the unloading phase, $\epsilon_{app,res}$, which are regarded as the fundamental quantities for this kind of analysis, were determined as indicated in Figure 4.2b. In particular, $\epsilon_{app,res}$ was taken in correspondence of the last point of monotonic decrease on the unloading curve below the threshold value of $P^* = 0.5$ N, where the specimen is considered as fully unloaded. In order to investigate the possible effect of the procedure adopted for the determination of $\epsilon_{app,res}$, a different data elaboration scheme was also used. According to this second approach, $\epsilon_{app,res}$ was determined for each cycle by considering the point of reloading in the subsequent cycle (evaluated at the first point of monotonic increase), thus allowing longer recovery times.

Flexural tests The flexural tests, in three-point bending configuration, were performed by using the same Instron machine used for the compression tests, this time equipped with a 500 N load cell. The tests were carried out in air, at room temperature, on specimens belonging to the RP_{L50} series (see Table 4.1). The specimens were positioned flatwise on supports properly lubricated with paraffin oil and a distance between the supports (span, S) of 40 mm was used. Specimen dimensions (refer to Table 4.1) were chosen by taking into account several aspects: (i) longer specimens (with a higher L) were hardly obtainable from the tissue H, and consequently L was fixed at 50 mm to use the same size for the specimens of the three different tissues; (ii) to reach a compromise between the need for a small specimen thickness, B, to contain the shear contribution in the test, and the need for a significant difference between the values of specimen thickness and width (B and W, respectively) and the maximum pore

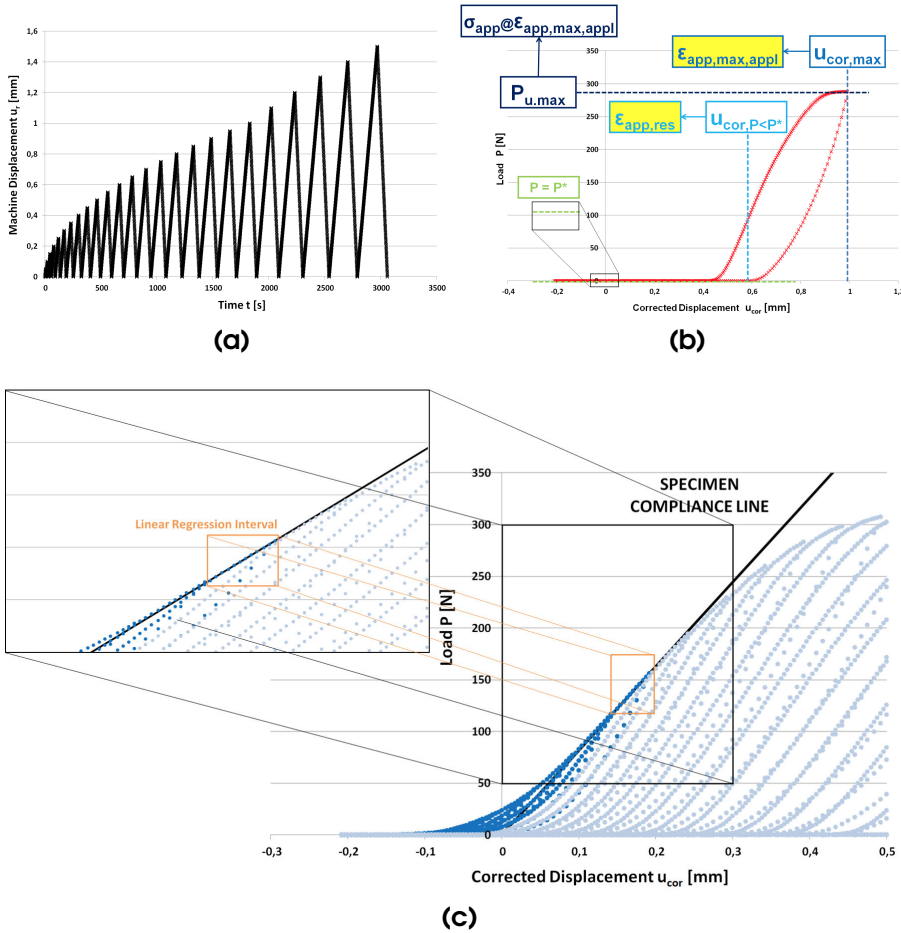


Figure 4.2: Cyclic tests. The test input consists in Machine Displacement, u_r , vs Time, t , plot (a). The output of the test is a series of cycles expressed in terms of Load, P , vs Corrected Displacement, u_{cor} , where u_{cor} is obtained by shifting the data on the displacement axis after the specimen compliance was calculated as the maximum slope of the initial linear region (c). The procedure for the determination of the maximum apparent deformation applied, $\epsilon_{app,max,appl}$, the corresponding stress, $\sigma_{app}@ \epsilon_{app,max,appl}$, and the residual apparent deformation after the unloading phase, $\epsilon_{app,res}$, is reported as well (b).

4. TRABECULAR BONE TISSUES USED AS HETEROLOGOUS BONE GRAFTS

dimension (see Section 4.3), W was set at 10 mm (that is the side length of the smallest cubes used for the compression tests) whereas B was reduced at $W/2$ (the resulting S/B ratio was 8). For data-processing, reference was made to the beam theory (for an elastic, homogeneous and isotropic material), neglecting the porous nature of the systems, but attributing an "apparent" character to the mechanical quantities involved in the description of the response of the materials. The load vs crosshead displacement curve, output of the test, was converted into an apparent stress vs apparent strain curve, with stress and strain determined in the outer fibers zone, at the specimen mid-length. The crosshead speed was chosen in such a way to obtain the same apparent strain rate of the compression tests (*i.e.* 0.05 min^{-1}). From the stress vs strain curve of each specimen examined, an apparent flexural modulus, $E_{\text{app},f}$, was determined.

Creep tests In order to study the possible contribution of viscoelastic effects on mechanical behaviour of trabecular bone, specific creep compression tests were performed on F and FF tissues. Specimens belonging to the C_{110} series (see Table 4.1) were selected, as smallest size was regarded to be the most suitable to minimize architectural and material (in terms of relative percentages of mineral and collagen, especially in FF). Measures of mass and volume were performed according to Section 4.2, in order to determine each specimen's apparent density, ρ_{app} . The activity was meant to study the effect of both apparent density and load applied on the response of the systems to static loads. More specifically, regarding the density effect, a fixed load was imposed (337 N for F tissue, 68 N for FF tissue) while spanning as much as possible in the apparent density of the specimens; conversely, regarding the load effect, specimens with almost the same ρ_{app} values were selected and then tested at significantly different load levels. In this final step, for each specimen, the load level chosen was determined as a percentage of the apparent stress at failure expected for its specific apparent density, by using the relationship obtained from monotonic one-way compression tests (Figure 4.8). The tests

were carried out at the Instron test system (model 3366), equipped with a 10 kN load cell, in air, at room temperature. A thin layer of paraffin oil was applied to the compression plates in order to reduce specimen-plate friction. The total time selected for creep testing was 3600 s, starting from load application, while acquisition time was set to 100 ms. The tests were designed in such a way to be composed of two different regimes: 1) the first regime, in displacement control characterized by fixed crosshead velocity (2 mm/min), up to the time t_0 , in correspondence of which the desired load level (either 337 N and 68 N for density effect, or the selected percentage of failure stress in load effect analysis) was reached; 2) the second regime, starting from t_0 - when a switch from displacement to load control was applied - up to the end of the test (3600 s), in load control, thus realizing the conditions of creep testing.

Fracture tests

Rectangular-base prism geometry was selected for the manufacturing of fracture test specimens. Tissues both with unchanged mineral content (F) and markedly demineralized (FF) were studied. The notching phase was performed according to the methodology developed and validated for polymer-based ACMs (see Section 3.2). Initial crack length to width, a_0/W , ratios belonging to the interval $0.45 \leq a_0/W \leq 0.55$ - according to classic FM theory³⁸ - were introduced by using the micrometer tool of the notching machine, with sacrificial PA6 bars used as process stabilizers. As already mentioned, the notches had to respect two fundamental requirements, consisting in the presence of a notch tip as sharp as possible, to mimic a natural crack in a component, and in the absence of damage ahead of the tip, due to the notch introduction process, that would undermine the structure, invalidating the results. Representative images of the notches for both F and FF tissues were reported in Figure 4.16*b*. Three-point bending tests on SE(B) specimens were performed on F and FF tissues. Span to width

³⁸Anderson, *Fracture Mechanics : Fundamentals and Applications*.

4. TRABECULAR BONE TISSUES USED AS HETEROLOGOUS BONE GRAFTS

ratio $S/W = 4$, according to classic FM theory on ductile polymers,³⁹ was used. Thus, being $B \times W \times L = 10 \times 20 \times 100 \text{ mm}^3$ the nominal specimen dimensions, span resulted of 80 mm. Five specimens for each tissue were tested. As already studied in the case of polymer-based ACMs, indentation effects occurring during fracture tests were supposed to be relevant, especially in the case of the highly-compliant FF tissue. Thus, proper correction tests were designed and performed. This is especially true considering that the approach used for ACMs, based on the research of regular patterns, could not be applied due to the heterogeneity of trabecular bone (stochastic foam). However, the underlying idea that supported the development of the method, consisting in the research of a parameter that could be representative of the structure in correspondence of the specimen-roll contact points, was maintained. More specifically, since the architecture itself could no longer fulfill the task, the local apparent density was selected as suitable parameter. Thus, after the execution of the tests, the terminal portions of each specimen, far from the notch, were carefully separated from the central region, using a hand-governed sharp blade, the same type hosted by the notching machine. The different regions all played a relevant yet peculiar role, serving to various purposes. The rectangular-base prism shaped terminal regions were measured in terms of mass and volume, so to obtain apparent density data (two for each fracture specimen). Those mass and volume data, if related to the corresponding values calculated for the entire specimen, allowed to obtain information about the central region, in terms of local density. The terminal regions were used to perform correction tests, as already did for polymer-based ACMs. Thus, lower rolls were positioned as close as possible each other, leading to a span $S \approx 0$ experimental configuration³⁹. Fracture and correction test configurations for SE(B) trabecular bone specimens were represented in Figure 4.3. Raw load vs displacement curves were recorded from both fracture and correction tests.

³⁹Moore, Williams, and Pavan, *Fracture mechanics testing methods for polymers, adhesives and composites*.

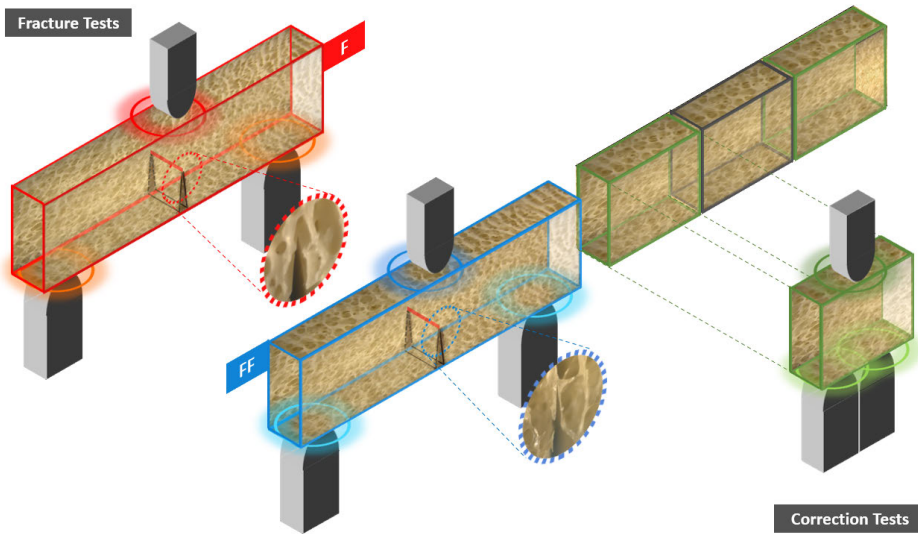


Figure 4.3: Fracture and correction test configuration for **F** and **FF** trabecular bone tissues. Magnified images of the crack tip are reported in dashed circular frameworks.

4.3 Results and Discussion

Morphology and density

Figure 4.4 shows the external surfaces of specimens of the three different bone tissues examined. It is important to point out that the images - collected by means of the microscope at the same magnification degree - can be considered as representative, for each tissue, of the material trabecular architecture that defines the porosity in terms of pore size and wall thickness, leaving the specific specimen structure - defined at Section 4.2 - out of consideration. At this degree of magnification, *i.e.* macroscopically, no pronounced difference appears in the morphological characteristics of the three tissues. FF tissue (Figure 4.4b) seems to be only slightly more porous than F (Figure 4.4a) and H (Figure 4.4c). Such small effect may be attributed to the demineralization process undergone by FF, that manifests itself

4. TRABECULAR BONE TISSUES USED AS HETEROLOGOUS BONE GRAFTS

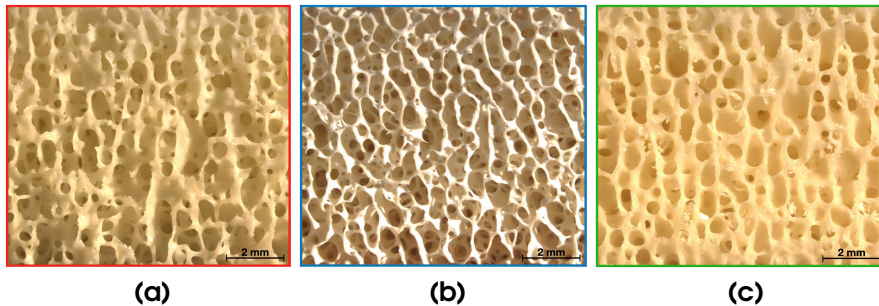


Figure 4.4: Images of representative external surfaces of (a) F, (b) FF and (c) H specimens.

in a small increase in pore size associated with a small decrease in wall thickness. However, the order of magnitude of 1 mm for the maximum pore size and 0.1 mm for the wall thickness - consistent with Cowin⁴⁰ and Martin et al.⁴¹ - can be considered as characteristic for all the systems under analysis. It has to be noted that a comprehensive study of the physical and morphological (at the micro-scale) characteristics of the bone tissues is being at present carried out by the authors.

The output of the morphology-based classification method applied to the specimens (see Section 4.2) is reported in Tables 4.3, 4.4 and 4.5, for F, FF and H tissues, respectively. For most of the specimens of F and FF tissues, one single MPDD aligned with a SPD - corresponding to 1Da-type structure (Table 4.2) - was noticed. By contrast, for H tissue, the number of specimens exhibiting one single MPDD (1D) was the same as that of the specimens with two MPDDs (2D). For H, MPDDs resulted aligned with the SPDs and only specimens classified as either 1Da or 2Da were obtained. Interestingly, for this tissue, only a few specimens exhibited a morphology that could be classified as

⁴⁰S. C. Cowin, "Wolff's Law of Trabecular Architecture at Remodeling Equilibrium," *Journal of Biomechanical Engineering* 108, no. 1 (February 1986): 83–88, ISSN: 0148-0731, <https://doi.org/10.1115/1.3138584>.

⁴¹Martin et al., *Skeletal Tissue Mechanics*.

3D, whereas for F and FF tissues the number of specimens with a 3D structure was much larger (at least fourfold). The more pronounced propensity of developing a bi-oriented porosity showed by the H tissue might be due to the different anatomical position, with respect to that of F and FF tissues, which might be responsible for a more marked confinement degree experienced by the bone tissue, thus preventing the development of the trabecular architecture in multiple directions (3D-type structure).

The apparent density data of the specimens are reported in Figure 4.5. The FF tissue is characterized by smaller density values in comparison to the ones of F and H. Such outcome may be due to the substantial differences in the mineral content, as well as to the slightly larger pore size and smaller wall thickness in the case of FF tissue compared to the non-demineralized F and H tissues. By considering the ρ_{app} mean values, H appears denser than F; however, by taking into account the standard deviation of the data, this difference is not statistically representative. For the three different tissues, the degree of dispersion of the ρ_{app} data around the mean value is included between the 20% and 30%.

Mechanical response in compression

Monotonic tests

The σ_{app} vs ε_{app} curves of the different tissues examined (F, FF, H), obtained from monotonic (one-way) compression tests carried out on specimens belonging to the C₁₁₀ series with structure of type 1Da, are reported in Figure 4.6. With the aim of exploring the "testing direction effect" (see section 4.2), for each tissue, part of the specimens was tested selecting the loading direction parallel to the specimen MPDDs, and part with the loading direction orthogonal to the MPDDs (see Tables 4.3-4.5). Darker and clearer curves refer to specimens tested in the former and in the latter manner, respectively.

Tissues F (Figure 4.6a) and H (Figure 4.6c) show a similar response, which appears remarkably different from that of tissue FF

4. TRABECULAR BONE TISSUES USED AS HETEROLOGOUS BONE GRAFTS

Table 4.3: F specimen population provided for the mechanical testing campaign. A specific symbol convention, which is maintained throughout the whole mechanical characterization, is used to gather and keep track of the information about specimen geometry, key dimensional parameters and model structure detected. Specimens of the C_{l10} series marked with \otimes and \odot are not used for the investigation of the testing direction effect on the mechanical response, since they do not satisfy the orthogonality condition between MPDD and SPD. However, the \odot -marked subset is used for the cyclic compression tests. A specific convention is adopted for the symbol edges: the yellow and grey border refers to specimens tested in a direction that is either orthogonal or parallel to a MPDD, respectively; on the contrary, non-outlined symbols stand for specimens where the above condition could not be met. The numbers indicated for each series represent the total population of specimen supplied as well as, more in detail, their amount for each structure type detected.



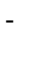


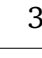





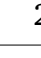


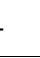


















































Specimen Geometry		Type of Bone					
		F					
Label	Total	Structure					
		1Da	1Db	2Da	2Db	3D	
C_{l10}	20	7 	1 	-	2 	4 	
		6 					
C_{l15}	5	2 	-	3 	-	-	
C	C_{l20}	5	2 	-	-	1 	2 
	C_{l25}	5	-	-	-	3 	2 
	C_{l30}	5	4 	-	-	-	1 
SP	SP_{h20}	5	4 	-	-	-	1 
	SP_{h30}	5	3 	-	-	1 	1 
RP	RP_{L50}	5	2 	-	-	-	-
		3 	-	-	-	-	

Table 4.4: FF specimen population provided for the mechanical testing campaign. See Table 4.3 for details. In addition: the specimen marked with \oplus is excluded from the analysis due to intrinsic shape defects that prevented from obtaining reliable results.

Specimen Geometry		Type of Bone				
		FF				
Label	Total	Structure				
		1Da	1Db	2Da	2Db	3D
C	C _{l10}	7 	-	1 	2 	2 
		6 	-	-	2 	-
	C _{l15}	1 	-	1 	1 	2 
	C _{l20}	1 	-	1 	2 	1 
	C _{l25}	-	-	-	2 	3 
C _{l30}	5	5 	-	-	-	-
SP	SP _{h20}	2 	-	-	1 	2 
	SP _{h30}	3 	-	1 	1 	-
RP	RP _{L50}	5	4 	-	-	1 

4. TRABECULAR BONE TISSUES USED AS HETEROLOGOUS BONE GRAFTS

Table 4.5: H specimen population provided for the mechanical testing campaign. See Table 4.3 for details.

Specimen Geometry		Type of Bone					
		H					
Label	Total	Structure					
		1Da	1Db	2Da	2Db	3D	
C _{l10}	20	5 	-	5 	-	1 	
		4 		5 			
C _{l15}	5	3 	-	2 	-	-	
C	C _{l20}	5	2 	-	3 	-	-
	C _{l25}	5	3 	-	2 	-	-
	C _{l30}	5	-	-	4 	-	1 
SP	SP _{h20}	5	1 	-	3 	-	1 
	SP _{h30}	5	3 	-	2 	-	-
RP	RP _{L50}	5	5 	-	-	-	-

(Figure 4.6b). The former tissues exhibit a brittle-like behaviour, with the σ_{app} vs ϵ_{app} curve showing an initial linear region, followed by a non-linear zone that generally precedes an abrupt stress drop associated with the failure of the specimen. The failure takes place at $\sigma_{app} = \sigma_{app,f}$, corresponding to a level of ϵ_{app} generally lower than 4%, and it can occur with the formation of scraps that rapidly abandon the specimen under testing. This is clearly visible in Figure 4.7, which shows deformed specimens after the compression test, for the three different bone tissues (one representative specimen for each tissue). On the F specimen, the regions generated by the separation of small

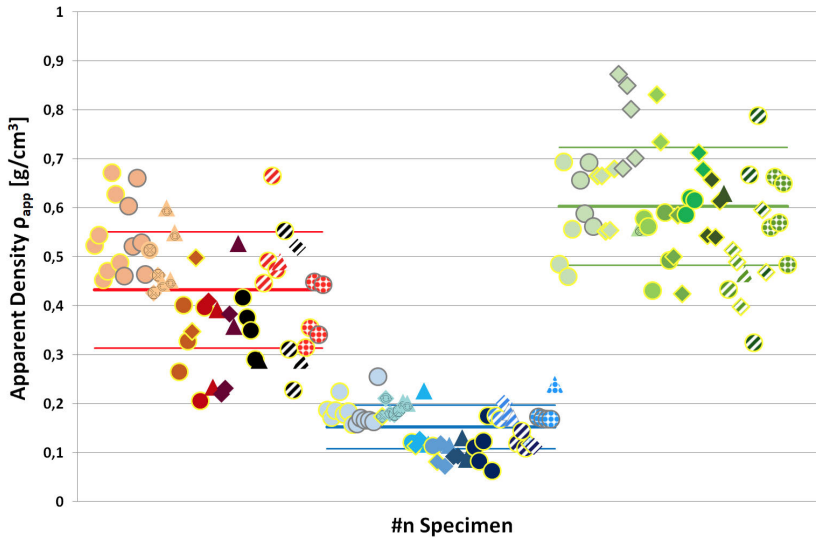


Figure 4.5: Apparent Density, ρ_{app} , of the bone tissue (F, FF, H) specimens under analysis (see Tables 4.3-4.5 for a complete recap of the symbol convention adopted). The thick coloured lines show the mean ρ_{app} value associated to each bone tissue, while the standard deviation band is represented by means of thin lines (with respect to the chromatic convention).

fragments of bone tissue, occurred at failure, can be clearly noticed; the H specimen, at failure, even split in two parts.

By contrast, the response of FF is characterized by the achievement of a relatively high level of ε_{app} (even ten times higher than the ε_{app} at failure showed by F and H specimens) without showing any sign of brittleness, at least at a macroscopic scale (Figure 4.7); interestingly, most of the applied deformation was not recovered after the load removal. A typical σ_{app} vs ε_{app} curve of a FF specimen shows an initial linear region, followed by a non-linear region that gives rise to a very broad peak preceding a zone generally characterized by irregular broad oscillations around a quasi-constant level of σ_{app} , extending up to the test interruption. The level of σ_{app} reached at the broad peak is taken as representative of the stress at failure of the specimen,

4. TRABECULAR BONE TISSUES USED AS HETEROLOGOUS BONE GRAFTS

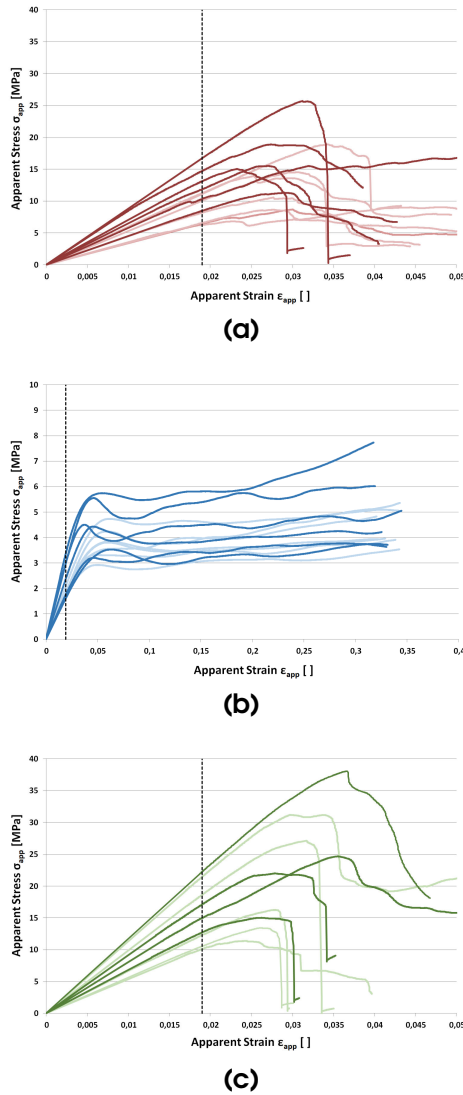


Figure 4.6: Apparent Stress, σ_{app} , vs Apparent Strain, ϵ_{app} , curves from compression tests on specimens belonging to the C_{l10} series with structure of type 1Da of (a) F, (b) FF and (c) H bone tissue. For each tissue, darker/clearer curves refer to specimens tested in parallel/orthogonally to their MPDDs, respectively. A vertical line at $\epsilon_{app} = 1.9\%$ (see text at Section 4.3) is represented as well.

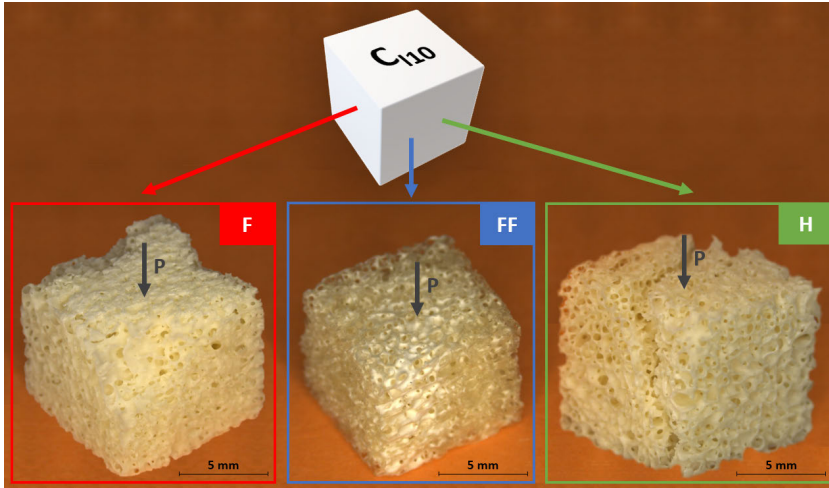


Figure 4.7: Failure patterns of **F**, **FF** and **H** C_{10} representative specimens from monotonic (one-way) compression tests.

and it is indicated with $\sigma_{app,f}$. At the macromechanical level, the FF specimens failure is quite similar to the one exhibited at yielding by a material with an elastic-plastic behaviour (see, for example, Khan and Huang⁴²). This suggests, with reference to FF, to talk about plasticity, whose specific characteristics are analyzed in the following. In this paper, the failure exhibited by FF specimens is referred to as a ductile-like failure. The levels of $\sigma_{app,f}$ of FF specimens can be even one order of magnitude lower than those of F and H specimens. The effect of the demineralization on the mechanical response of cancellous bone tissues was analyzed also by Chen and McKittrick,⁴³ on tissues from bovine femur. The effect they observed is qualitatively consistent with that noticed in the present paper for the equine femur bone tissues. A comparison between the values of stiffness and strength measured by Chen and McKittrick⁴³ and those measured here is presented below

⁴²Akhtar S. Khan and Sujian. Huang, *Continuum theory of plasticity* (Wiley, 1995), 421, ISBN: 978-0-471-31043-3.

⁴³Chen and McKittrick, “Compressive mechanical properties of demineralized and deproteinized cancellous bone.”

4. TRABECULAR BONE TISSUES USED AS HETEROLOGOUS BONE GRAFTS

Table 4.6: Mean values \pm standard deviation of Apparent Elastic Modulus, E_{app} , and Apparent Failure Stress, $\sigma_{app,f}$, from compression tests on C_{l10} specimens with 1Da only (F, FF) and 1Da/2Da (H) structure carried out with loading direction parallel (\parallel) and orthogonal (\perp) to the MPDDs.

Tissue	E_{app} [MPa]		$\sigma_{app,f}$ [MPa]	
	\parallel	\perp	\parallel	\perp
F	683 \pm 162	456 \pm 115	17 \pm 4.8	12 \pm 3.9
FF	132 \pm 39	96 \pm 6.7	4.5 \pm 1.0	3.8 \pm 0.6
H	1052 \pm 236	721 \pm 233	30 \pm 9.8	19 \pm 7.3

in this section.

From a comparative analysis of darker and clearer curves in Figure 4.6, it emerges that the testing direction (either parallel or orthogonal to the MPDDs) seems to produce only a weak effect on the σ_{app} vs ϵ_{app} curves. The data of stiffness (Young's modulus, E_{app} , see below) and strength (indicated with $\sigma_{app,f}$) measured along the two different testing directions are reported in Table 4.6 (mean values \pm standard deviation). It emerges that, for each type of bone tissue, the mean values of E_{app} and $\sigma_{app,f}$ measured along a direction parallel to the MPDD are higher than those measured along a direction orthogonal to the MPDD. Nevertheless, considering the standard deviations, these differences can not be considered statistically significant. For the H tissue only, also the data coming from the tests carried out on the 2Da-type specimens, tested along the two different directions, were taken into account.

For each type of tissue examined, the mechanical response exhibited under monotonic compression by the C_{l10} specimens with structure of 1Da (Figure 4.6) is representative of the response showed by any other specimen with a different geometry and/or structure (see Section 4.2 and Tables 4.3-4.5). A value of apparent elastic modulus, E_{app} , index of the mechanical stiffness of the material, was determined from the slope in the initial linear region of the σ_{app} vs ϵ_{app}

curve. Figure 4.8 shows a bi-logarithmic plot of E_{app} as a function of the apparent density, ρ_{app} , for all the specimens of the three tissues. The three series of data-points mix with each other, practically drawing one single linear trend. The fact that H and F data-points could result mixed with each other was expected, considering that the two tissues do not show significant differences in the morphological characteristics (at a macroscopic level) as well as in the mineral content. By contrast, the fact that FF data-points mix with those of the other two tissues was rather unexpected. This outcome seems to indicate that, after the demineralization treatment, the resulting material stiffness varies with ρ_{app} with the same law as in the non-demineralized tissue. At small strain levels, FF behaves as a less dense F. Interestingly, the stiffness of the bone tissues here examined is governed by the tissue density, with specimen geometry and material structure only playing a secondary role. More specifically, with reference to the specimen geometry and dimensions explored (see Section 4.2 and Tables 4.3-4.5), no evident "size" (for C specimens) or "height effect" (for SP specimens) is observed. For a given geometry, if specimens with different structures are considered, no clear influence of the structure is detected. Further, where different loading directions are analyzed, by considering the ρ_{app} -dependence of E_{app} , even the "testing direction effect" appears overshadowed.

Based on the scientific literature,⁴⁴ a linear trend in a bi-logarithmic chart was expected, and a power law best fitting curve was forced to the experimental data, without regard to tissue type, specimen geometry and structure, and loading direction. The fitting equation and the correlation coefficient of the regression are reported in Figure 4.8. E_{app} can be expressed as proportional to ρ_{app} raised to a power, n , of 1.86, which is included within the n -range expected for cancellous bone tissues ($n = 1 \div 3$), as predicted by the applications of the models developed to describe the elastic response of cellular solids⁴⁴. Rice, Cowin, and Bowman,⁴⁵ who worked on experimental

⁴⁴Gibson and Ashby, *Cellular solids: Structure and properties, second edition*.

⁴⁵J. C. Rice, S. C. Cowin, and J. A. Bowman, "On the dependence of the elasticity

4. TRABECULAR BONE TISSUES USED AS HETEROLOGOUS BONE GRAFTS

data, pointed out that, statistically, E_{app} is proportional to the square of ρ_{app} ($n = 2$) for cancellous bone. Such outcome is still well established in the scientific literature^{46, 47}. Even though the variation of ρ_{app} observed for each tissue examined is rather limited, a power law best fitting curve was forced to the experimental data-points of each tissue as well. n-Values of 1.80, 1.55 and 2.54 were obtained for F, H, and FF tissue, respectively. In spite of small differences, all these n-values are well included within the range expected for cancellous bone tissues^{48, 49, 50}.

Figure 4.9 shows the $\sigma_{app,f}$ data plotted as a function of ρ_{app} for all the specimens of the three different tissues, in a bi-logarithmic chart. The data-points of F and H tissues mix with each other, practically drawing one single linear trend, whereas FF data-points, still outlining a linear trend, keep separate from the others. This evident separation might be related to the two different failure types observed for the specimens of the F and H tissues on one side (brittle-like failure), and for the FF specimens (ductile-like failure) on the other. The results indicate that the material density governs not only the material stiffness, but also the material strength (here represented by $\sigma_{app,f}$). Specimen geometry and structure, and loading direction only play a secondary role. For the specimens of F and H with the highest density levels, with structure of type 1Db, 2Db or 3D, a possible contribution of

and strength of cancellous bone on apparent density,” *Journal of Biomechanics* 21, no. 2 (January 1988): 155–168, ISSN: 0021-9290, [https://doi.org/10.1016/0021-9290\(88\)90008-5](https://doi.org/10.1016/0021-9290(88)90008-5).

⁴⁶Yuehuei H. An and Robert A. Draughn, *Mechanical testing of bone and the bone-implant interface* (CRC Press, 2000), 624, ISBN: 9780849302664.

⁴⁷Martin et al., *Skeletal Tissue Mechanics*.

⁴⁸Dennis R. Carter and Wilson C. Hayes, “Bone Compressive Strength: The Influence of Density and Strain Rate,” *Science* 194, no. 4270 (December 1976): 1174–1176, ISSN: 00368075, <https://doi.org/10.1126/SCIENCE.996549>.

⁴⁹D. R. Carter and W. C. Hayes, “The compressive behavior of bone as a two-phase porous structure,” *Journal of Bone and Joint Surgery - Series A* 59, no. 7 (1977): 954–962, ISSN: 00219355, <https://doi.org/10.2106/0004623-197759070-00021>.

⁵⁰Hodgskinson and Currey, “Young’s modulus, density and material properties in cancellous bone over a large density range.”

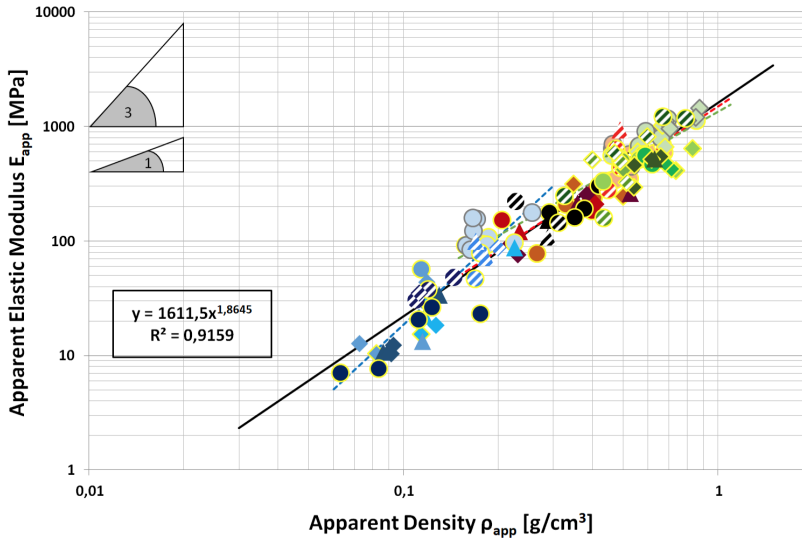


Figure 4.8: Apparent Elastic Modulus, E_{app} , vs Apparent Density, ρ_{app} , plot from monotonic (one-way) compression tests carried out on **F**, **FF** and **H** specimens (see Tables 4.3-4.5 for a complete recap of the symbol convention adopted). The black line represents the unique power law best fitting curve - whose equation and regression coefficient are reported as well - forced on all specimens, while the coloured dashed lines stand for the trends of the single bone tissues data-points.

shear on the materials strength could not be completely ruled out.⁵¹ For these structures, under compression, the loading direction was not aligned with the principal material direction and this could result in potential coupling with shear. No significant difference is noticed between the strength measured on structures of type 1Da or 2Da (loaded along a direction parallel/orthogonal to that of trabecular orientation) and the strength measured on structures of type 1Db, 2Db or 3D, as data points mix with each other. This seems to suggest that in the structures of the latter type, if shear contributed to the mechanical failure, its contribution remains overshadowed. Based on

⁵¹Gibson and Ashby, *Cellular solids: Structure and properties, second edition*.

4. TRABECULAR BONE TISSUES USED AS HETEROLOGOUS BONE GRAFTS

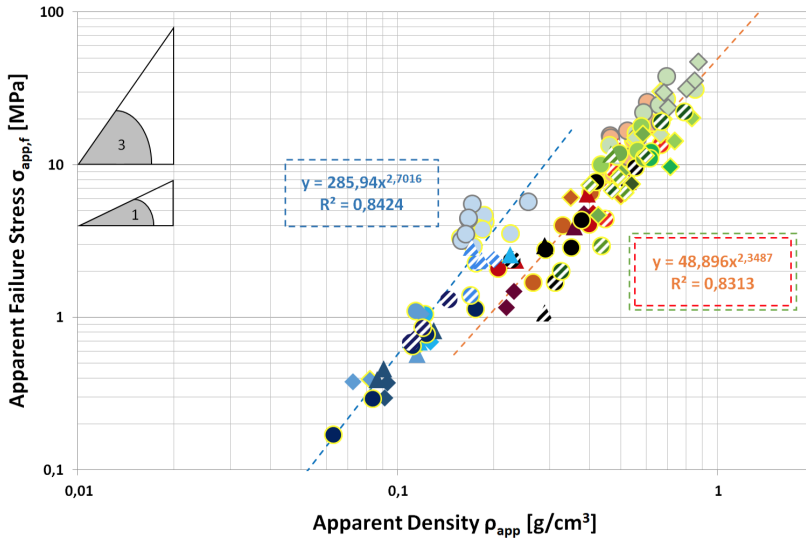


Figure 4.9: Apparent Failure Stress, $\sigma_{app,f}$, vs Apparent Density, ρ_{app} , plot from monotonic compression tests carried out on **F**, **FF** and **H** specimens (see Tables 4.3-4.5 for a complete recap of the symbol convention adopted). The blue dashed line represents the power law best fitting curve to FF data-points, while F and H are described by a unique trend (orange dashed line). The equation of the curves and the regression coefficients are reported as well.

the scientific literature⁵¹, a linear trend in a bi-logarithmic chart was expected for strength vs apparent density data. A power law best fitting curve was forced to the two different series of data (F and H data on one side and FF data on the other). The fitting equations and the correlation coefficients of the regressions are reported in Figure 4.9.

In Figure 4.10, the specific strength ($\sigma_{app,f}$ normalized over ρ_{app}) is plotted against the specific stiffness (E_{app} normalized over ρ_{app}). Interestingly, the data points, associated to different failure mechanisms (brittle- and ductile-like failure, for F/H and FF, respectively), draw a unique trend. The only exception is represented by the data

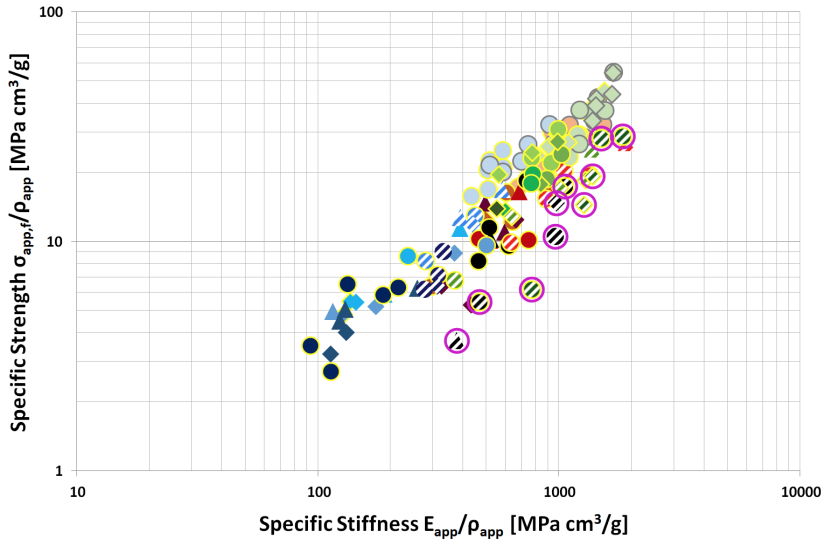


Figure 4.10: Specific Apparent Failure Stress (Specific Strength), $\sigma_{app,f}/\rho_{app}$, vs Specific Apparent Elastic Modulus (Specific Stiffness), E_{app}/ρ_{app} , plot from monotonic compression tests carried out on **F**, **FF** and **H** specimens (see Tables 4.3-4.5 for a complete recap of the symbol convention adopted). Data points referring to specimens with the highest height-to-width ratio (3:1) exhibiting a brittle-like failure (F, H) are outlined in **purple**.

points of F and H corresponding to specimens with the highest length (SP₃₀ series), which tend to keep separate from the others. The results, represented in this way, suggest that the use of specimens with a relatively high height-to-width ratio (3:1) leads to observe a decrease in the specific compression strength for cancellous bone tissues exhibiting a brittle-like failure.

A comparison of the values of stiffness and strength of the bone tissues here examined with those of other mammalian cancellous bone tissues (data from literature) can be of interest. Chen and McKittrick⁵² measured data of stiffness and strength on bovine femur bone

⁵²Chen and McKittrick, “Compressive mechanical properties of demineralized and deproteinized cancellous bone.”

4. TRABECULAR BONE TISSUES USED AS HETEROLOGOUS BONE GRAFTS

tissues, both demineralized and not. The fact that they used mechanical testing conditions very similar to those adopted in the present experimentation allows a direct comparison of the data (at given levels of density). For the density level corresponding to the average value measured for the specimens of the F tissue (Figure 4.5), stiffness and strength of the bovine tissue result of 690 MPa and 13 MPa, respectively, whereas they are 340 MPa and 7 MPa for the equine F tissue, respectively (data from fitting line equations). By comparing the data of stiffness measured after demineralization - and leaving apart the possible difference in the degrees of demineralization of the two tissues - the difference observed is strongly reduced: 66 MPa for the bovine against 48 MPa for the equine FF tissue (data from fitting line equations). A wide series of data of stiffness and strength of cancellous bone tissues collected from several literature papers, of bovine and human origin, is reported by Gibson and Ashby⁵³ in a graphical form. These data refer to trabecular bone tissues coming from different anatomical sites and tested in a variety of different conditions, including temperature, strain rate and environment. By comparing the values of stiffness and strength measured in the present work (for F, FF and H) with those reported by Gibson and Ashby⁵³, a good agreement is observed between the two sets of data. This outcome indicates that, at least from the mechanical point of view, the equine bone tissues here examined can be regarded as valid substitutes for the human cancellous bones. Hodgkinson and Currey⁵⁴ reported data of stiffness for bovine, equine and human cancellous bone tissues (non-demineralized). In this case, only an approximate comparison with the data measured on the equine bones tissues here examined can be done. Indeed, data from Hodgkinson and Currey⁵⁴ were measured under compression but using testing conditions significantly different from those adopted here - with reference to testing temperature and humidity. The stiffness measured for the F tissue

⁵³Gibson and Ashby, *Cellular solids: Structure and properties, second edition*.

⁵⁴Hodgkinson and Currey, "Young's modulus, density and material properties in cancellous bone over a large density range."

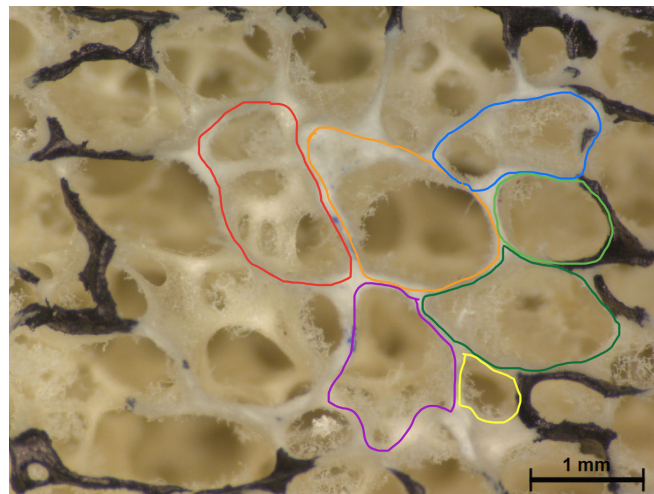
turns out to be smaller - to an extent that is 30%, 46% and 38% - than that measured on bovine, equine and human tissues, respectively.

In consideration of the peculiar response exhibited by the FF tissue under compression, which shows a sort of plasticity at the macromechanical level, its large deformation behaviour was further investigated by resorting to a more local approach. A FF specimen belonging to the C series (C_{I30} with 1Da-type structure) was selected and a nearly rectangular area (reference area) was marked in black on one of its lateral faces (parallel to the loading direction), as reported in Figure 4.11. A picture of the reference area, representative of the material in the undeformed state, was taken by means of the DMS 300 Leica microscope (Figure 4.11a). Then, the specimen was subjected to the compression test, following the usual testing procedure, and it was rapidly unloaded after reaching a level of $\varepsilon_{app} \approx 30\%$. Only a small part of the applied deformation was recovered after load removal. After 30 minutes, a second picture of the reference area, representative of the material in the permanent deformed state, was taken (Figure 4.11b). The borders of some cells were marked with a colored line to facilitate the comparison between the two pictures, from which the effects of the deformation history undergone by the specimen could be deduced. It emerges that the permanent character of the deformation observed at a macroscopic scale, which is at the basis of the apparent plasticity exhibited by FF tissue, is associated with a pronounced size variation of the cells accompanied by distortion of the cell borders. Localized breakage of single trabeculae can even occur, as it clearly emerges at the border between the orange- and blue-marked cells, where fracture seems to originate from a local defect in the cell wall.

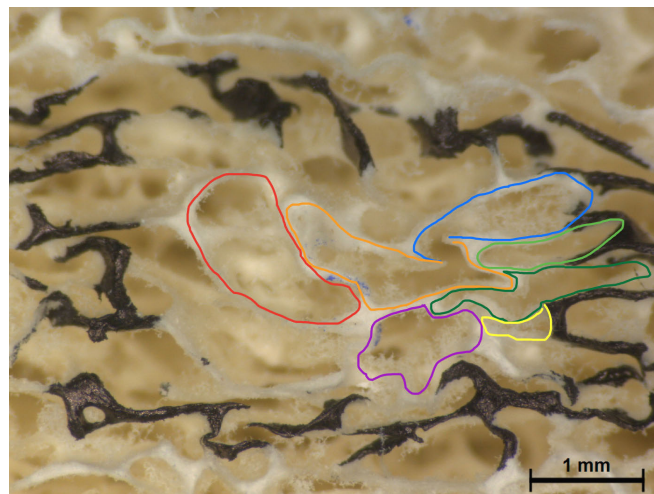
Cyclic tests

Figure 4.12 shows representative load vs displacement curves, with the displacement properly corrected for the curve "foot zone" (see Section 4.2), from compression cyclic tests carried out on a FF (Figure

4. TRABECULAR BONE TISSUES USED AS HETEROLOGOUS BONE GRAFTS



(a)



(b)

Figure 4.11: Pictures of the lateral face of a FF specimen in (a) the undeformed state (before a compression test) and in (b) the deformed state (30 minutes after the load removal). The specimen belongs to the C_{l30} series. A specific portion of the specimen - on which the attention is focused - is framed in black. Coloured outlines are used to highlight the cells of the bone tissue and to point out the changes in shape and size due to the test.

4.12a) and a F specimen (Figure 4.12b). FF and F clearly show a different response in terms of load and displacement levels achieved (F specimens exhibited breakage generally after no more than 15 cycles). In Figure 4.13 the residual apparent deformation recorded after the unloading phase of each specimen, $\varepsilon_{\text{app,res}}$, is plotted as a function of the maximum apparent deformation applied, $\varepsilon_{\text{app,max,appl}}$, in each cycle (see Section 4.2 for the data processing details). The apparent stress read at the maximum apparent deformation applied, $\sigma_{\text{app}}@_{\varepsilon_{\text{app,max,appl}}}$, is also plotted against $\varepsilon_{\text{app,max,appl}}$. The values of ρ_{app} of the various specimens are indicated in the figure.

A clear similarity emerges between the trend of a generic σ_{app} vs ε_{app} curve obtained from a monotonic (one-way) compression experiment (Figure 4.6) and the trend outlined in Figure 4.13 by the $\sigma_{\text{app}}@_{\varepsilon_{\text{app,max,appl}}}$ data plotted against $\varepsilon_{\text{app,max,appl}}$. For F specimens, a pronounced variability of the response with ρ_{app} can be clearly observed: the higher the density, the higher is the stress reached at a given level of $\varepsilon_{\text{app,max,appl}}$. A qualitatively similar observation also applies to FF, even though the effect of ρ_{app} is less pronounced, and it emerges less clearly due to the graph scale.

The analysis of the data coming from the cyclic tests is based on the idea that the $\varepsilon_{\text{app,max,appl}}$ applied to the specimen during a generic cycle can be seen as the sum of two contributions: a recoverable contribution, which is recovered at load removal, and a residual strain contribution, which is "stored" in the specimen and is represented by $\varepsilon_{\text{app,res}}$. In consideration of the viscoelastic nature of bone tissues (reported in relevant literature^{55,56,57}), a possible effect of the strain

⁵⁵T. M. Keaveny et al., "Biomechanics of trabecular bone," *Annual Review of Biomedical Engineering* 3 (2001): 307–333, ISSN: 15239829, <https://doi.org/10.1146/ANNUREV.BIOENG.3.1.307>.

⁵⁶R. M. Guedes, J. A. Simões, and J. L. Morais, "Viscoelastic behaviour and failure of bovine cancellous bone under constant strain rate," *Journal of Biomechanics* 39, no. 1 (2006): 49–60, ISSN: 00219290, <https://doi.org/10.1016/j.jbiomech.2004.11.005>.

⁵⁷Srinidhi Nagaraja, Mario D. Ball, and Robert E. Guldborg, "Time-dependent damage accumulation under stress relaxation testing of bovine trabecular bone,"

4. TRABECULAR BONE TISSUES USED AS HETEROLOGOUS BONE GRAFTS

history experienced by the material under investigation in an experiment aimed at separating the residual strain contribution from the recovered one should not be completely ruled out. Therefore, the results obtained in the cyclic experiments carried out in the present work should be related to the specific strain history experienced during the test. Further, taking into account that, for these materials, strain recovery is expected not to be an instantaneous event but a time-dependent process, a possible effect of the procedure adopted for the determination of the values of $\varepsilon_{app,res}$ cannot be excluded. In connection with this, the viscoelastic response of the bone tissues examined was addressed by means of creep compression tests - loading condition already explored in literature^{58,59} as discussed in the following.

From Figure 4.13 it emerges that FF and F data of $\varepsilon_{app,res}$ plotted against $\varepsilon_{app,max,appl}$ tend to overlap (with the only exception of the FF specimen with the highest ρ_{app}), practically drawing one single trend, with $\varepsilon_{app,res}$ equal to 0 if $\varepsilon_{app,max,appl}$ is less than $\approx 2\%$. Interestingly, no appreciable difference is observed in the response, at least up to F specimens breakage. These results seem to point out not only the negligible effect of tissue density on the $\varepsilon_{app,res}$ vs $\varepsilon_{app,max,appl}$ relationship, but also that the differences between FF and F do not produce any appreciable variation on the residual strain accumulation process, in a cyclic test with an increasing level of applied strain. By considering that FF and F differ slightly for the morphology (at least at a macroscopic scale), but largely for the mineral content, it

International Journal of Fatigue 29, no. 6 (2007): 1034–1038, ISSN: 01421123, <https://doi.org/10.1016/j.ijfatigue.2006.09.019>.

⁵⁸Ei Yamamoto et al., “Development of residual strains in human vertebral trabecular bone after prolonged static and cyclic loading at low load levels,” *Journal of Biomechanics* 39, no. 10 (2006): 1812–1818, ISSN: 00219290, <https://doi.org/10.1016/j.jbiomech.2005.05.017>.

⁵⁹Do Gyoon Kim et al., “Variability of tissue mineral density can determine physiological creep of human vertebral cancellous bone,” *Journal of Biomechanics* 44, no. 9 (2011): 1660–1665, ISSN: 00219290, <https://doi.org/10.1016/j.jbiomech.2011.03.025>.

is reasonable to think that the mineral part of the material does not control the residual strain accumulation process in this kind of tests. Interestingly, the strain storage process, which should be in charge of the collagenous part, seems to be unaffected by the weight fraction of collagen in the bone tissue. The ability of F tissue to accumulate unrecoverable strain before the specimen brittle breakage seems to indicate that the term plasticity could be used in its own right with reference to this brittle-like tissue as well. This observation is in general agreement with the scientific literature (see for example Ritchie, Buehler, and Hansma⁶⁰ and Cook and Zioupos⁶¹) which, with reference to non-demineralized cancellous bone tissues, ascribes the elastic-plastic behaviour exhibited by the tissue at the macromechanical level to the cellular structure of the material, whose trabeculae are, by contrast, made of perfectly brittle material. By means of a computer-based extrapolation procedure, the value of $\epsilon_{\text{app,max,appl}}$ at which a residual deformation starts accumulating, indicated with $\epsilon_{\text{app,max,appl,i}}$, was determined for each specimen tested. From the values of $\epsilon_{\text{app,max,appl,i}}$ obtained for the various specimens, irrespective of the tissue type, an average value was calculated and resulted of $(1.9 \pm 0.43)\%$.

By resorting to a different procedure for the determination of $\epsilon_{\text{app,res}}$ (see Section 4.2), in which the residual deformation was calculated from the loading phase curve of the cycle subsequent to the one under examination, different (smaller) levels of $\epsilon_{\text{app,res}}$ were obtained (the maximum difference between the data of $\epsilon_{\text{app,res}}$ determined with the two different data elaboration schemes is $\approx 10\%$). This is the proof of the ability of the materials under investigation to exhibit a gradual strain recovery over time after specimen unloading. Interestingly, even if slightly different data of $\epsilon_{\text{app,res}}$ were determined from the application of this second procedure, the value of $\epsilon_{\text{app,max,appl,i}}$ re-

⁶⁰Robert O. Ritchie, Markus J. Buehler, and Paul Hansma, "Plasticity and toughness in bone," *Physics Today* 62, no. 6 (2009): 41–47, ISSN: 00319228, <https://doi.org/10.1063/1.3156332>.

⁶¹Cook and Zioupos, "The fracture toughness of cancellous bone."

4. TRABECULAR BONE TISSUES USED AS HETEROLOGOUS BONE GRAFTS

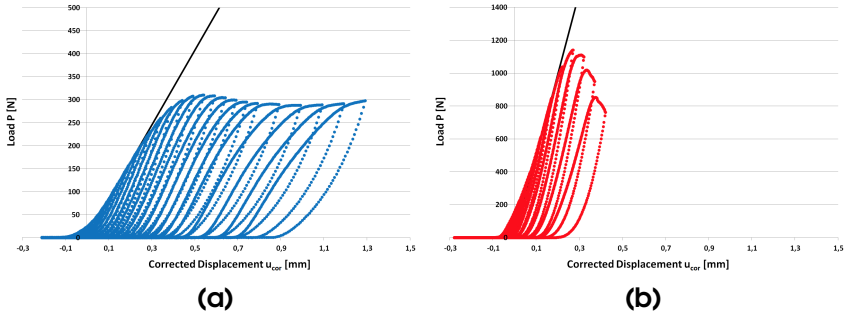


Figure 4.12: Output loading curves from cyclic compression tests performed on (a) FF and (b) F specimens belonging to the C_{l10} series. The specimen compliance lines are represented in black (see Figure 4.2c).

sulted unchanged by considering the standard deviation of the data, thus suggesting that this parameter might result independent of the time allowed for strain recovery.

The ρ_{app} -dependence of the stress at which residual deformation starts accumulating in the monotonic (one-way) compression tests was also investigated. $\epsilon_{app,max,appl,i}$ was assumed to be independent of specimen geometry and structure, and loading direction, and the stress value corresponding to $\epsilon_{app} = 1.9\%$ (which is the average value of $\epsilon_{app,max,appl,i}$) was read on the σ_{app} vs ϵ_{app} of each specimen (Figure 4.6). These stress data were then represented as a function of the specimen ρ_{app} in a bi-logarithmic chart (graph not showed) and it was observed that F and FF data points mixed with each other to draw a trend that could be considered linear, and a power law best fitting curve was forced to all the experimental data. A value of $n = 1.88$ was obtained. The fact that the data-points drew a single linear trend, with a n -value quite close to that of the power law expression obtained for the E_{app} data plotted as a function of ρ_{app} , was expected by considering that the level of ϵ_{app} at which residual deformation starts accumulating is quite close to, or even within, the initial linear region of the σ_{app} vs ϵ_{app} curve (Figure 4.6).

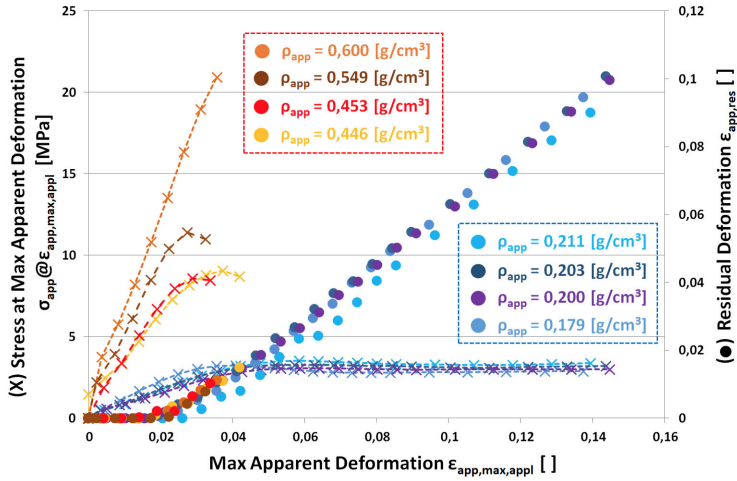


Figure 4.13: Stress at Maximum Apparent Deformation, $\sigma_{app}@ \varepsilon_{app,max,appl}$, (X) on the left axis, and Residual Deformation, ε_{res} , (•) on the right axis, as a function of the Maximum Apparent Deformation, $\varepsilon_{app,max,appl}$, plots from the cyclic compression tests carried out on four different specimens of F and FF tissues. The values of the ρ_{app} of the various specimens are also indicated.

Creep tests

The aim in the use of the first displacement-controlled regime during creep tests was twofold: 1) the evaluation of the apparent elastic modulus of the systems, so to perform a comparison with the data coming from monotonic one-way compressions (Figure 4.8), which led to consistent results; 2) to reach the conditions of load-controlled creep tests in the gentlest way possible, not to induce undesired load peaks that would have caused damage or failure of the systems due to overloading (and not due to creep). Raw load vs displacement curves were recorded and elaborated, in order to isolate the effective creep test region ($t \geq t_0$). The results were expressed in terms of creep deformation, ε_{app} , vs creep time, t^* , as reported in Figure 4.14. Referring to the applied load effect (Figure 4.14a and, magnified, 4.14b), it is clearly visible that F and FF tissue behave in a

4. TRABECULAR BONE TISSUES USED AS HETEROLOGOUS BONE GRAFTS

significantly different way. Very low creep deformation were induced in all F specimens, leading to almost flat curves that only differ by their onset value, and suggesting that even a relevant load variation results in low effects in specimens with almost the same ρ_{app} values. Conversely, as different percentages of the theoretical failure stress predicted from experimental compression data (Figure 4.9) were selected, FF tissue showed broad variations in creep response: interestingly, in addition to low and high creep deformation trends, a curve with intermediate behaviour was recorded, suggesting the presence of a gentle transition in terms of creep response between the two extreme configurations. Referring to the apparent density effect (Figure 4.14c and, magnified, 4.14d), no variations in FF specimens response could be detected, as low, intermediate and high ε_{app} trends were observed. However, concerning F tissue, alongside the almost flat creep curves already observed, the specimens with lower density presented a different behaviour: 1) significant increase in ε_{app} values were recorded after onset (non-null slope of the curve); 2) as creep deformation reached critical values, that could not be accommodated any longer, complete failure of the structures was induced. This is an extremely interesting result, as it points out the possibility for failure of trabecular bone architecture under static loads - in correspondence of critical levels of creep deformation. This mechanism is inherently different from failure due to overloading, which was observed in the case of either too small ρ_{app} specimens or excessively high load levels, where specimens failed during the first loading regime, in displacement control, before even reaching creep test conditions. As static loads turned out to be a potential undermining cause of the systems' structural integrity, more in-depth studies would be required to assess the underlying mechanisms. More specifically, while apparent density seems not to completely control the response of the systems, the local architectural and material characteristics of the structures are regarded to play a crucial role in it. Further, the study of fatigue in dynamic load conditions could be useful to broaden the *spectrum* and deepen the comprehension of trabecular bone mechanical response.

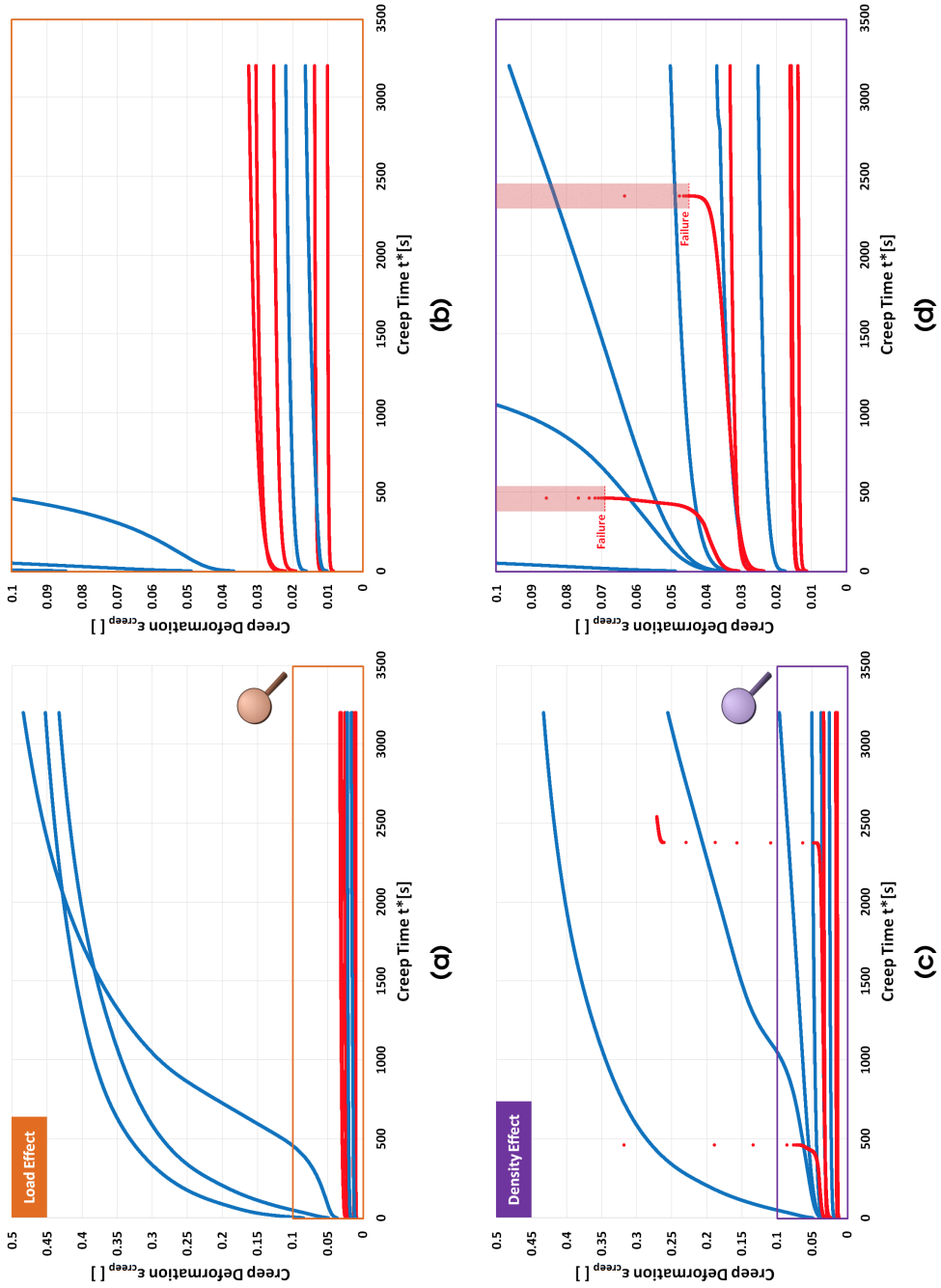


Figure 4.14

Figure 4.14: Creep tests on trabecular **F** and **FF** trabecular bone tissues: effect of (a-b) load level applied and (c-d) apparent density of the systems on the creep deformation, ϵ_{app} vs creep time t^* curves.

Mechanical response in bending

Figure 4.15 shows the $E_{app,f}$ data plotted as a function of ρ_{app} for all the RP specimens of the three different tissues examined, in a bi-logarithmic chart. It can be observed that the fifteen data-points tend to draw one single linear trend. Following what was done for the compression stiffness, E_{app} , data (see Section 4.3), a power law best fitting curve was forced to the experimental data without regard to tissue type and specimen structure (fitting equation and correlation coefficient of the regression are reported in Figure 4.15). The exponent, n , of the power law expression ($n = 2.08$) is not significantly different from the exponent of the E_{app} vs ρ_{app} power law fitting curve ($n = 1.86$), also traced in Figure 4.15 as a dashed black line. Even though all the data-points of $E_{app,f}$ keep above the E_{app} vs ρ_{app} fitting line, the difference between $E_{app,f}$ and E_{app} at a given level of ρ_{app} is very small, especially by taking into account the scattering observed for E_{app} vs ρ_{app} data-points (see Figure 4.8), reported as black dots in Figure 4.15. This seems to indicate that the mechanical stiffness is the same in tension and compression. Further, in the case of the tissues presenting a brittle-like failure (F and H), the relationship between the flexural stress at failure and the apparent density was studied as well. The data-points obtained perfectly overlap on those from compression tests (graph not showed). Thus, for F and H, and also for FF with reference to the stiffness, no significant difference is observed in the mechanical response in the two test configurations. These are interesting results by considering that: (i) in a bending test on a cellular material the stress state experienced by the material is expected to be particularly complex; (ii) the specimen used in the flexural tests carried out in the present work was not slender (see Section 4.2).

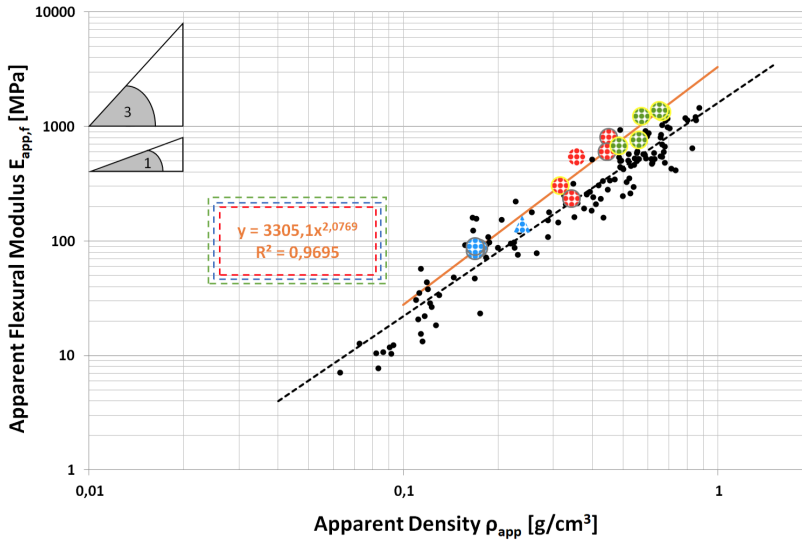


Figure 4.15: Apparent Flexural Modulus, $E_{app,f}$, vs Apparent Density, ρ_{app} , plot from bending tests carried out on **F**, **FF** and **H** RP_{L50} specimens (see Tables 4.3-4.5 for a complete recap of the symbol convention adopted). The orange line represents the unique power law best fitting curve - whose equation and regression coefficient are reported as well - forced on all RP_{L50} specimens. The black dashed line is the E_{app} vs ρ_{app} power-law best fitting curve forced on all the data-points (black dots) coming from monotonic (one-way) compression tests (see Figure 4.8).

Fracture response

Morphology of the structures

The heterogeneity of trabecular bone tissues – characteristic of stochastic foams – required each specimen to be analyzed independently from the others. In addition, differently from the case of ACMs, no regular patterns could be detected, meaning that even within the same specimen, special care had to be reserved in dealing with architecture. Thus, a proper way to keep track of all the information had to be developed. The method consisted in focusing the attention on the

4. TRABECULAR BONE TISSUES USED AS HETEROLOGOUS BONE GRAFTS

central portion of each F and FF specimen, corresponding to the region where notch would have been introduced (Figure 4.16a). Then, all four external surfaces (two bases and two sides) were observed at the optical microscope, and the corresponding images taken, resulting in complete mapping of the structure as produced, at the most external level (Figure 4.16b). As the notches had to respect the fundamental requirements of tip sharpness and no damage induction ahead of it, the natural evolution of the structure monitoring method was then to perform image acquisition of notched specimens, the same way already applied in the as produced configuration. The same positioning was used - by means of a paper mask specifically prepared - and the magnification remained the same as well, to obtain perfectly comparable pictures, representing exactly the same region of the specimen. This way, the check of preliminary requirements could be performed: images pointed out that notches were successfully introduced, presenting adequate sharpness not only for fragile F tissue, but also in the case of the highly-compliant FF tissue, where such accuracy wasn't taken *a-priori* for granted. Further, an accurate inspection of the external structure of the specimens allowed to state that notch introduction did not cause damage in the region ahead of crack tip, as surrounding *trabeculae* and cells turned out to be untouched. Finally, after fracture tests were performed, the specimens in their final configuration - either completely divided in two portions (F) or extensively deformed but still holding themselves (FF) - were once again observed at the optical microscope. The same rigorous attention to positioning and magnification was maintained. In the case of brittle F tissue, it was even possible to reconstruct the crack path, by simply carefully pulling over the two separate portions of specimen. This way, the brittle nature of fracture was even more evident, as broken *trabeculae* were not accompanied by extensive damage, deformation and cell shape and size distortion. The entire method is portrayed in Figure 4.16, for the representative case of F tissue. It is important to point out that the visual analysis could be performed only at the surface level. The systematic use of more sophisticated tech-

niques - like (micro-)CT, recurrently used in literature - that could provide information about the internal structure of the specimens, were disregarded at this initial stage. Indeed, CT-scans on representative specimens were carried out 1) to assess whether damage in the notched specimens was induced or not; 2) to perform a qualitative analysis of the structures (see below), especially in terms of crack front. The difficulties in the correct individuation of low-mineral areas in the demineralized tissue suggested their use in the description of the structure as crack initiated and propagated and of the damage phenomena, to be questionable. Thus, the CT-scanning procedure was not applied to all specimens used in the fracture characterization. Finally, as the most critical buckling conditions during scalpel-sliding notching process were supposed to be experienced at the surface, the absence of damage at the external level suggested that the same could be valid throughout the specimen thickness, where stress conditions were milder. CT-scans on representative specimens confirmed this point, as no damage induced by notching was observed.

Despite the key role attributed to the structure imaging activity, at the external level, the problem of internal architecture of cellular materials was still unsolved. In the case of polymer-based ACMs, the inherent architectural regularity imposed *a-priori* in the design phase, by controlling infill level and filament deposition angles, suggested the possibility to successfully build up 3D CAD models using dimensional measurements taken on actual specimens. Conversely, the stochastic foam nature of trabecular bone - intrinsically heterogeneous in terms of cell size, shape and strut thickness - required different techniques to be used to deal with it. More specifically, a representative specimen for F and FF tissues was dedicated to in-depth imaging analyses, being subjected to CT scans. The activity was carried out in collaboration with Fabbrica d'Armi Pietro Beretta (Gardone Val Trompia, Brescia, Italy). It is worth pointing out the qualitative nature of such activity, as the X-ray effect on preliminary treated trabecular bone of heterologous origin was not *a-priori* known, due to the industrial nature of the systems and especially in the case of the

4. TRABECULAR BONE TISSUES USED AS HETEROLOGOUS BONE GRAFTS

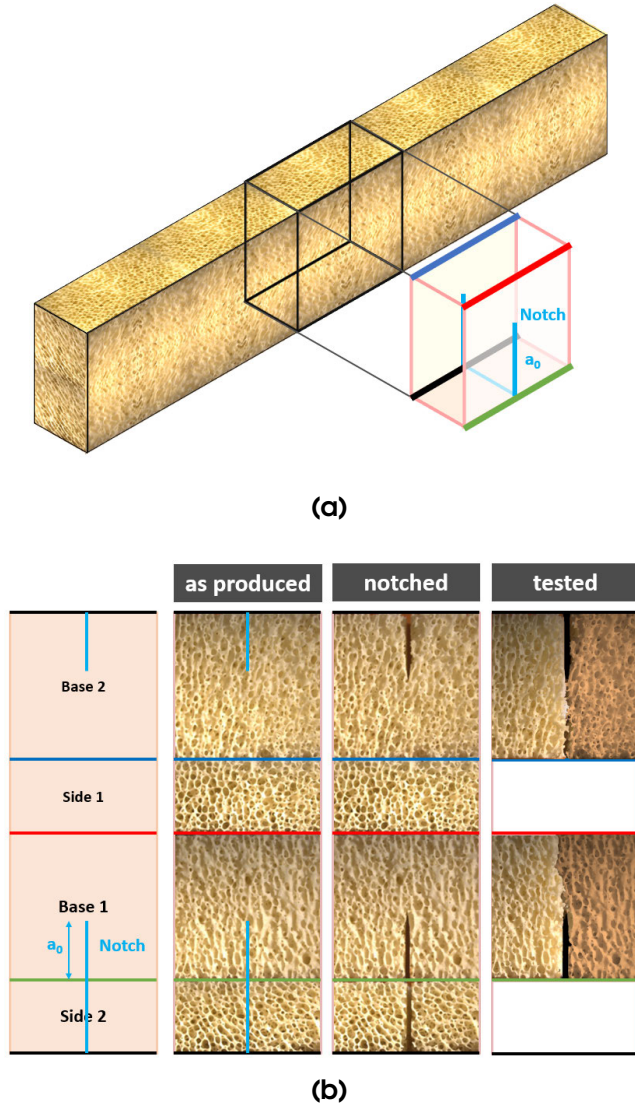


Figure 4.16: Optical microscopy morphological analyses of the surfaces: (a) identification of the notch region and development of the structure-tracking method; (b) structure monitoring from as-produced to after-notching and after-testing stages, for a representative **F** specimen.

highly-demineralized FF tissue. Scouting CT-scans were meant to assess the applicability of the technique, by observing potential damage induced, and to eventually lay the foundations for the development of a solid testing and data interpretation method, if applicable. Thus, the output coming from the analyses were not used as quantitative parameters, but rather as qualitative information about the nature of the systems.

The specimens were preliminarily measured and observed at the optical microscope in the region of interest, before undergoing the notching phase, carried out as previously exposed. After checking the adequate sharpness of the notches, as well as that no damage ahead of the crack tip was produced, the samples were ready for the scanning. The output of the CT activity consisted in a 3D model of the systems in the region of interest where notches were manufactured. By operating on this model with section planes orthogonal to the prism surfaces, relevant information about the internal structure of both F and FF tissue specimens could be deduced (Figure 4.17). The blue-outlined images represent sections taken using a plane orthogonal to crack plane, so that the notch V-shape could be observed. By sweeping the plane along the specimen thickness, some information about notch sharpness and the nature of crack tip - which may intercept *trabeculae* or not, depending on the specific position considered - could be deduced. By considering another section plan - once again orthogonal to crack plane but also to the blue one - the green-outlined regions were obtained. By sweeping along cutting direction, structural variations in the stochastic-foam-like architecture were examined, as the separation between notch lateral surfaces was progressively lowering, up to the notch tip configuration. The knowledge of the structure in correspondence of crack tip and in the surrounding area (volume) ahead of is fundamental, since local architecture was regarded as the crucial parameter governing fracture resistance and propagation, in addition to the trabecular material composition itself. Finally, the section plane containing the crack, located in correspondence of notch position, was considered (red-outlined region). For

4. TRABECULAR BONE TISSUES USED AS HETEROLOGOUS BONE GRAFTS

bot F and FF, it provided crucial information about the discontinuous nature of crack front, which obviously strongly depends on apparent density but also on the specific region of interest within the specimen, individuated by notch position and initial crack length. In general, by considering different areas in F and FF specimen, it can be stated that FF is characterized by a more discontinuous - referring to a higher 1D total linear length of void regions - crack front, in comparison to F, due to its inherent higher degree of porosity (and lower mineral). However, some regions of higher porosity F and lower porosity FF were observed, leading to extremely similar results in terms of nature of crack front. Thus, some final considerations were sorted out: 1) at fixed kind of tissue, each specimen was confirmed to be unique, meaning that the application of multi-specimen approaches would be incorrect from a fundamental point of view, and likely to provide wrong outputs; 2) even within the same sample, different regions presented varying architectures, orientations and degree of porosity, meaning that the results have always to be related with the systems' local - or, at least, as local as possible - characteristics; 3) the separation between full mineral tissue F and strongly demineralized FF, while being neat in theory, is actually far less marked, due to the intrinsic variability of the stochastic-foam-like structures, as well as to the non-homogeneous demineralization process, at the more local level. This finding implies that, from a structural point of view, highly porous F tissue is not that different from denser FF, especially in average demineralization conditions. Further, it supports the results of apparent density overlapping regions in compression tests, where F and FF behave almost the same at low strains (E_{app}), while presenting differences at higher strains ($\sigma_{app,f}$), probably due to different underlying mechanisms governing failure (see Figures 4.8 and 4.9).

By summing up, the method used proved to be reliable for the analysis of both full mineral and strongly demineralized trabecular bone tissues, not damaging them during the scanning phase. In the image post-processing phase, some problems in the correct detection of FF trabecular regions, were addressed: the main issue is repre-

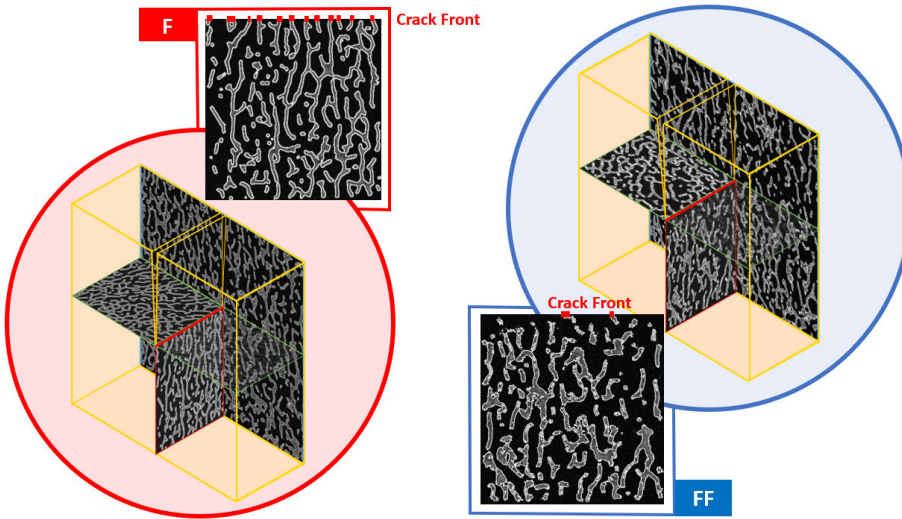


Figure 4.17: CT-scans on **F** and **FF** trabecular bone tissues. Images on the three fundamental planes are combined for the reconstruction of the structure of the specimens in correspondence of the notch. Further, magnified images of the notching planes were reported, on which the (discontinuous) crack fronts are represented with red dashed lines.

sented by the collagen component, especially in low mineral areas, as it is hard to be correctly individuated (and separated by the void regions), in comparison with the much more easily-detectable highly-mineralized *trabeculae*.

Fracture data elaboration

Raw load vs displacement curves coming from fracture tests on **F** and **FF** specimens were elaborated according to the method presented in Section 3.3. Thus, a twofold approach based on the separate analysis of both loading curves and high-resolution images taken during the tests was applied. The output of the method, consisting in the position of the critical points where relevant events for fracture initiation and propagation took place, are reported in Figure 4.18, for

4. TRABECULAR BONE TISSUES USED AS HETEROLOGOUS BONE GRAFTS

a representative F and FF specimen. Preliminary analyses seemed to indicate the possibility to resort to high-resolution images to place fracture initiation, which is an extremely difficult operation, even for *continuum* materials. Indeed, for *continuum*, uncertainties linked to surface-only inspection are always present, as early initiation is more likely to take place at the core of the specimen, where plain strain conditions occur. Well aware of such complications, fracture initiation was not placed at the peak of the loading curves, but rather in correspondence of specific points determined from curve-images approaches interaction. This is an extremely interesting result, as it suggests that an extremely local even like initiation could be traced back by referring to the macroscopic response of the entire specimen, in correspondence of either load peaks or significant slope variations on the loading curves. The same strategy was applied to place relevant crack propagation events (Figure 4.19). Raw loading curves were eventually corrected for the indentation effects using data coming from compliance correction tests. As linear elastic regions in fracture and correction tests were still detected at significantly different load levels (just like the case of polymer-based ACMs), data were corrected considering the whole curves, according to the procedure presented in Section 3.3. However, as no repeating patterns could be detected any longer due to the heterogeneity of stochastic-foam-like trabecular bone, correction tests corresponding to specimens with the closest apparent density were considered for the correction of each fracture test specimen.

F and FF tissue present an extremely different fracture response: while F is characterized by high loads, low displacements and a sudden failure, typical of brittle-like response materials, the high demineralization undergone by FF induced a markedly ductile response, resulting in low load and high displacement levels reached and progressive failure. This is clearly evident by carefully observing the region ahead of the crack tip, which is characterized by sharp and brittle crack propagation in the case of F tissue, while presenting extensive plastic deformation, crack blunt and eventually ductile crack

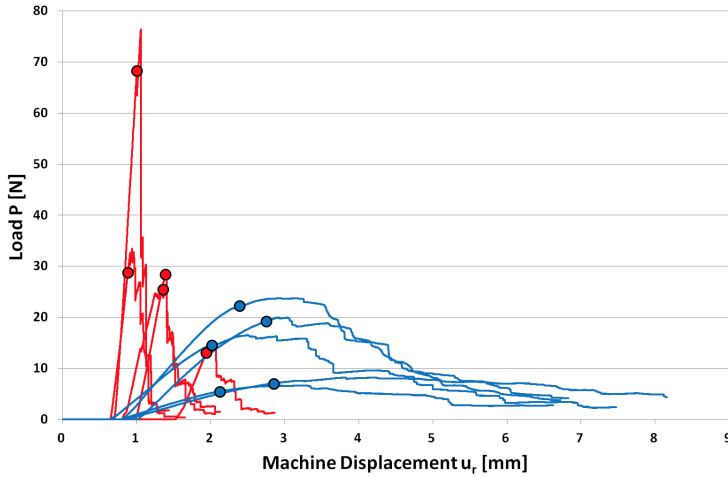


Figure 4.18: Fracture testing for **F** and **FF** specimens. Raw curves and fracture initiation ●. Data refer to non-corrected curves, before considering the indentation effect.

propagation in the case of FF tissue.

Fracture toughness

The radical difference in the response between F and FF suggested that different FM approaches had to be considered. Thus, LEFM and EPFM were selected as suitable for F and FF, respectively. The possible effect of viscoelasticity was considered during this initial stage. Recalling the results of creep tests (Section 4.3), the time scale over which viscoelastic phenomena were supposed to take place was far higher than the time frame proper of FM tests. Thus, the possible contribution of viscoelasticity, if present, was regarded not to significantly influence the fracture response of the systems, allowing to discard time-dependent FM schemes. The knowledge of the critical point where fracture initiation took place is crucial for the determination of fracture toughness. Considering the inherent complexity and heterogeneity of the systems, in addition to their porous nature,

4. TRABECULAR BONE TISSUES USED AS HETEROLOGOUS BONE GRAFTS

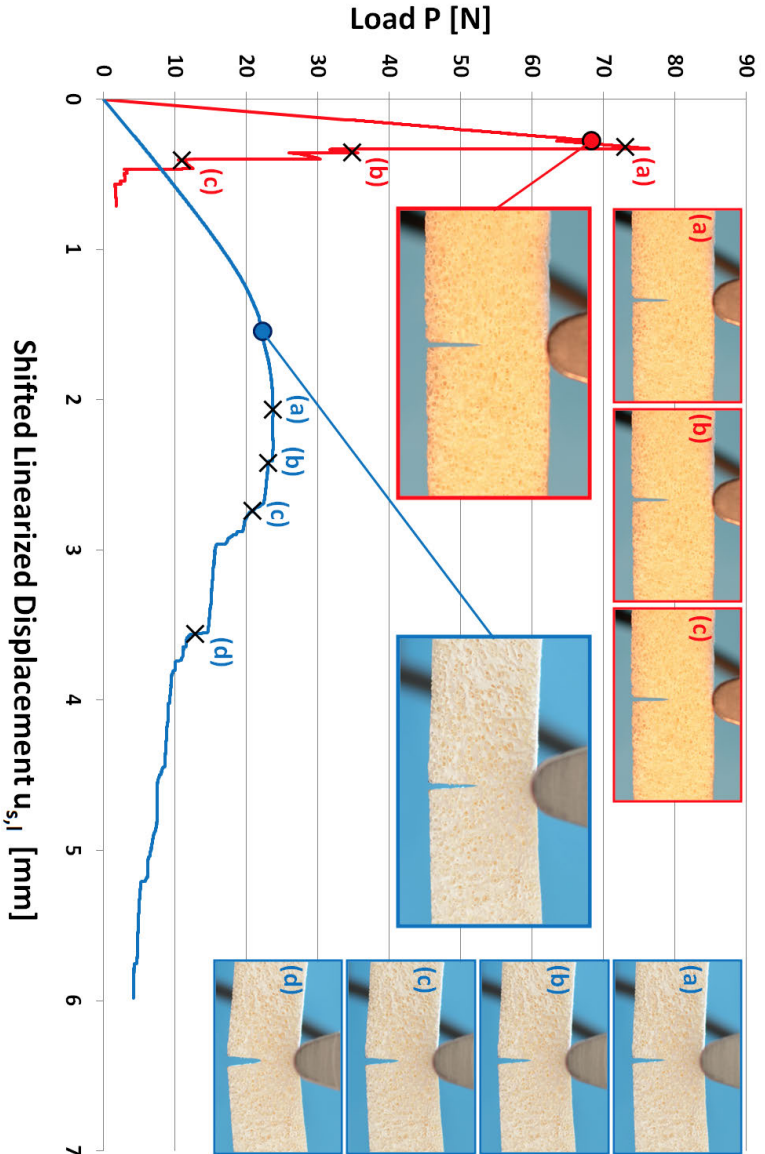


Figure 4.19: Fracture testing for **F** and **FF** specimens. Representative shifted and linearized loading curves. **X** crosses indicate the position of relevant crack propagation events. All the indicated stages of the fracture process are accompanied by the corresponding high-resolution images taken during the tests. Data refer to non-corrected curves, before considering indentation effects.

the energetic - rather than the stress - approach was followed. Thus, fracture toughness at initiation G_c and $J_{I,c}$ were calculated from the total energy up to critical point in the corrected curves, according to equations (2.15) and (2.27), for F and FF respectively. A direct comparison can be made, as G and J are representative of the same parameter, just considered either in LEFM or in EPFM. The energy-based fracture toughness data were plotted against the apparent density of the systems, ρ_{app} , as reported in Figure 4.20. The experimental data points - already properly corrected - clearly delineate two different responses. As F and FF were harvested from the same anatomic site and underwent the same deantigenation process, the demineralization treatment is the responsible of the different behaviour. According to Hassenkam et al.,⁶² fracture in untreated trabecular bone tissues is governed - at both trabecular surface and core - by collagen fibrils, which are responsible of toughening mechanisms, while mineral plates remain unaffected by the process. The fracture behaviour of F tissue can be traced back to this scenario. The results indicate that the highly-demineralized FF tissue can absorb more energy before fracture initiation occurs, resulting in higher fracture toughness. This interesting feature was attributed to the peculiar nature of FF constituent material, which is supposed to be capable of accommodating the stresses generated during the tests - and keeping them at lower values - thanks to the presence of low-mineral regions with highly-exposed collagen. In conditions with such low mineral relative percentages, the collagen fibrils - being previously blocked by mineral plates - are supposed to gain significant amount of mobility, which further accentuates the inherent plasticity of trabecular bone tissue. Thus, the residual strain build-up processes studied in compression tests at a global scale, are regarded to play an important role also in hindering and delaying fracture initiation and propagation, at a more local level.

⁶²Tue Hassenkam et al., "High-resolution AFM imaging of intact and fractured trabecular bone," *Bone* 35, no. 1 (2004): 4-10, ISSN: 87563282, <https://doi.org/10.1016/j.bone.2004.02.024>.

4. TRABECULAR BONE TISSUES USED AS HETEROLOGOUS BONE GRAFTS

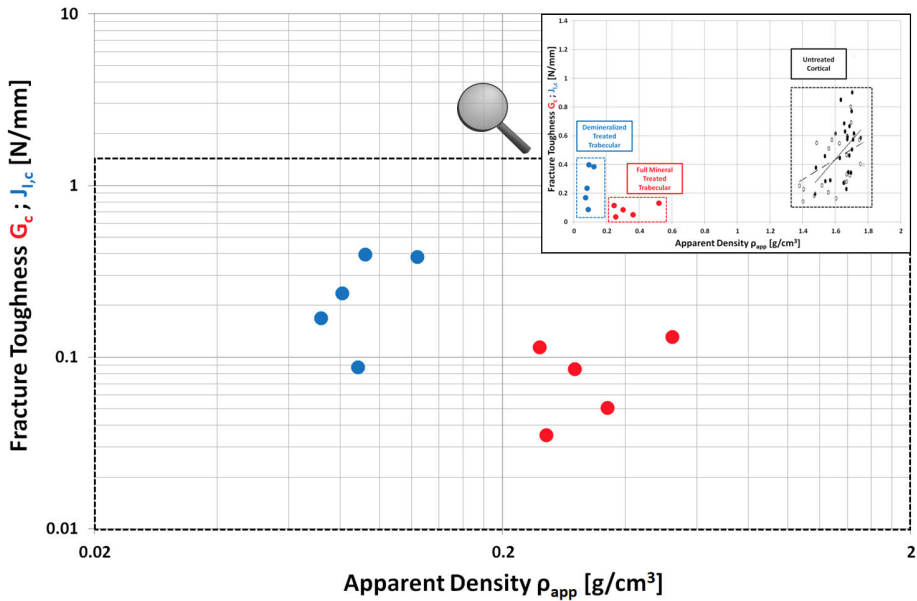


Figure 4.20: Fracture Toughness of F and FF tissues as a function of Apparent Density, ρ_{app} : energetic approach - G_c and $J_{I,c}$. Data are represented on bi-logarithmic axes. A comparison with literature data about cortical bone provided in [Yeni, Brown, and Norman, “Influence of bone composition and apparent density on fracture toughness of the human femur and tibia”] is reported in the in-box, where regular axes are used for the sake of better representation.

A direct comparison of fracture toughness data with relevant literature is extremely difficult, as the energetic approach is still quite overlooked. Thus, instead of considering G_c and $J_{I,c}$, the K parameter characterizing the tensional approach - which relies on the knowledge of the stress field in the crack region - was adopted. With regards to F, from critical load, P_{crit} , fracture toughness $K_{I,c}$ was determined according to LEFM equations (2.14) and (2.18-2.21). Conversely, in the framework of EPFM and following an approach proposed in liter-

ature about cortical bone tissues by Koester, Barth, and Ritchie,⁶³ $J_{I,c}$ data were converted into $K_{I,c-J}$

$$K_{I,c-J}^2 = EJ_{I,c} \quad (4.1)$$

which is equivalent to equation (2.10) in LEFM. It has to be noted that E is the elastic modulus derived from the specimen compliance measured in the fracture tests which, under the framework of LEFM and in plane stress conditions (see equation 2.22), is equal to the Young's elastic modulus. Thus, the elastic modulus from fracture tests, E_f , was determined for both F and FF tissue from corrected loading curves, according to equations equations (2.16-2.21). Figure 4.21 shows the relationship between the fracture toughness - either $K_{I,c}$ for F or $K_{I,c-J}$ for FF - and the apparent density of the systems, ρ_{app} . More specifically, while $K_{I,c}$ was determined directly from the loading curve, $K_{I,c-J}$ for FF tissue was calculated by using both E_{app} and E_f (◆ and ◇, respectively). As K is proportional to \sqrt{E} from equation (4.1), at fixed J , the general relationship observed $E_f > E_{app}$ led to $K_{I,c-J}$ values higher when determined from E_f , rather than from E_{app} . However, considering their spurious nature, $K_{I,c-J}$ values were considered for representative purposes only. Indeed, $K_{I,c}$ for F was regarded as the fundamental parameter for a comparison with relevant literature, as the peculiar and even accentuated heterogeneity degree of highly-demineralized FF tissue excluded it from direct check. A power-law best fitting curve was forced on F experimental data, resulting in $n = 1.6595$ as exponent value, which is consistent with FM classical relationship for open-celled cellular solids ($n = 3/2$), widely established in literature.⁶⁴

Despite the peculiar nature of the systems under analysis, a comparison between the results obtained for equine trabecular bone tissues - after proper treatments and possibly final demineralization -

⁶³Koester, Barth, and Ritchie, "Effect of aging on the transverse toughness of human cortical bone : Evaluation by R-curves."

⁶⁴Gibson and Ashby, *Cellular solids: Structure and properties, second edition*.

4. TRABECULAR BONE TISSUES USED AS HETEROLOGOUS BONE GRAFTS

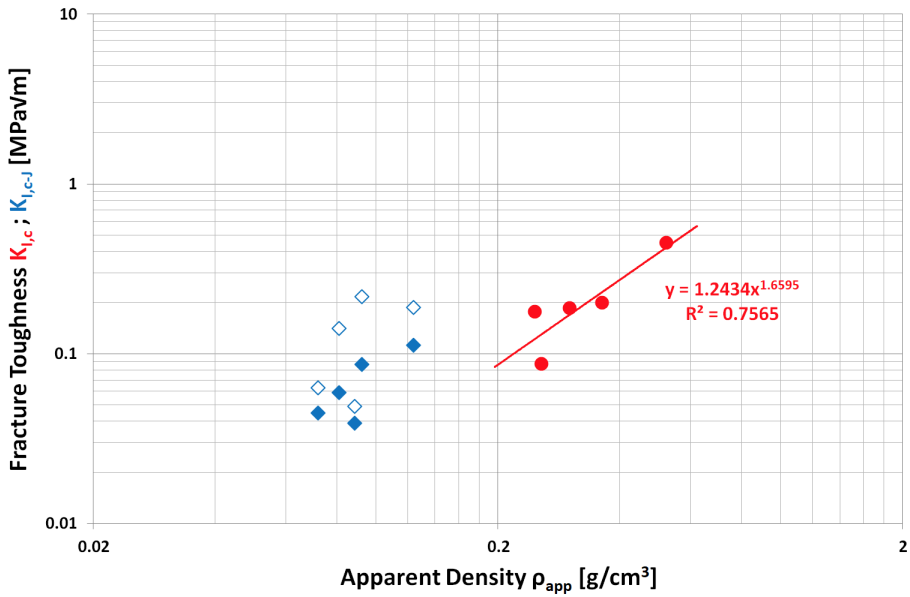


Figure 4.21: Fracture toughness at initiation as a function of apparent density, ρ_{app} , for F and FF tissues. Data for F tissue are reported in terms of $K_{I,c}$, determined directly from corrected loading curves (●), while $K_{I,c-J}$ is used for FF tissue, according to an approach presented in [Koester, Barth, and Ritchie, “Effect of aging on the transverse toughness of human cortical bone : Evaluation by R-curves”]. ◆ and ◇ correspond to data where the apparent elastic modulus (E_{app} from apparent density via theoretical prediction) and the elastic modulus from fracture tests, E_f , is considered, respectively.

and relevant literature about cancellous bone of heterologous origin was attempted. The data pool is extremely limited, even beyond the expectations, linked to the specific characteristics of the systems. However, a proper reference example was found in the studies of Cook and Zioupos,⁶⁵ in which both material origin and fracture testing procedures and data elaboration schemes were consistent. Cook and Zioupos⁶⁵ paid attention to the cutting direction during specimen shaping stage, in such a way to allow testing in both orthogonal and parallel direction with respect to the main trabecular orientations: this represents a relevant difference with the material here tested, as no preferential orientation was used during sampling phase. Thus, literature data were merged, before overlapping the $K_{I,c}$ data for F tissue, as represented in Figure 4.22, in which data from FF were tentatively located as well, for the sake of representation. $K_{I,c}$ resulted perfectly consistent with literature data, and the exponent check was brilliantly verified as well, being $n = 1.66$ for F and $n = 1.62$ and $n = 1.60$ for orthogonal and in-parallel testing data sets provided by Cook and Zioupos.⁶⁵

For F tissue, E_f was alternatively determined from K_c and G_c , according to equation (2.10). The so-obtained E_f values - in addition to E_f directly determined from corrected loading curves, for both F and FF, as previously described - were compared to apparent elastic modulus, E_{app} data coming from apparent density via theoretical prediction (Figure 4.8). The results are reported in Figure 4.23. By comparing the two alternative methods used for the determination of E_f , no relevant differences could be generally observed, supporting the validity of the FM scheme applied. Only one specimen presented significant variations from the trend. In this specific case, fracture initiation point was individuated in a region characterized by marked non-linearity. The E_f value calculated from loading curves takes this contribution into account. However, the application of LEFM to derive E_f from K_c and G_c totally overlooks the non-linear character of the loading curve, as well as relevant plasticity, thus providing sig-

⁶⁵Cook and Zioupos, "The fracture toughness of cancellous bone."

4. TRABECULAR BONE TISSUES USED AS HETEROLOGOUS BONE GRAFTS

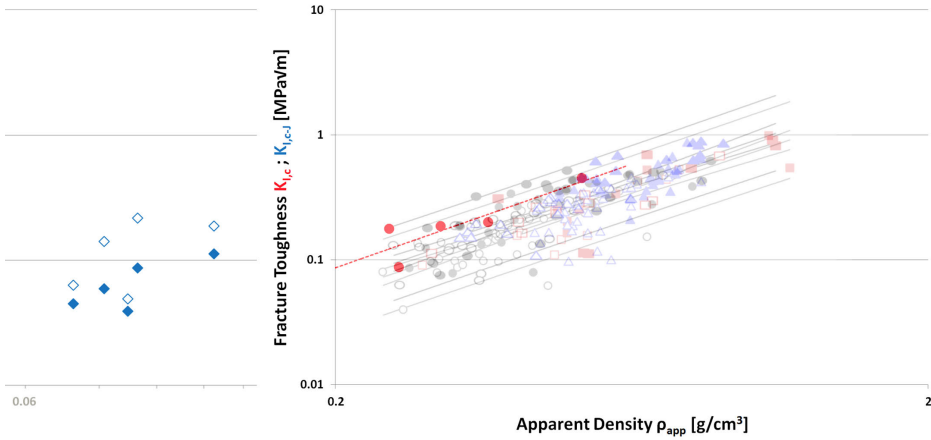


Figure 4.22: Fracture Toughness data, expressed as $K_{I,c}$ and $K_{I,c-J}$ for **F** and **FF** tissue respectively, as a function of Apparent Density, ρ_{app} . The experimental data points ($n = 1.66$) are successfully compared with relevant literature about heterologous trabecular bone fracture testing ($n \approx 1.6$), adapted from [Cook and Zioupos, “The fracture toughness of cancellous bone”]. See Figure 4.21 for further details about the symbol convention adopted.

nificantly different results. Conversely, by considering both F and FF tissues, the corresponding data points seem to delineate a unique trend, characterized by a linear dependency between E_f and E_{app} , in bi-logarithmic axes. The whole series is located above the bisector of the graph, meaning that E_f is greater than E_{app} , with relevant differences observable.

Load Separation Criterion (LSC)

By summing up the main outcomes obtained until now, while brittle F tissue was fully and successfully characterized in the framework of LEFM, the need for EPFM approaches to study the highly-peculiar demineralized FF tissue, as well as the complicated mechanisms underlying its fracture initiation and propagation, led to still unresolved

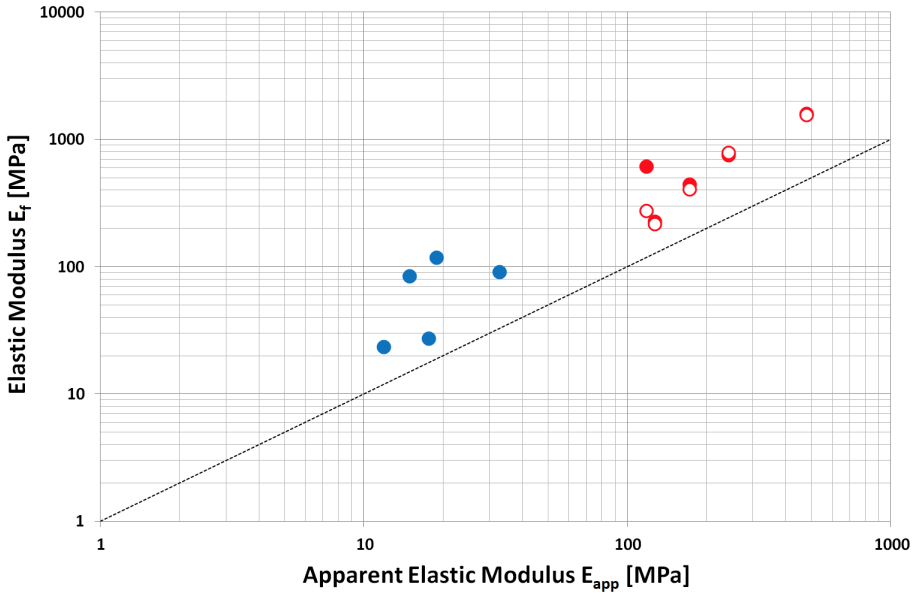


Figure 4.23: Elastic Modulus from fracture tests, E_f , vs Apparent Elastic Modulus, E_{app} , curves for F and FF tissues. ● refer to E_f values directly determined from corrected loading curves. For F tissue, an alternative path - based on the use of K and G parameters - is followed, and the results represented with ○ indicator.

questions. More specifically, the presence of widespread plastic deformation at crack tip, the occurrence of crack blunting and then the ductile crack propagation characterizing FF tissue, suggested that room for improvement was possible. The markedly ductile response - similar to the one manifested by some ductile polymers - which was not expected *a-priori* for a bone tissue, suggested the possibility to apply a criterion for ductile materials, the Load Separation Principle, LSC. LSC was initially proposed for metals in the 1990s,⁶⁶ before be-

⁶⁶M. Sharobeam and Landes, “The load separation criterion and methodology in ductile fracture mechanics.”

4. TRABECULAR BONE TISSUES USED AS HETEROLOGOUS BONE GRAFTS

ing extended and established for polymers as well.⁶⁷ LSC states that, in a fracture test with fixed material, geometry and constraint - load can be seen as the product of two independent contribution: a contribution only related to the geometry of the specimen (G-function) and a contribution only dependent on the material (H-function). LSC is defined by the relationship

$$P = G\left(\frac{b}{W}\right) \cdot H\left(\frac{u_{pl}}{W}\right) \quad (4.2)$$

where P is the load and $G(b/W)$ and $H(u_{pl}/W)$ are the geometry and material deformation functions, respectively. Stationary crack experiments, in which crack propagation is hindered by resorting to blunt notches, highlighted that for several geometries, including SE(B) configuration, the geometry function could be expressed as

$$G\left(\frac{b}{W}\right) = \left(\frac{b}{W}\right)^{\eta_{pl}} \quad (4.3)$$

where b is the ligament, W the width of the specimen ($b = W - a_0$) and η_{pl} the geometry dependent plastic calibration factor.⁶⁸ Preliminary tests on blunt tip notched specimens were carried out. It is important to point out that this kind of notch was meant to hinder crack propagation, differently from the case of sharp tip, where the notch had the role of induce stress intensification and preferentially drive crack propagation. Such activity was designed in order to verify the possibility to use multi-specimen approaches for fracture testing of trabecular bone tissues. Despite being the traditional approach for J-testing, in particular for metallic materials, the multi-specimen

⁶⁷Francesco Baldi, Silvia Agnelli, and Theonis Riccò, "On the applicability of the load separation criterion in determining the fracture resistance (JIC) of ductile polymers at low and high loading rates," *International Journal of Fracture* 165 (2010): 105–119, <https://doi.org/10.1007/s10704-010-9510-9>.

⁶⁸M. H. Sharobeam and J.D. Landes, "The load separation and η_{pl} development in precracked specimen test records," *International Journal of Fracture* 59 (1993): 213–226.

methodologies require several identical specimens to be tested in the same conditions and the capability to follow the crack advancement during the fracture test. However, the output obtained invalidated that possibility. This is an interesting result, as it confirms the unique and peculiar nature of each specimen (and, by extension, even of different regions within the same specimen), clearly evident from morphological analyses carried out using CT-scans. Thus, single-specimen approaches remained the only alternative available for the study of trabecular bone tissues. For each specimen, the G-function was calculated, by assuming $\eta_{pl} = 2$, as reported in relevant literature.⁶⁹ The normalization method⁷⁰ requires the determination of the material deformation function, which could be represented as

$$H = f\left(P_N, \frac{u_{pl}}{W}\right) \quad (4.4)$$

where u_{pl} is the plastic displacement and P_N the normalized load. The plastic displacement is defined as the difference between the displacement and the product between load and the mechanical compliance, C , evaluated in the linear elastic region

$$u_{pl} = u - P C \quad (4.5)$$

The normalized load is defined as load from fracture tests, normalized over geometrical parameters and geometry function G , according to the relationship

$$P_N = \frac{P}{G(b/W)BW} \quad (4.6)$$

As the G-function was calculated for each specimen, P_N could be obtained for each point of the loading curves. Further, from C , the

⁶⁹Baldi, Agnelli, and Riccò, "On the applicability of the load separation criterion in determining the fracture resistance (J_{Ic}) of ductile polymers at low and high loading rates."

⁷⁰F Baldi and T Ricco, "High-rate J-testing of toughened polyamide 6/6: Applicability of the load separation criterion and the normalization method," *Engineering Fracture Mechanics* 72 (2005): 2218–2231, <https://doi.org/10.1016/j.engfracmech.2005.02.002>.

4. TRABECULAR BONE TISSUES USED AS HETEROLOGOUS BONE GRAFTS

plastic displacement u_{pl} could be determined. The compliance correction procedure - aimed at taking into account the indentation effects - regarded the linear elastic regime, thus it did not affect the material deformation function, which if defined for plastic displacements (in the plastic region). By representing P_N as a function of u_{pl}/W , the Material Key Curves, MKCs, of FF tissue specimens were obtained (Figure 4.24). It is important to point out that MKCs - which are defined for plastic displacements - were determined up to the fracture initiation point, as crack lengths were required to be constant (and equal to a_0). Power-law best fitting trends were successfully forced on the experimental data, obtaining the model parameters. The power-law trends were then extended in the crack propagation region, under the hypothesis that the structure at crack front - extremely difficult to determine as tests progress - remains the same. At this stage, all the tools needed for the application of the normalization method were available.

First, the MKCs were used for the determination of the reconstructed curves of sharp notched specimens, following an approach about ductile polymers FM proposed in literature.⁷¹ The aim of such activity was to compare the loading curves as obtained from fracture tests with the reconstructed virtual curves, which are representative of a scenario in which no fracture propagation took place, as represented in Figure 4.25. While in the first region, both the fracture and the virtual curves perfectly superimpose, at a certain load level divergence occurs: the specimen progressively fails as a result of fracture propagation, significantly differing from its supposed response if fracture process was hindered. As a result of this approach, a couple of points are worth to be noted: 1) interestingly, by placing the crack initiation points - determined as previously discussed - on the curves, it emerges that they are located exactly in correspondence of the start of divergence process. This provides further validity to the

⁷¹Baldi, Agnelli, and Riccò, "On the applicability of the load separation criterion in determining the fracture resistance (J_{Ic}) of ductile polymers at low and high loading rates."

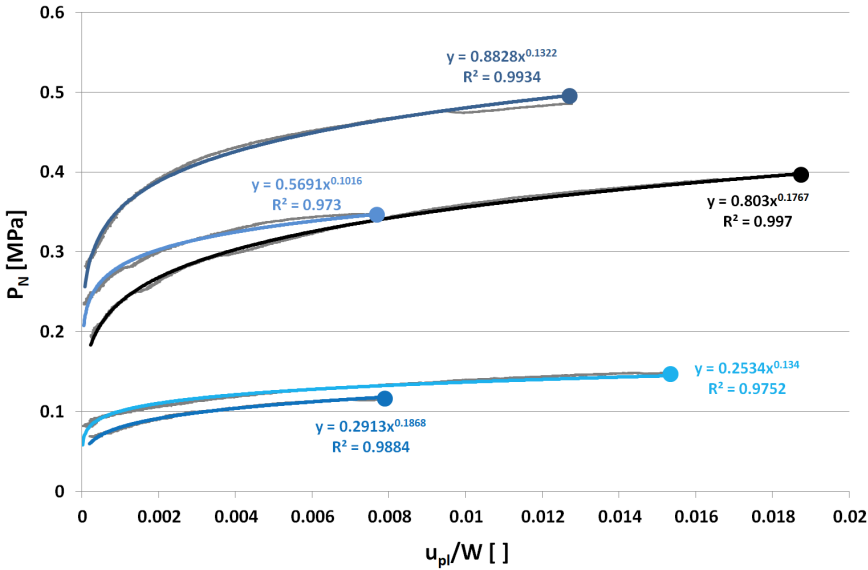


Figure 4.24: Material Key Curves (MKCs) - Normalized Load, P_N , vs u_{pl}/W - for FF tissues. Power-law trends fitted on the experimental data, are reported with full lines, alongside their equation. MKCs are constructed up to fracture initiation point, represented with ● indicator.

technique used for the determination of fracture initiation, as well as suggests that it is the responsible of the failure of the specimens; 2) the reconstructed curves give an idea of the response of the specimens in the case of hindered fracture initiation and propagation, which means if the low-mineral high-mobility collagen network was able to accommodate the stresses by means of crack blunting and plastic deformation build-up mechanisms.

For each specimen, an arbitrary initial (displacement;load) data couple was selected. As it was necessary for the data points to be located in the plastic displacement region ($u_{pl} \geq 0$), and in particular in the fracture propagation regime, the fracture initiation point was selected as suitable. Then, an arbitrary small value of crack advancement, Δa , was initially assumed, obtaining the actual crack length

4. TRABECULAR BONE TISSUES USED AS HETEROLOGOUS BONE GRAFTS

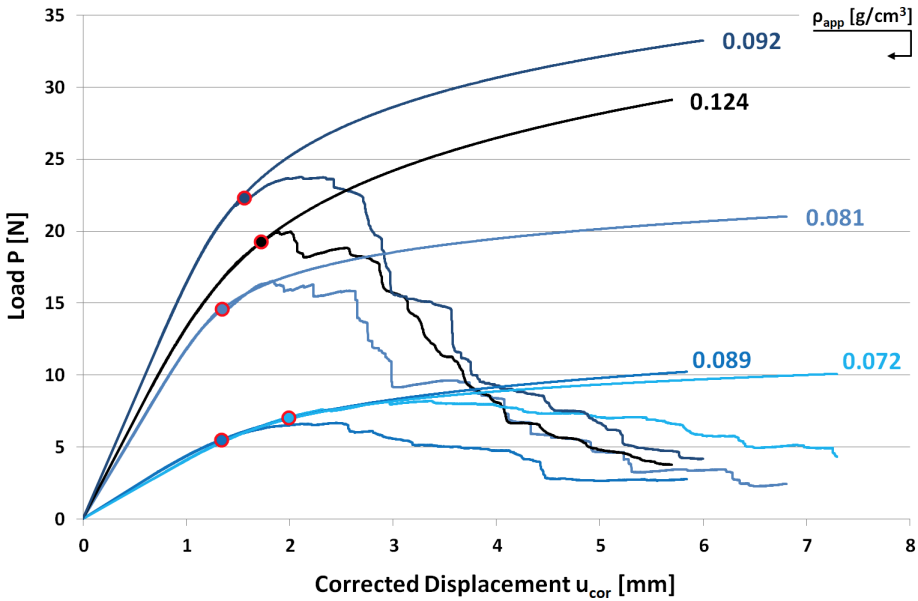


Figure 4.25: Fracture and reconstructed loading curves of sharp notched **FF** specimens, as a result of the application of the LSC-based normalization method proposed in [Baldi, Agnelli, and Riccò, “On the applicability of the load separation criterion in determining the fracture resistance (J_{Ic}) of ductile polymers at low and high loading rates”]. The local apparent density of each specimen is reported alongside the curves. In addition, the corresponding fracture initiation points are placed using the ● indicator.

$a = a_0 + \Delta a$ and eventually the actual crack to width, $\alpha = a/W$, ratio. For the SE(B) configuration, by sequentially relying on equation (2.18), (2.20), (2.21), (2.19) and (2.16), the actual compliance $C(a)$ could be determined. By recalling equation (4.5), the actual plastic displacement - referring to the specific Δa assumed - was obtained, using $C(a)$. Then, the knowledge of the material deformation function allowed to use MKCs model parameters to calculate the normalized load corresponding to the selected Δa . The final step consisted in the backward application of equation (4.6), where G-function and geometrical parameters were used for the determination of the load,

once again corresponding to specific level of Δa . This entire procedure was finalized at the obtainment of this reconstructed load value via normalization method, to be then compared to the actual load coming from the initial (displacement;load) data couple selected at the initial stage. More specifically, the difference between those values, ΔP , was minimized, thus implying the reconstructed load to be representative of the actual load and thus validating the Δa value initially assumed. By using the fracture initiation as reference point, if Δa values as small as possible turned out to produce minimum ΔP , the validity of the procedure could be confirmed. For each specimen, the results of this cross-check procedure were positive. Once the process was validated, for each specimen, other (displacement;load) located in the fracture propagation region were selected. For each one, after a tentative Δa was assumed, the procedure was iteratively applied up to the condition of minimum ΔP , corresponding to the correct value of crack advancement Δa . The more (displacement;load) couples were analyzed, the more accurate information could be deduced about fracture propagation. Their values were then employed for the determination of energy provided up to the corresponding points, which was eventually used to calculate the fracture toughness parameter, J-integral, according to equation (2.27). The relationship between the fracture toughness parameter and the actual crack advancement is conventionally referred to - in relevant literature about *continuum* materials⁷² - as R-curve of the material. In the specific case of cellular materials, R-curves are regarded as representative of the system, which is the result of the synergistic effect of both constituent material and architectural features. R-curves obtained for the highly-demineralized FF tissue specimens used for fracture testing was reported in Figure 4.26a. The power-law trend parameters were reported in Table 4.7. The pool of experimental data - meaning the (displacement;load) couples previously mentioned - considered was in the order of 10 – 15 points for each specimen. A power-law best fitting curve was forced on the experimental data. It clearly

⁷²Anderson, *Fracture Mechanics : Fundamentals and Applications*.

4. TRABECULAR BONE TISSUES USED AS HETEROLOGOUS BONE GRAFTS

emerges that the curves do not overlap, even though three of them are extremely similar. This, once again, confirms the impossibility to rely on multi-specimen approaches, as well as the unique character of each specimen, whose structure and material composition in the region ahead of the crack tip are regarded to control the entire fracture initiation and crack propagation process. It is important to emphasize a few fundamental points about the method used for the construction of R-curves, in particular regarding the nature of Δa :

- Δa values were not obtained by monitoring the crack advancement during fracture tests - a methodology widely employed for metals, but non applicable to polymers and in general to time-dependent materials, due to their viscoelastic nature - but rather indirectly determined on the basis of an optimization algorithm based on actual (displacement;load) data couples;
- as Δa increases during fracture tests, the actual structure at the crack tip is likely to change, due to the stochastic-foam-like architecture and the material heterogeneity characterizing trabecular bone - and even further such treated and highly-demineralized tissues. However, the normalization method applied, based on the hypothesis of an arbitrary Δa value and its subsequent optimization for the entire amount of experimental data points desired, assumes the structure at crack tip as constant. Thus, as fracture propagation takes place, the J-integral data always refer to the structure at initiation.
- the optimization algorithm used on experimental data couples provided results up to $\Delta a = 7$ mm. While the procedure could in theory be applied without any constraint, so that arbitrary high values of Δa could be obtained, the meaning of the results was always questioned. Thus, optical microscopy analyses were carried out on the specimens after testing, in order to assess - if possible, by relying only on the analysis of the surfaces - the actual values of crack advancement (Figure 4.26b). The

Table 4.7: R-curve power-law fitting parameters for FF tissues.

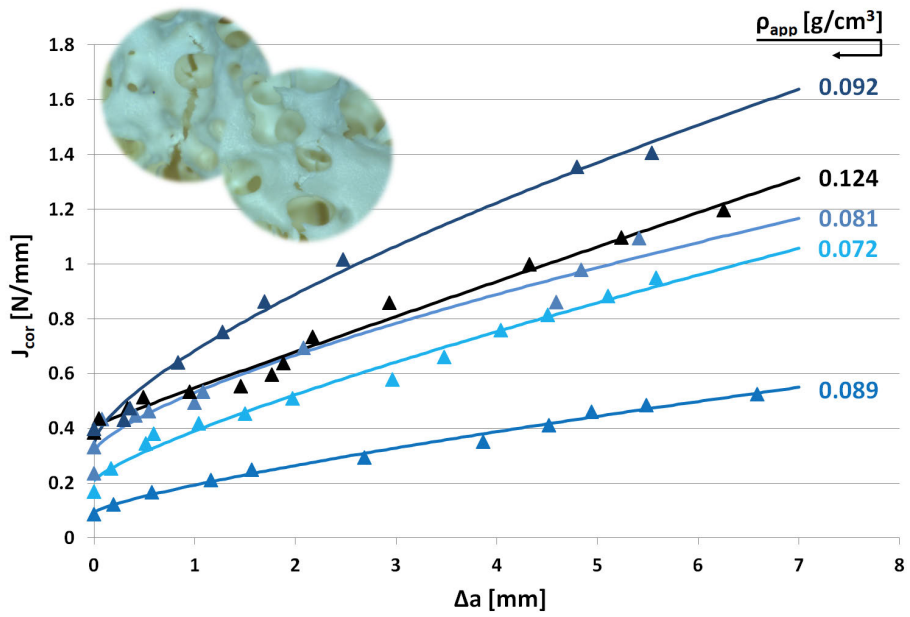
MKCs power-law fitting			
Specimen	$J_{\text{cor}} = d \cdot \Delta a^f + g$		
	d	f	g
FF1	0.2165	0.7041	0.3142
FF2	0.0989	0.7850	0.0941
FF3	0.1386	0.9634	0.4089
FF4	0.1812	0.7930	0.2090
FF5	0.3340	0.6940	0.3490

results obtained were consistent with the range explored on the R-curves, providing reliability both to the experimental points and to the power-law trends forced on them.

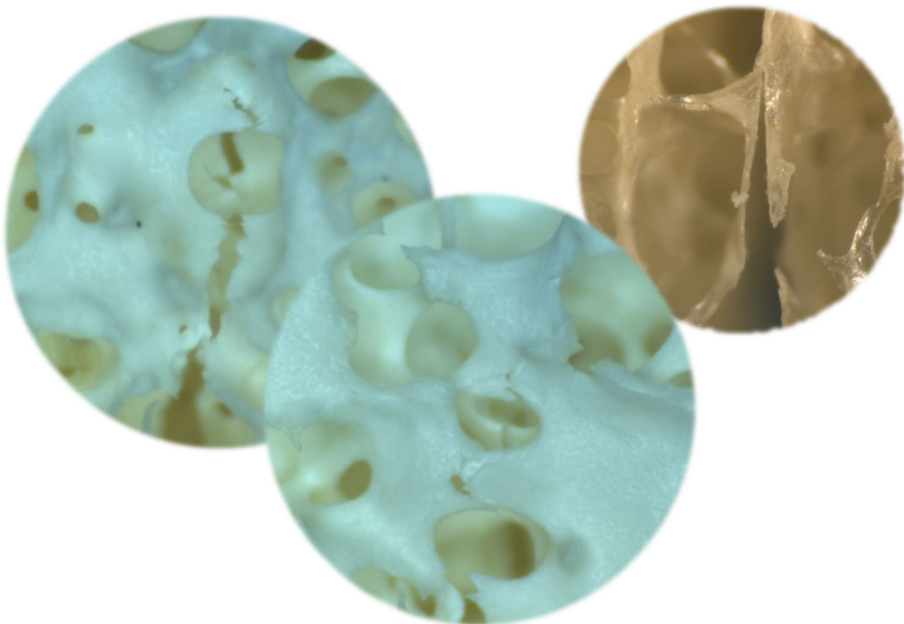
A potential correlation with apparent density, ρ_{app} , was tentatively explored. However, ρ_{app} seems not to be responsible for the trend of R-curves, suggesting that even more local parameters would probably control the fracture response, like local architecture and constituent material - mineral and collagen - relative percentages. The use of CT-scans on post-test specimens is supposed to improve the understanding of the relationship between crack propagation and local structure, as well as provide further and more detailed information about actual maximum crack advancement. Indeed, the central region of the specimens could be examined, which was precluded to optical microscopy analyses.

By converting the data into K-J parameter, according to equation (4.1), a direct comparison with relevant literature about cortical bone tissues - which frequently reports experimental data according to this

4. TRABECULAR BONE TISSUES USED AS HETEROLOGOUS BONE GRAFTS



(c)



(b)

Figure 4.25: R-curves, expressed as fracture toughness J_{cor} vs crack advancement Δa , for FF tissue specimens. The reference data points are represented with \blacktriangle , on which the corresponding power-law best fitting lines are forced. Lighter to darker shades of blue indicate increasing specimen apparent density, whose values are reported alongside. The data are accompanied by representative images of crack propagation in the highly-demineralized FF trabecular bone tissue (a). Magnified images of cracked demineralized trabecular bone tissue are reported, accompanied by representative FF tissue notch.

approach^{73,74} - could be assessed (Figure 4.26). An order of magnitude in the fracture toughness values was observed between cortical and trabecular bone tissues. While for fracture initiation, some extremely limited literature could be used as suitable benchmark, it is important to underline that fracture propagation approaches aimed at the determination of R-curves were never attempted on trabecular bone tissues. This provides a further degree of novelty to the research, in addition to the innovative methodological approach and to the possibility to study crack propagation without directly monitoring crack growth on the specimen - consolidated for *continuum* but never applied to such complex porous materials.

Finally, following the same approach adopted for polymer-based ACMs (Section 3.3), the relationship between the normalized fracture toughness parameters over apparent density- $G_{I,c}/\rho_{\text{app}}$ and $J_{I,c}/\rho_{\text{app}}$ for F and FF, respectively - and the normalized elastic modulus from fracture tests, E_f/ρ_{app} , was studied, as reported in Figure 4.27. As FF was characterized by higher fracture toughness values at initiation, the normalization over smaller apparent density values led to a broader difference, in comparison with F tissue. Further, FF seems to

⁷³R. K. Nalla et al., "Effect of aging on the toughness of human cortical bone: evaluation by R-curves," *Bone* 35 (2004): 1240–1246, <https://doi.org/10.1016/j.bone.2004.07.016>.

⁷⁴Koester, Barth, and Ritchie, "Effect of aging on the transverse toughness of human cortical bone : Evaluation by R-curves."

4. TRABECULAR BONE TISSUES USED AS HETEROLOGOUS BONE GRAFTS

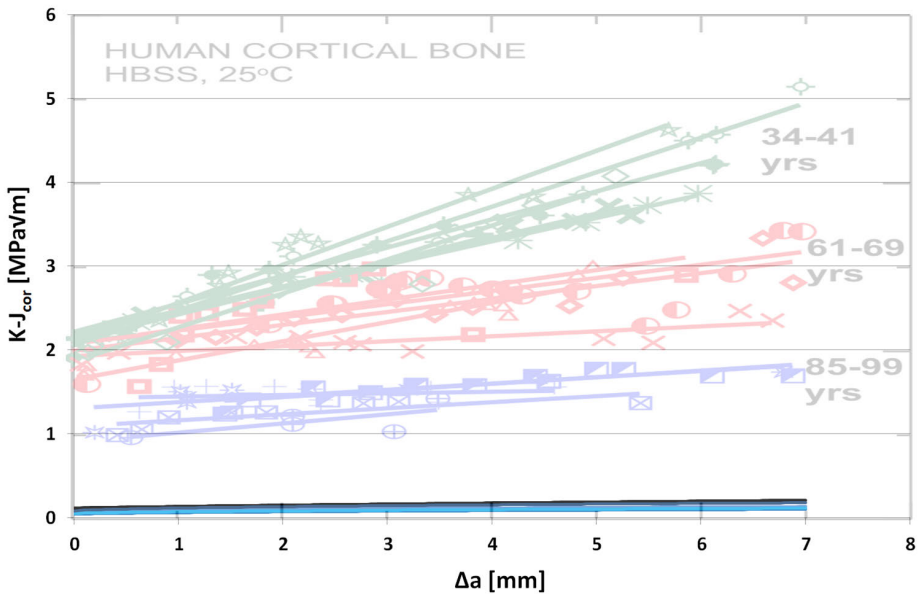


Figure 4.26: R-curves, expressed as $K-J_{cor}$, for FF tissue specimens, in comparison with relevant literature data for cortical bone, adapted from [Koester, Barth, and Ritchie, “Effect of aging on the transverse toughness of human cortical bone : Evaluation by R-curves”].

be characterized by a linear trend - not observable in the case of F - according to which high performances at low strains are accompanied by high-energy absorption and damage tolerability, in specific terms.

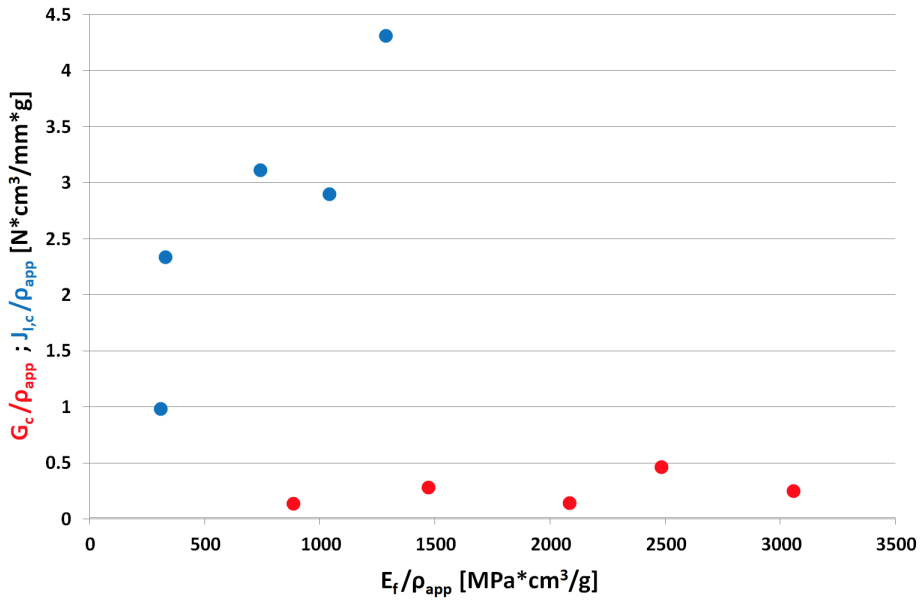


Figure 4.27: Normalized Fracture Toughness at Initiation, $G_{I,c}/\rho_{app}J_{I,c}/\rho_{app}$, vs Normalized Elastic Modulus from fracture tests, E_f/ρ_{app} for **F** and **FF** tissue, respectively.

Conclusions

In this work, the structural integrity of cellular materials was studied. Natural stochastic foams (trabecular bone) and Architected Cellular Materials, ACMs, (3D-printed polymer-based structures), characterized by open cells and interconnected porosity, were examined. The study of the structural integrity was carried out in the framework of Fracture Mechanics, FM. The attention was focused on commercial trabecular bone tissues used for the manufacturing of heterologous bone grafts, properly treated to ensure biocompatibility and with varying mineral content. However, the architectural complexity of the systems, their heterogeneity even within the *trabeculae* - due to mineral and collagen copresence, with varying relative percentages - in addition to their porous structure, pushed to address some methodological problems on simpler systems. Thus, 3D-printed ACMs (in a ductile polymeric material, ABS) characterized by controlled architecture and porosity levels consistent with trabecular bone - were developed and manufactured. The final aim of the research activity was to develop, within the framework of FM, new solutions to face specific methodological issues directly related to the peculiar nature of the systems examined (starting from ductile polymer ACMs and then extending to trabecular bone), for the assessment of the structural integrity of cellular materials, to be used to find robust structure-property relationships.

Regarding the polymer-based ACMs, special attention was paid to

the structure design and sample manufacturing phases. As the extruded filament was meant to be the reference structural element of these materials, particular interest was placed on the thermo-mechanical history experienced by the ABS resin extruded by the FDM machine nozzle. A basic unit composed of 4 layers with different orientations (0° , 45° , 90° , -45°) was repeated in the layer stacking direction to build up the specimens with geometry and dimensions suitable for the execution of compression, tension and FM tests. The mechanical characterization under compression was performed on specimens with nominal porosity of 70% (actual porosity of 70%). As the classical literature definition for cellular materials requires minimum porosity levels of 70%, the applicability of the theoretical relationships to such boundary structures had to be questioned. Repeating patterns were found in specimens with different sizes, by means of morphological analyses at the optical microscope. The analysis pointed out a tri-linear stress-strain behaviour (corresponding to three different regimes) in the layer stacking direction, consistent with relevant literature. The effect of specimen size and geometry, where present, seemed not to produce pronounced variations in terms of mechanical properties, stiffness and strength. Further, the occurrence of plasticity (studied by means of specific cyclic compression tests) was observed in correspondence of the I-II regime transition region. Densification processes were studied as well, turning out to induce cell shape and size distortion (structural deformation of the system) and whitening of ABS material (deformation within the filament), at about 20% of apparent strain. FM characterization was performed on single edge notched in bending, SE(B) specimen (notched bars subjected to three-point bending). At this stage, specimens with various degrees of actual porosity were produced, starting from $\approx 75\%$ and down to $\approx 20\%$ (no more full-fledged cellular materials, according to their definition). Higher relative densities were explored to point out the underlying deformation and failure mechanisms. The markedly ductile fracture response of the systems required to resort to EPFM approaches, requiring the implementation of spe-

cific correction tests in order to take into account the roller-testpiece indentation effects. These tests were performed in such a way as the structure at the roller-testpiece contact points resulted the same as during the fracture test. Specific data elaboration schemes were developed. The elastic modulus determined from the specimen compliance measured in the fracture tests turned out to be dependent on the apparent density of the systems with a power-law trend (as in the proper open-celled materials) up to the minimum porosity level examined, in correspondence of which an abrupt variation was observed. A twofold approach based on loading curves analysis and high-resolution image observations allowed to individuate fracture initiation and to place further relevant fracture propagation events. Fracture initiation occurred well before the achievement of the peak in the loading curves. Fracture toughness was calculated by using the J-integral concept. By taking into account the experimental uncertainty associated to the data, fracture toughness at initiation ($J_{I,c}$) seemed to assume almost constant values over a wide range of porosity (35%-75%), once again manifesting an abrupt variation in correspondence of the minimum porosity value. Such transition was supposed to be related to the architecture of the systems, which is characterized only by *inter*-layer filament contact points over a wide range of porosity, while presenting additional *intra*-layer contact surfaces between filaments when *continuum*-like conditions were approached. As porosity levels were reduced, the importance of delamination processes after fracture initiation decreased. The architecture of the systems was studied also by means of CAD models, developed by using the dimensions and key geometrical parameters taken on the actual specimens. By sectioning the model in correspondence of notch position, the presence of surface contact between filaments within the same layer was confirmed in the minimum porosity specimens - which turned out to manifest actual porosity values of $\approx 20\%$, in contrast with nominal 100% infill level. Further, the discontinuous nature of crack front - at least up to minimum porosity levels - was clearly pointed out.

Once the methodology for mechanical and fracture testing of

ACMs was set and critically examined, it was applied to the more complex case of trabecular bone. An initial mechanical characterization was performed *via* compressive tests, pointing out a brittle-like response for tissues with unchanged mineral content (F and H, coming from different anatomic sites), and a significantly different, ductile-like response for the highly-demineralized FF tissue (F tissue after undergoing a final demineralization treatment). The mechanical stiffness turned out to be strongly dependent on the apparent density of the tissue, according to a power-law trend consistent with relevant literature. Trabecular material, architecture, specimen size and geometry, and loading direction played only a secondary role on the small-strain response. At higher strains, as the mechanical strength proved to be strongly dependent on apparent density once again - while keeping insensitive to specimen geometry, architecture and loading direction - the effect of mineral content in trabecular material was relevant, leading to an offset in FF data (stress at failure represented against the tissue density), in comparison to F and H. This suggested that different failure mechanisms were activated, depending on the relative percentages of mineral and collagen within *trabeculae*. Morphological analyses on ductile-like FF tissue clearly demonstrated the occurrence of plasticity during compression tests - in the form of cell shape and size distortion, permanent deformation of the entire structures and within the *trabeculae* and possibly breakage in correspondence of microdefects. The nature of such plasticity was studied by means of cyclic tests (according to the method used for polymer-based ACMs), which pointed out the non-recoverable nature of residual strains and their build-up process, starting to take place at $\approx 2\%$ strain (in correspondence of the knee region of the stress-strain curve). Creep tests aimed at the investigation of the viscoelastic nature of the systems, pointed out the possible occurrence of failure under static loads. Fracture tests were performed on SE(B) specimens. The methodology developed for ACMs was applied. Sharp notches were obtained, without inducing damage ahead of crack tip, even in the case of the highly compliant FF tissue. Optical microscopy analy-

ses were used as quality control during the various steps of specimen preparation. The discontinuous nature of the crack front (just like ACMs) was proved by CT-scans, which provided a further indication of the quality of preparation procedure. Indeed, CT-scans proved the unique nature of each specimen and the existence of different regions even within the same specimen, questioning the possibility to use multi-specimen approaches. In order to take into account the possible effect of structure on indentation, as repeating patterns could not be detected in a stochastic-foam-like material, an approach based on the local apparent density was used. The data elaboration technique developed for ACMs was used for the determination of the corrected loading curves. The fracture response of the systems turned out to be strongly influenced by mineral content. Thus, brittle-like F and ductile-like FF tissues were studied in the framework of LEFM and EPFM, respectively. Viscoelastic approaches to FM were discarded as the differences in the characteristic time scales of creep and fracture tests suggested viscoelasticity to play only a secondary role on the fracture response. The synergistic approach based on loading curves and high-resolution images analysis was applied, to place fracture initiation and possibly the most relevant crack propagation events. Aware of the uncertainties in the individuation of a fracture initiation point (still present even in *continuum* materials), fracture toughness was determined according to the FM theory. The energetic approach was preferred over the tensional one since it does not take into account the complex stress field at crack tip induced in the porous structure, further complicated by the heterogeneity in architecture and even in the constituent material. As two separate series were observed in fracture toughness results, the trabecular material - or at least the mineral and collagen relative percentages - turned out to be the fundamental parameter for the systems' response, in addition to the apparent density of the tissue. By converting the data into tensional fracture toughness parameters, a positive correlation with relevant literature was assessed. regarding both cellular materials in general and heterologous trabecular bone tissues. As the possibility to

rely on multi-specimen approaches - addressed by means of fracture tests on blunt notched specimens - was discarded, a single-specimen approach, based on the Load Separation Criterion, LSC - developed for metals and successfully applied to continuous polymeric materials - was tentatively applied to the case of ductile FF tissue. The attention was focused on crack propagation. Thus, by applying the LSC-based normalization method, it was possible to construct the crack resistance curve, R-curve (fracture toughness vs crack advancement), for the various FF tissue samples examined. This is very interesting, as R-curves, while being extensively studied for cortical bone, were never examined in the case of trabecular bone, not to mention in such peculiar conditions - commercial products of extreme industrial interest, that underwent deantigenation and high demineralization. Power-law trends were observed for the R-curves, and the results showed that the response was not governed by the apparent density of the tissue, thus confirming the important role of the very local structure at the crack tip.

By summing up, the applicability of FM testing approaches to cellular materials was critically examined, and new solutions adopted to face specific methodological issues directly related to the peculiar nature of the systems developed. Ductile polymer cellular model structures manufactured by FDM (ACMs) were examined first, and the outcomes used as reference for the characterization of stochastic-foam-like trabecular bone tissues. For the specific case of highly ductile markedly demineralized bone tissue, a cutting-edge research based on the application of the Load Separation Criterion (LSC) was carried out, which led to the tentative construction of R-curves, never attempted before even for untreated trabecular bone.

Some of the results of this research work were extensively analyzed in scientific papers in peer-reviewed relevant literature journals.

- Agnelli et al., "Mechanical behaviour of cancellous bone tissues used for the manufacturing of heterologous bone grafts", *Biomedical Engineering Advances* 5 (2023): 100073.

-
- Agnelli et al., "Mechanical behaviour of ductile polymer cellular model structures manufactured by FDM", *Mechanics of Materials* 190 (2024): 104882.

Future perspectives

In this work, the study of the structural integrity of 3D-printed cellular model structures in ductile polymeric material was assessed. The mechanical response was firstly explored according to the *Continuum Mechanics*, before investigating it within the framework of Fracture Mechanics. The effect of the systems' structure on fracture toughness, in terms of both *inter-* and *intra-*layer interaction between filaments, turned out to be crucial. Thus, further investigation on this topic may shed some light on the underlying mechanisms governing the response. As the type of approach adopted was fully experimental, the implementation of simulation analyses - which is regarded as a suitable future step on this topic - is currently being carried out. More specifically, taking advantage of the CAD models of the structures previously developed, the fracture response of the systems in presence of a crack - introduced in a specific point within the specimens and characterized by initial length known *a-priori* - will be investigated *via* FEM techniques.

The same approach, considering firstly *Continuum* and then Fracture Mechanics, was adopted for the study of the structural integrity of heterologous trabecular bone tissues. Once again, as the work was meant to be fully experimental and the attention was deliberately focused on the response of the systems at the macro-scale, morphological more in-depth analyses are currently planned. More

specifically, crack propagation during fracture tests is meant to be explored by relying on CT techniques, by scanning the pre-cracked specimen both before and after the tests. Such approach is regarded to provide information on extension and branching of the induced propagated cracks within the specimens as well, supporting the optical microscopy approach already used for surface analyses. Further, the possibility to obtain the actual 3D models of the specimens will be exploited, paving the way for FEM analyses to be carried out. Finally, as fracture toughness turned out to be strongly dependent on apparent density, the possibility to set up experimental rule of thumbs - based on the measurement of rather easily accessible properties - for the selection of the most suitable trabecular bone tissues for a specific clinical application will be explored. In this scenario, while the mechanical characterization within *continuum* mechanics was performed on a wide data base, in order to study the experimental variability of the results - the relatively simple testing conditions allowed it - the study of the structural integrity of the tissues in the framework of FM was limited to a relatively small amount of specimens. Indeed, so far the attention was focused on the interpretation of the underlying mechanisms governing the process and on specific methodological aspects for the characterization of the systems, based on the LSC and applied to the highly-demineralized trabecular bone tissue, due to its relevant scientific and industrial interest. The determination of R-curves for such kind of material represents a cutting-edge research achievement, as it was never been attempted before even for regular trabecular bone. In the future, statistical analyses of the data are meant to be performed in the framework of a close collaboration with industrial partners, for more in-depth studies on specific batches of materials of high industrial interest, where extensive data population is required.

Acknowledgments

The author sincerely thanks the Materials Science and Technology Laboratory (Department of Mechanical and Industrial Engineering, University of Brescia), for the support and the expertise provided throughout the doctoral program.

Bioteck S.p.A. (Arcugnano, Vicenza, Italy) and STIIMA-CNR (Milano, Italy) are highly acknowledged for the collaboration to the research project and the manufacturing of the cellular materials under analysis. Fabbrica d'Armi Pietro Beretta S.p.A. (Gardone Val Trompia, Brescia, Italy) is acknowledged for the support with CT-scans and image processing kindly provided. Industrie Polieco-M.P.B. S.r.l. (Caz-zago San Martino, Brescia, Italy) and CSMT Gestione S.c.a.r.l. (Brescia, Italy) are acknowledged for the support provided to the research activity.

Bibliography

- Abou-ali, Aliaa M, and Oraib Al-ketan. "Mechanical Response of 3D Printed Bending-Dominated Ligament-Based Triply Periodic Cellular Polymeric Solids." *Journal of Materials Engineering and Performance* 28, no. 4 (2019): 2316–2326. ISSN: 1544-1024. <https://doi.org/10.1007/s11665-019-03982-8>.
- Aerssens, Jeroen, Steven Boonen, Geert Lowet, and Jan Dequeker. "Interspecies differences in bone composition, density, and quality: Potential implications for in vivo bone research." *Endocrinology* 139, no. 2 (1998): 663–670. ISSN: 00137227. <https://doi.org/10.1210/endo.139.2.5751>.
- Agnelli, S., F. Baldi, L. Castellani, K. Pisoni, M. Vighi, and L. Laiarinandrasana. "Study of the plastic deformation behaviour of ductile polymers: Use of the material key curves." *Mechanics of Materials* 117, no. July 2017 (2018): 105–115. ISSN: 01676636. <https://doi.org/10.1016/j.mechmat.2017.11.002>.
- Almomani, Abdulla, and Abdel Hamid I. Mourad. "The fracture toughness of Schwarz Primitive triply periodic minimal surface lattice." *Theoretical and Applied Fracture Mechanics* 125, no. May (2023): 103924. ISSN: 01678442. <https://doi.org/10.1016/j.tafmec.2023.103924>.
- An, Yuehuei H., and Robert A. Draughn. *Mechanical testing of bone and the bone-implant interface*. 624. CRC Press, 2000. ISBN: 9780849302664.

BIBLIOGRAPHY

- Anderson, T.L. *Fracture Mechanics : Fundamentals and Applications*. CRC Press, March 2017. ISBN: 9781315370293. <https://doi.org/10.1201/9781315370293>.
- Askari, Meisam, David A. Hutchins, Peter J. Thomas, Lorenzo Astolfi, Richard L. Watson, Meisam Abdi, Marco Ricci, et al. "Additive manufacturing of metamaterials: A review." *Additive Manufacturing* 36, no. September (2020): 101562. ISSN: 22148604. <https://doi.org/10.1016/j.addma.2020.101562>.
- Bachtiar, Emilio Omar, Virginia Cary Ritter, and Ken Gall. "Structure-property relationships in 3D-printed poly(L-lactide-co- ϵ -caprolactone) degradable polymer." *Journal of the Mechanical Behavior of Biomedical Materials* 121, no. April (2021). ISSN: 1751-6161. <https://doi.org/10.1016/j.jmbbm.2021.104650>.
- Badiche, X., S. Forest, T. Guibert, Y. Bienvenu, J. D. Bartout, P. Ienny, M. Croset, and H. Bernet. "Mechanical properties and non-homogeneous deformation of open-cell nickel foams: Application of the mechanics of cellular solids and of porous materials." *Materials Science and Engineering A* 289, no. 1 (2000): 276–288. ISSN: 09215093. [https://doi.org/10.1016/S0921-5093\(00\)00898-4](https://doi.org/10.1016/S0921-5093(00)00898-4).
- Baldi, F, and T Ricco. "High-rate J-testing of toughened polyamide 6/6: Applicability of the load separation criterion and the normalization method." *Engineering Fracture Mechanics* 72 (2005): 2218–2231. <https://doi.org/10.1016/j.engfracmech.2005.02.002>.
- Baldi, Francesco, Silvia Agnelli, and Theonis Riccò. "On the applicability of the load separation criterion in determining the fracture resistance (J_{Ic}) of ductile polymers at low and high loading rates." *International Journal of Fracture* 165 (2010): 105–119. <https://doi.org/10.1007/s10704-010-9510-9>.
- Bedini, Rossella, Deborah Meleo, Raffaella Pecci, and Luciano Pacifici. "The use of microtomography in bone tissue and biomaterial three-dimensional analysis." *Annali dell'Istituto Superiore di Sanita* 45, no. 2 (2009): 178–184. ISSN: 00212571.

- Calvo-Guirado, José Luis, Gerardo Gómez-Moreno, Javier Guardia, Antonio Ortiz-Ruiz, Adriano Piatelli, Antonio Barone, José María Martínez-González, Luis Meseguer-Olmo, Laura López-Marí, and Cristina Barona Dorado. "Biological response to porcine xenograft implants: An experimental study in rabbits." *Implant Dentistry* 21, no. 2 (2012): 112–117. ISSN: 10566163. <https://doi.org/10.1097/ID.0b013e3182425991>.
- Carter, D. R., and W. C. Hayes. "The compressive behavior of bone as a two-phase porous structure." *Journal of Bone and Joint Surgery - Series A* 59, no. 7 (1977): 954–962. ISSN: 00219355. <https://doi.org/10.2106/00004623-197759070-00021>.
- Carter, Dennis R., and Wilson C. Hayes. "Bone Compressive Strength: The Influence of Density and Strain Rate." *Science* 194, no. 4270 (December 1976): 1174–1176. ISSN: 00368075. <https://doi.org/10.1126/SCIENCE.996549>.
- Chen, Po Yu, and Joanna McKittrick. "Compressive mechanical properties of demineralized and deproteinized cancellous bone." *Journal of the Mechanical Behavior of Biomedical Materials* 4, no. 7 (2011): 961–973. ISSN: 17516161. <https://doi.org/10.1016/j.jmbbm.2011.02.006>.
- Cho, Jung Sang, Hyung Sup Kim, Seung Hoon Um, and Sang Hoon Rhee. "Preparation of a novel anorganic bovine bone xenograft with enhanced bioactivity and osteoconductivity." *Journal of Biomedical Materials Research - Part B Applied Biomaterials* 101 B, no. 5 (2013): 855–869. ISSN: 15524973. <https://doi.org/10.1002/jbm.b.32890>.
- Choi, S., and B. V. Sankar. "Fracture Toughness of Carbon Foam." *Journal of Composite Materials* 37, no. 23 (2003): 2101–2116. ISSN: 00219983. <https://doi.org/10.1177/002199803036264>.
- Cook, R. B., C. Curwen, T. Tasker, and P. Zioupos. "Fracture toughness and compressive properties of cancellous bone at the head of the femur and relationships to non-invasive skeletal assessment measurements." *Medical Engineering and Physics* 32, no. 9 (2010): 991–997. ISSN: 13504533. <https://doi.org/10.1016/j.medengphy.2010.06.014>.

BIBLIOGRAPHY

- Cook, R. B., and P. Zioupos. "The fracture toughness of cancellous bone." *Journal of Biomechanics* 42, no. 13 (September 2009): 2054–2060. ISSN: 00219290. <https://doi.org/10.1016/j.jbiomech.2009.06.001>.
- Cowin, S. C. "Wolff's Law of Trabecular Architecture at Remodeling Equilibrium." *Journal of Biomechanical Engineering* 108, no. 1 (February 1986): 83–88. ISSN: 0148-0731. <https://doi.org/10.1115/1.3138584>.
- Daminabo, S C, S Goel, S A Grammatikos, H Y Nezhad, and V K Thakur. "Fused deposition modeling-based additive manufacturing (3D printing): techniques for polymer material systems." *Materials Today Chemistry* 16 (2020): 100248. ISSN: 2468-5194. <https://doi.org/10.1016/j.mtchem.2020.100248>. <https://doi.org/10.1016/j.mtchem.2020.100248>.
- Di Stefano, Danilo, Giorgio Gastaldi, Raffaele Vinci, Elisabetta Polizzi, Lorenzo Cinci, Laura Pieri, and Enrico Gherlone. "Bone Formation Following Sinus Augmentation with an Equine-Derived Bone Graft: A Retrospective Histologic and Histomorphometric Study with 36-Month Follow-up." *The International Journal of Oral & Maxillofacial Implants* 31, no. 2 (2016): 406–412. ISSN: 08822786. <https://doi.org/10.11607/jomi.4373>.
- Dimitriou, Rozalia, George I. Mataliotakis, Antonios G. Angoules, Nikolaos K. Kanakaris, and Peter V. Giannoudis. "Complications following autologous bone graft harvesting from the iliac crest and using the RIA: A systematic review." *Injury* 42, no. SUPPL. 2 (2011): S3–S15. ISSN: 18790267. <https://doi.org/10.1016/j.injury.2011.06.015>.
- Egan, Paul F, Nava Raj Khatri, Manasi Anil Parab, and Amit M E Arefin. "Mechanics of 3D-Printed Polymer Lattices with Varied Design and Processing Strategies." *Polymers* 14 (2022): 5515. <https://doi.org/10.3390/polym14245515>.
- Eom, Jung Hye, Young Wook Kim, and Santosh Raju. "Processing and properties of macroporous silicon carbide ceramics: A review." *Journal of Asian Ceramic Societies* 1, no. 3 (2013): 220–242. ISSN: 21870764. <https://doi.org/10.1016/j.jascer.2013.07.003>.

- Eren, Ogulcan, Hüseyin Kürsad Sezer, and Necati Yalcin. "Effect of lattice design on mechanical response of PolyJet additively manufactured cellular structures." *Journal of Manufacturing Processes* 75, no. January (2022): 1175–1188. <https://doi.org/10.1016/j.jmapro.2022.01.063>.
- Gallo, Nunzia, Maria Lucia Natali, Alessandro Sannino, and Luca Salvatore. "An overview of the use of equine collagen as emerging material for biomedical applications." *Journal of Functional Biomaterials* 11, no. 4 (2020): 1–27. ISSN: 20794983. <https://doi.org/10.3390/jfb11040079>.
- Gibson, Lorna J., and Michael F. Ashby. *Cellular solids: Structure and properties, second edition*, 510. Cambridge University Press, January 1997. ISBN: 9781139878326. <https://doi.org/10.1017/CBO9781139878326>.
- González-Henríquez, Carmen M, Mauricio A Sarabia-Vallejos, and Juan Rodriguez-Hernandez. "Progress in Polymer Science Polymers for additive manufacturing and 4D-printing : Materials , methodologies , and biomedical applications." *Progress in Polymer Science* 94 (2019): 57–116. ISSN: 0079-6700. <https://doi.org/10.1016/j.progpolymsci.2019.03.001>. <https://doi.org/10.1016/j.progpolymsci.2019.03.001>.
- Greenwald, A Seth, Scott D Boden, Victor M Goldberg, Yusuf Khan, Cato T Laurencin, and Randy N Rosier. "Bone-graft substitutes: facts, fictions, and applications." *Journal of Bone and Joint Surgery - Series A* 83-A, no. Supplement 2, Part 2 (2001): 98–103.
- Griffith, A.A. "The phenomena of rupture and flow in solids." *Philosophical Transactions of the Royal Society of London* 221 (1920): 163–198. ISSN: 00254576. <https://doi.org/10.1098/rsta.1921.0006>.
- Guedes, R. M., J. A. Simões, and J. L. Morais. "Viscoelastic behaviour and failure of bovine cancellous bone under constant strain rate." *Journal of Biomechanics* 39, no. 1 (2006): 49–60. ISSN: 00219290. <https://doi.org/10.1016/j.jbiomech.2004.11.005>.
- Hassenkam, Tue, Georg E. Fantner, Jacqueline A. Cutroni, James C. Weaver, Daniel E. Morse, and Paul K. Hansma. "High-resolution AFM imaging of intact and fractured trabecular bone." *Bone* 35, no. 1 (2004): 4–10. ISSN: 87563282. <https://doi.org/10.1016/j.bone.2004.02.024>.

BIBLIOGRAPHY

- Helgason, Benedikt, Egon Perilli, Enrico Schileo, Fulvia Taddei, Sigurdur Brynjólfsson, and Marco Viceconti. "Mathematical relationships between bone density and mechanical properties: A literature review." *Clinical Biomechanics* 23, no. 2 (2008): 135–146. ISSN: 02680033. <https://doi.org/10.1016/j.clinbiomech.2007.08.024>.
- Hernandez, C. J., F. M. Lambers, J. Widjaja, C. Chapa, and C. M. Rimnac. "Quantitative relationships between microdamage and cancellous bone strength and stiffness." *Bone* 66 (2014): 205–213. ISSN: 87563282. <https://doi.org/10.1016/j.bone.2014.05.023>.
- Hodgkinson, R., and J. D. Currey. "Young's modulus, density and material properties in cancellous bone over a large density range." *Journal of Materials Science: Materials in Medicine* 3, no. 5 (September 1992): 377–381. ISSN: 1573-4838. <https://doi.org/10.1007/BF00705371>.
- Huang, J. S., and L. J. Gibson. "Fracture toughness of brittle foams." *Acta Metallurgica Et Materialia* 39, no. 7 (1991): 1627–1636. ISSN: 09567151. [https://doi.org/10.1016/0956-7151\(91\)90250-5](https://doi.org/10.1016/0956-7151(91)90250-5).
- Javaid, Mohd., and Abid Haleem. "Additive manufacturing applications in medical cases: A literature based review." *Alexandria Journal of Medicine* 54, no. 4 (2018): 411–422. ISSN: 2090-5068. <https://doi.org/10.1016/j.ajme.2017.09.003>.
- Kashef, Sadaf, Alireza Asgari, Timothy B. Hilditch, Wenyi Yan, Vijay K. Goel, Peter Quadbeck, and Peter D. Hodgson. "Fracture mechanics of stainless steel foams." *Materials Science and Engineering: A* 578 (2013): 115–124. ISSN: 09215093. <https://doi.org/10.1016/j.msea.2013.03.062>.
- Keaveny, T. M., E. F. Morgan, G. L. Niebur, and O. C. Yeh. "Biomechanics of trabecular bone." *Annual Review of Biomedical Engineering* 3 (2001): 307–333. ISSN: 15239829. <https://doi.org/10.1146/ANNUREV.BIOEN.G.3.1.307>.
- Khan, Akhtar S., and Sujian. Huang. *Continuum theory of plasticity*. 421. Wiley, 1995. ISBN: 978-0-471-31043-3.

- Kim, Do Gyoon, Daniel Shertok, Boon Ching Tee, and Yener N. Yeni. "Variability of tissue mineral density can determine physiological creep of human vertebral cancellous bone." *Journal of Biomechanics* 44, no. 9 (2011): 1660–1665. ISSN: 00219290. <https://doi.org/10.1016/j.jbiomech.2011.03.025>.
- Kinaci, Ahmet, Valentin Neuhaus, and David C. Ring. "Trends in bone graft use in the United States." *Orthopedics* 37, no. 9 (2014): e783–e788. ISSN: 19382367. <https://doi.org/10.3928/01477447-20140825-54>.
- Koester, K J, H D Barth, and R O Ritchie. "Effect of aging on the transverse toughness of human cortical bone : Evaluation by R-curves." *Journal of the Mechanical Behavior of Biomedical Materials* 4, no. 7 (2011): 1504–1513. ISSN: 1751-6161. <https://doi.org/10.1016/j.jmbbm.2011.05.020>.
- Leahy, P. Devin, Barbara S. Smith, Katrina L. Easton, Chris E. Kawcak, Jens C. Eickhoff, Snehal S. Shetye, and Christian M. Puttlitz. "Correlation of mechanical properties within the equine third metacarpal with trabecular bending and multi-density micro-computed tomography data." *Bone* 46, no. 4 (2010): 1108–1113. ISSN: 87563282. <https://doi.org/10.1016/j.bone.2010.01.366>.
- Les, C. M., J. H. Keyak, S. M. Stover, K. T. Taylor, and A. J. Kaneps. "Estimation of material properties in the equine metacarpus with use of quantitative computed tomography." *Journal of Orthopaedic Research* 12, no. 6 (1994): 822–833. ISSN: 1554527X. <https://doi.org/10.1002/jor.1100120610>.
- Ling, Chen, Alessandro Cernicchi, Michael D Gilchrist, and Philip Cardiff. "Mechanical behaviour of additively-manufactured polymeric octet-truss lattice structures under quasi-static and dynamic compressive loading." *Materials & Design* 162 (2019): 106–118. ISSN: 0264-1275. <https://doi.org/10.1016/j.matdes.2018.11.035>.

BIBLIOGRAPHY

- Lowe, Jason A., Gregory J. Della Rocca, Yvonne Murtha, Frank A. Liporace, Michael D. Stover, Sean E. Nork, and Brett D. Crist. "Complications associated with negative pressure reaming for harvesting autologous bone graft: A case series." *Journal of Orthopaedic Trauma* 24, no. 1 (2010): 46–52. ISSN: 08905339. <https://doi.org/10.1097/BOT.0bo13e31819c0ccb>.
- Macosko, Christopher W. *Rheology Principles, Measurements and Applications*. Wiley-VCH, 1994. ISBN: 1560815795.
- Marşavina, Liviu, and Emanoil Linul. "Fracture toughness of rigid polymeric foams: A review." *Fatigue and Fracture of Engineering Materials and Structures* 43, no. 11 (2020): 2483–2514. ISSN: 14602695. <https://doi.org/10.1111/ffe.13327>.
- Martin, R. Bruce, David B. Burr, Neil A. Sharkey, and David P. Fyhrie. *Skeletal Tissue Mechanics*. Second Edi, 501. New York: Springer Science+Business Media, 2015. ISBN: 9781493930012. <https://doi.org/10.1007/978-1-4939-3002-9>.
- Maskery, I, L Sturm, A O Aremu, A Panesar, C B Williams, C J Tuck, R D Wildman, I A Ashcroft, and R J M Hague. "Insights into the mechanical properties of several triply periodic minimal surface lattice structures made by polymer additive manufacturing." *Polymer* 152 (2018): 62–71. ISSN: 0032-3861. <https://doi.org/10.1016/j.polymer.2017.11.049>.
- Matsumoto, Noah, and John A Nairn. "Fracture toughness of wood and wood composites during crack propagation." *Wood and Fiber Science* 44, no. 2 (2012): 121–133.
- McCullough, K. Y.G., N. A. Fleck, and M. F. Ashby. "Toughness of aluminum alloy foams." *Acta Materialia* 47, no. 8 (1999): 2331–2343. ISSN: 13596454. [https://doi.org/10.1016/S1359-6454\(99\)00125-1](https://doi.org/10.1016/S1359-6454(99)00125-1).
- Moore, D.R., J.G. Williams, and A. Pavan. *Fracture mechanics testing methods for polymers, adhesives and composites*. 388. Elsevier Sci Ltd, 2001. ISBN: 9780080531960.

- Nagaraja, Srinidhi, Mario D. Ball, and Robert E. Guldberg. "Time-dependent damage accumulation under stress relaxation testing of bovine trabecular bone." *International Journal of Fatigue* 29, no. 6 (2007): 1034–1038. ISSN: 01421123. <https://doi.org/10.1016/j.ijfatigue.2006.09.019>.
- Nalla, R. K., J. J. Kruzic, J.H. Kinney, and R.O. Ritchie. "Effect of aging on the toughness of human cortical bone: evaluation by R-curves." *Bone* 35 (2004): 1240–1246. <https://doi.org/10.1016/j.bone.2004.07.016>.
- O'Masta, M. R., L. Dong, L. St-Pierre, H. N.G. Wadley, and V. S. Deshpande. "The fracture toughness of octet-truss lattices." *Journal of the Mechanics and Physics of Solids* 98, no. September 2016 (2017): 271–289. ISSN: 00225096. <https://doi.org/10.1016/j.jmps.2016.09.009>.
- Odén, A., E. V. McCloskey, J. A. Kanis, N. C. Harvey, and H. Johansson. "Burden of high fracture probability worldwide: secular increases 2010–2040." *Osteoporosis International* 26, no. 9 (2015): 2243–2248. ISSN: 14332965. <https://doi.org/10.1007/s00198-015-3154-6>.
- Odgaard, A., J. Kabel, B. Rietbergern, M. Dalstra, and R. Huiskes. "Fabric and Elastic Principal Directions of Cancellous." *Journal of biomechanics* 30, no. 5 (1997): 487–495.
- Pagano, Claudia, Lara Rebaioli, Francesco Baldi, Irene Fassi, Claudia Pagano, Lara Rebaioli, Francesco Baldi, and Irene Fassi. "Relationships between size and mechanical properties of scaffold-like structures." *Mechanics of Advanced Materials and Structures* 28, no. 17 (2021): 1812–1817. ISSN: 1537-6494. <https://doi.org/10.1080/15376494.2019.1709675>.
- Penumakala, Pavan Kumar, Jose Santo, and Alen Thomas. "A critical review on the fused deposition modeling of thermoplastic polymer composites." *Composites Part B: Engineering* 201, no. August (2020): 108336. ISSN: 13598368. <https://doi.org/10.1016/j.compositesb.2020.108336>.
- Rice, J. C., S. C. Cowin, and J. A. Bowman. "On the dependence of the elasticity and strength of cancellous bone on apparent density." *Journal of Biomechanics* 21, no. 2 (January 1988): 155–168. ISSN: 0021-9290. [https://doi.org/10.1016/0021-9290\(88\)90008-5](https://doi.org/10.1016/0021-9290(88)90008-5).

BIBLIOGRAPHY

- Rice, J. R. "A path independent integral and the approximate analysis of strain concentration by notches and cracks." *Journal of Applied Mechanics, Transactions of the ASME* 35, no. 2 (1968): 379–388. ISSN: 15289036. <https://doi.org/10.1115/1.3601206>.
- Ritchie, Robert O., Markus J. Buehler, and Paul Hansma. "Plasticity and toughness in bone." *Physics Today* 62, no. 6 (2009): 41–47. ISSN: 00319228. <https://doi.org/10.1063/1.3156332>.
- Rosa, M. E., and M. A. Fortes. "Deformation and fracture of cork in tension." *Journal of Materials Science* 26, no. 2 (1991): 341–348. ISSN: 00222461. <https://doi.org/10.1007/BF00576525>.
- Rupp, Markus, Maximilian Kerschbaum, Lisa Klute, Leona Frank, and Volker Alt. "Bone transplantation or biomaterials?: An analysis of 99,863 surgical procedures in orthopedic and trauma surgery in Germany from 2018." *Unfallchirurg* 124, no. 2 (2021): 146–152. ISSN: 01775537. <https://doi.org/10.1007/s00113-020-00861-z>.
- Rupp, Markus, Lisa Klute, Susanne Baertl, Nike Walter, Gopala Krishna Mannala, Leona Frank, Christian Pfeifer, Volker Alt, and Maximilian Kerschbaum. "The clinical use of bone graft substitutes in orthopedic surgery in Germany—A 10-years survey from 2008 to 2018 of 1,090,167 surgical interventions." *Journal of Biomedical Materials Research - Part B Applied Biomaterials* 110, no. 2 (2022): 350–357. ISSN: 15524981. <https://doi.org/10.1002/jbm.b.34911>.
- Russo, Raffaele, Marco Maiotti, and Ettore Taverna. "Arthroscopic bone graft procedure combined with arthroscopic subscapularis augmentation (ASA) for recurrent anterior instability with glenoid bone defect: a cadaver study." *Journal of Experimental Orthopaedics* 5, no. 1 (2018). ISSN: 21971153. <https://doi.org/10.1186/s40634-018-0121-0>.
- Scanlon, M. G., D. Fahloul, and H. D. Sapirstein. "A Measure of Fracture Toughness of Bread Crumb." *Cereal Chemistry* 74, no. 5 (1997): 612–613. ISSN: 0009-0352. <https://doi.org/10.1094/cchem.1997.74.5.612>.

- Sen, M. K., and T. Miclau. "Autologous iliac crest bone graft: Should it still be the gold standard for treating nonunions?" *Injury* 38, no. SUPPL. 1 (2007): 2–7. ISSN: 00201383. <https://doi.org/10.1016/j.injury.2007.02.012>.
- Shaikeea, Angkur Jyoti Dipanka, Huachen Cui, Mark O'Masta, Xiaoyu Rayne Zheng, and Vikram Sudhir Deshpande. "The toughness of mechanical metamaterials." *Nature Materials* 21, no. 3 (2022): 297–304. ISSN: 1476-4660. <https://doi.org/10.1038/s41563-021-01182-1>.
- Shalchy, Faezeh, Christopher Lovell, and Atul Bhaskar. "Hierarchical porosity in additively manufactured bioengineering scaffolds: Fabrication & characterisation." *Journal of the Mechanical Behavior of Biomedical Materials* 110, no. April (2020): 103968. ISSN: 18780180. <https://doi.org/10.1016/j.jmbbm.2020.103968>.
- Sharobeam, M. H., and J.D. Landes. "The load separation and η_{pl} development in precracked specimen test records." *International Journal of Fracture* 59 (1993): 213–226.
- . "The load separation criterion and methodology in ductile fracture mechanics." *International Journal of Fracture* 47 (1991): 81–104.
- Surjadi, James Utama, and Yang Lu. "Design criteria for tough metamaterials." *Nature Materials* 21, no. 3 (2022): 272–274. ISSN: 14764660. <https://doi.org/10.1038/s41563-022-01193-6>.
- Sylvester, Adam D., and Claire E. Terhune. "Trabecular mapping: Leveraging geometric morphometrics for analyses of trabecular structure." *American Journal of Physical Anthropology* 163, no. 3 (2017): 553–569. ISSN: 10968644. <https://doi.org/10.1002/ajpa.23231>.
- Symons, Jennifer E, Rachel C Entwistle, Amanda M Arens, Tanya C Garcia, Blaine A Christiansen, David P Fyhrie, and Susan M Stover. "Mechanical and morphological properties of trabecular bone samples obtained from third that syndrome." *American journal of veterinary research* 73, no. 11 (2012).
- Tortora, G. J. *Principles of Human Anatomy*. 12th. 1056. Wiley, 2010. ISBN: 9780470567050.

BIBLIOGRAPHY

- Wang, Xinxin, Tianyu Gao, Chong Shi, Yin Zhou, Zhendong Li, and Zhong-gang Wang. "Effect of geometric configuration on compression behavior of 3D-printed polymeric triply periodic minimal surface sheets." *Mechanics of Advanced Materials and Structures* 30, no. 11 (2023): 2304–2314.
- Weiner, S., and H. D. Wagner. "The material bone: Structure-mechanical function relations." *Annual Review of Materials Science* 28, no. 1 (1998): 271–298. ISSN: 00846600. <https://doi.org/10.1146/annurev.matsci.28.1.271>.
- Wells, A.A. "Unstable Crack Propagation in Metals: Cleavage and Fast Fracture." *Proceedings of the Crack Propagation Symposium* 1 (1961): 84.
- Wychowanski, Piotr, Jarosław Woliński, Tadeusz Morawiec, Patryk Kownacki, Anna Starzynska, Maciej Kosieradzki, and Piotr Fiedor. "Preliminary Clinical Data and the Comparison of the Safety and Efficacy of Autogenous Bone Grafts Versus Xenograft Implantations in Vertical Bone Deficiencies Before Dental Implant Installation." *Transplantation Proceedings* 52, no. 7 (2020): 2248–2251. ISSN: 18732623. <https://doi.org/10.1016/j.transproceed.2020.02.099>.
- Yamamoto, Ei, R. Paul Crawford, Deva D. Chan, and Tony M. Keaveny. "Development of residual strains in human vertebral trabecular bone after prolonged static and cyclic loading at low load levels." *Journal of Biomechanics* 39, no. 10 (2006): 1812–1818. ISSN: 00219290. <https://doi.org/10.1016/j.jbiomech.2005.05.017>.
- Yeni, Y. N., C. U. Brown, and T. L. Norman. "Influence of bone composition and apparent density on fracture toughness of the human femur and tibia." *Bone* 22, no. 1 (1998): 79–84. ISSN: 87563282. [https://doi.org/10.1016/S8756-3282\(97\)00227-5](https://doi.org/10.1016/S8756-3282(97)00227-5).
- Yeo, Seon Ju, Min Jun Oh, and Pil J. Yoo. "Structurally Controlled Cellular Architectures for High-Performance Ultra-Lightweight Materials." *Advanced Materials* 31, no. 34 (2019): 1–26. ISSN: 15214095. <https://doi.org/10.1002/adma.201803670>.

- Zhao, Rusin, Ruijia Yang, Paul R. Cooper, Zohaib Khurshid, Amin Shavandi, and Jithendra Ratnayake. "Bone grafts and substitutes in dentistry: A review of current trends and developments." *Molecules* 26, no. 10 (2021): 1–27. ISSN: 14203049. <https://doi.org/10.3390/molecules26103007>.
- Zimmermann, Elizabeth A, Björn Busse, and Robert O Ritchie. "The fracture mechanics of human bone: influence of disease and treatment." *BoneKEy Reports* 4 (2015): 743. <https://doi.org/10.1038/bonekey.2015.112>.
- Zysset, Philippe K. "A review of morphology-elasticity relationships in human trabecular bone: Theories and experiments." *Journal of Biomechanics* 36, no. 10 (2003): 1469–1485. ISSN: 00219290. [https://doi.org/10.1016/S0021-9290\(03\)00128-3](https://doi.org/10.1016/S0021-9290(03)00128-3).